Colloidal Hydrodynamics and Interfacial Effects

Maciej Lisicki and Gerhard Nägele

Abstract Interfaces and boundaries play an important role in numerous soft matter and biological systems. Apart from direct interactions, the boundaries interact with suspended microparticles by altering the solvent flow field in their vicinity. Hydrodynamic interactions with walls and liquid interfaces may lead to a significant change in the particle dynamics in (partially) confined geometry. In these lecture notes, we review basic concepts related to colloidal hydrodynamics and discuss in more detail the effects of geometric confinement and the hydrodynamic boundary condition which an interface imposes on a suspension of microparticles. We start with considering the general characteristic features of low-Reynolds-number flows, which are an inherent part of any colloidal system, and discuss the appropriate boundary conditions for various types of interfaces. We then proceed to develop a proper theoretical description of the friction-dominated, inertia-free dynamics of colloidal particles. To this end, we introduce the concept of hydrodynamic mobility, and analyse the solutions of the Stokes equations for single spherical particle in bulk and in the presence of a planar solid-fluid, and fluid-fluid interfaces. Both forced and phoretic motions are considered, with particular emphasis on the principles of electrophoresis and the associated fluid flows. Moreover, we discuss the hydrodynamic interactions of self-propelling microswimmers, and the peculiar motion of bacteria attracted to slip and no-slip walls.

Warning: This is a preliminary version which may contain errors. The final version has been published in:
Soft Matter at Aqueous Interfaces, P. R. Lang and Y. Liu (Eds), Lecture Notes in Physics, Vol. 917, 313-386, Springer (2016), doi:10.1007/978-3-319-24502-7_10

Maciej Lisicki
Institute of Theoretical Physics, Faculty of Physics, University of Warsaw, Warsaw, Poland. e-mail: mklis@fuw.edu.pl

Gerhard Nägele
Institute for Complex Systems ICS-3, Forschungszentrum Jülich, and Institut für Theoretische Physik, Heinrich-Heine-Universität Düsseldorf, Germany. e-mail: g.naegele@fz-juelich.de

1 Introduction

Mesoscale particles suspended in a viscous fluid are found in numerous technological processes and products, including paints, cosmetics, pharmaceuticals, and foodstuff. They are encountered also in biological processes involving complex fluids, and animalcules such as eukaryotic cells and bacteria. Understanding the dynamics of such systems, often referred to as passive or active soft matter systems, is of importance not only for industrial development, materials science, microbiology and health care, but also from the point of view of fundamental scientific problems such as in dynamic phase transitions. The importance of soft matter systems derives also from their diversity, and the variety of tunable particle interactions giving rise to a plethora of phenomena that are partially still unexplored. An inherent feature of such systems is the presence of a viscous solvent which transmits mechanical stresses through the fluid, affecting in this way the motion of suspended particles. These solvent-mediated particle interactions are known as hydrodynamic interactions (HIs). The presence of HIs affects the dynamic properties of soft matter systems: In colloidal suspensions, e.g., they change the diffusion and rheological suspension properties [1], and play an important role in the dynamics of DNA helices and proteins in solution [2]. Moreover, HIs modify the characteristics of the coiling-stretching transition in polymers [3], influence the pathways of phase separation in binary mixtures [4], alter the kinetics of macromolecules adsorption on surfaces [5] and cell adhesion [6], and are at the origin of the flow-induced polymer migration in microchannels [7].

There has been a growing interest in the physics of soft matter systems, particularly triggered by the development of experimental techniques allowing for probing soft matter on smaller length and time scales. The widespread use of advanced optical microscopy and light scattering techniques in scientific and industrial laboratories has fostered the insight in the structure and dynamics of soft matter systems, and has boosted the development of theoretical and numerical tools used in tackling emerging problems. The complexity of the studied systems has considerably grown over the past years. Yet, the underlying physical principles remain rather simple, so that if not fully quantitative then at least qualitative predictions of dynamic properties can still be made.

Quite interestingly, many relevant hydrodynamic processes take place under (partial) confinement such as in a vessel or channel, close to a cell wall, inside droplets, in the presence of bubbles, or near macroscopic fluid interfaces. Since the confining boundaries or interfaces can have a dominant effect on the system dynamics, it is important to analyse in detail their effect on the fluid flow in their relative vicinity, and on the motion of suspended particles.

The aim of these lecture notes is to give an elementary introduction into hydrodynamic effects occurring in colloidal systems, with particular emphasis on interfacial effects. There are various mathematical subtleties showing up in the theoretical and computer simulation modelling of colloidal hydrodynamics. In this more elementary introduction, however, we leave these subtleties aside, focusing instead on the physical principles without attempting to be mathematically rigorous.

There exists a large number of overview articles and textbooks on the hydrodynamics of soft matter systems, on different levels of complexity. As introductory texts on colloid hydrodynamics, we recommend the textbooks by Dhont [1] and Guazzelli and Morris [8], the lecture notes by Nägele in [9, 10], and the overview articles by Hinch [11], Pusey [12], and Pusey and Jones [13]. More advanced topics related to slow viscous flows are addressed in the excellent textbooks of Kim & Karrila [14], Happel & Brenner [15], and Zapryanov & Tabakova [16]. Standard textbooks on general hydrodynamics are the ones by Batchelor [17], and Landau and Lifshitz [18]. We further recommend the textbook by Guyon *et al.* [19]. A set of classical videos by G. I. Taylor [20] is recommended as an enjoyable illustration of the general features of low-Reynolds-number hydrodynamics discussed in the present notes.

Outline We start by introducing in Sec. 2 the Stokes (creeping flow) equations governing the low-Reynolds-number quasi-incompressible motion of a viscous fluid on colloidal time and length scales. The linear Stokes equations are a special case of the non-linear Navier-Stokes equations of incompressible flow, under the conditions where inertia effects are negligible and the particle motion is viscosity dominated. We show that these equations apply to flows related to the motions of suspended colloids and unicellular animalcules. The Stokes equations are amended by boundary conditions (BCs) on particle surfaces, confining interfaces and container walls. In this context, we discuss as important examples the no-slip and Navier partial-slip BCs for the fluid at a rigid surface, and the fluid-fluid BCs at a clean fluid-fluid interface. In Sec. 3, we explain salient generic features of Stokes flows, namely linearity, instantaneity, and kinematic reversibility. These features are used subsequently to infer some general knowledge on the motion of rigid microparticles in a viscous liquid. In Sec. 4, we analyse the bulk hydrodynamics of an unbounded colloidal suspension and the associated microparticles motion. For this purpose, we introduce the important concept of hydrodynamic friction and mobility tensors. Moreover, we discuss a versatile set of elemental solutions of the Stokes equations from which the flow profiles in simple situations are readily constructed. As examples, we discuss the motion of a slender particle (a rod) where the shape anisotropy results in anisotropic friction, and a spherical particle driven by body forces (i.e. gravitational settling), or by external fields such as temperature or electric potential gradient (phoretic motion). We introduce the notion of many-body hydrodynamic interactions (HIs) between microparticles, and outline how these interactions can be accounted for theoretically. The section is concluded by the lubrication analysis of the motion of two nearly touching spheres, and of a sphere near a flat no-slip wall.

Sec. 5 is dedicated to single-particle dynamics in the presence of a flat interface. We show how the solutions of the Stokes equations in (partially) confined geometry can be constructed using a superposition of the previously introduced elemental flow solutions, and discuss the implications of various interfacial boundary conditions on the dynamics of a suspended colloidal particle. In particular, we discuss the translational and rotational motion of a spherical particle near a no-slip wall, and comment on generalizations of this system to elastic particles and deformable

interfaces. In Sec. 6, we explore the self-propulsion of microswimmers such as bacteria and spermatozoa, both in the bulk fluid and near to a confining surface. Our concluding remarks are contained in Sec. 7.

2 Fluid-particle dynamics on microscale

In this Section, we elucidate some of the basic features of microscale flows. Due to the typical small sizes and velocities of microparticles, the flow on these scales can be treated as inertia-free and dominated by viscous effects. The neglect of inertia in the Navier-Stokes equations of hydrodynamics leads to the linear Stokes equations. These equations need to be supplied with appropriate boundary conditions at interfaces confining the fluid. We introduce and discuss the BCs for a no-slip rigid wall, a clean fluid-fluid interface, and a partial slip surface.

2.1 Low-Reynolds-number flow

On length and time scales where continuum mechanics applies, the flow of an incompressible Newtonian fluid of shear viscosity η and constant mass density ρ_f is governed by the Navier-Stokes equations,

$$\rho_f \left(\frac{\partial \mathbf{u}(\mathbf{r},t)}{\partial t} + \mathbf{u}(\mathbf{r},t) \cdot \nabla \mathbf{u}(\mathbf{r},t) \right) = -\nabla p(\mathbf{r},t) + \eta \nabla^2 \mathbf{u}(\mathbf{r},t) + \mathbf{f}(\mathbf{r},t), \qquad (1)$$

$$\nabla \cdot \mathbf{u}(\mathbf{r},t) = 0, \qquad (2)$$

where $\mathbf{u}(\mathbf{r},t)$ is the velocity field at a point $\mathbf{r}$ at time t, and $p(\mathbf{r},t)$ is the pressure field. The shear viscosity η and the fluid mass density ρ_f are constant for a Newtonian fluid. The second equation follows from the continuity equation for a fluid of constant mass density, and is referred to as the incompressibility condition. The pressure in an incompressible fluid is determined only up to an additive constant, for p appears in the Navier-Stokes equations in form of its gradient only. The external body force field per unit volume acting on the fluid is denoted by $\mathbf{f}(\mathbf{r},t)$. It can be due, e.g., to an applied electric or magnetic field, and to particle surfaces or system boundaries confining the fluid. For the latter two cases, the body forces are singularly concentrated on two-dimensional surfaces. For surface hydrodynamic boundary conditions (BCs) involving velocities only, the effect of a constant gravitational field on the fluid can be included conveniently by redefining the pressure according to $p \to p + \rho_f \mathbf{g} \cdot \mathbf{r}$ where $\mathbf{g}$ is the gravitational acceleration. A particle of uniform mass density ρ_p and volume $\Delta\Omega_p$ experiences in the fluid the buoyancy-corrected gravitational force $\left(\rho_p - \rho_f\right) \Delta\Omega_p \mathbf{g}$ acting at its center-of-mass (Archimedes principle).

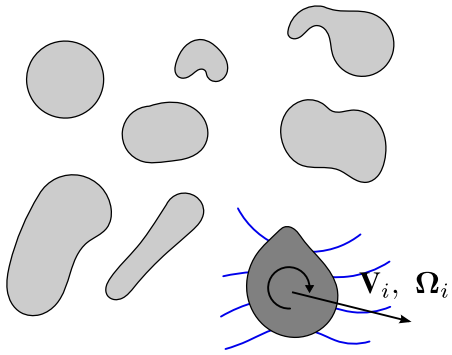

Fig. 1 Sketch of fluid flow around a microparticle labelled i with translational and rotational velocities $\mathbf{V}_i$ and $\boldsymbol{\Omega}_i$, respectively, in the presence of other immersed particles. Even if the rigid particles are free to translate and rotate in response to an externally imposed flow (freely advecting particles), they still modify the flow pattern through the BCs on their surfaces.

Consider now an ensemble of rigid, impermeable microparticles immersed in the fluid (Fig. 1). In many but not all cases, the particles have no-slip surfaces. This means that the velocity of the fluid at every point of a particle surface must match the velocity of the particle at this point. The motion of the material on the surface and inside a rigid particle i can be described by

$$\mathbf{u}(\mathbf{r}) = \mathbf{V}_i + \boldsymbol{\Omega}_i \times (\mathbf{r} - \mathbf{R}_i), \tag{3}$$

where $\mathbf{V}_i$ and $\boldsymbol{\Omega}_i$ are the particle's translational and angular velocity vectors, respectively, and $\mathbf{R}_i$ is a body-fixed reference point which can be taken, e.g., to be the centre-of-mass position. The particles influence the flow outside through the boundary conditions applied to their surfaces. Another influence on the fluid flow is caused by the boundary conditions on external boundaries such as container walls, or at infinity.

The Navier–Stokes Eqs. (1) include both inertial effects, represented by the two terms on the left-hand side proportional to ρ_f, and fluid viscosity effects which are included in the viscous force density term term $\eta\nabla^2\mathbf{u}$ on the right-hand side. The relative importance of these effects can be read off from the dimensionless Reynolds number Re. Suppose a sphere of radius a translates through the fluid with velocity of magnitude V. The Reynolds number associated with the fluid flow caused by the sphere's motion is

$$Re = \frac{\rho_f V a}{\eta} \sim \frac{|\mathbf{u}\cdot\nabla\mathbf{u}|}{|\eta\nabla^2\mathbf{u}|}. \tag{4}$$

For nano- to micrometer-sized particles, which includes in particular colloidal systems, the Reynolds number is typically of the order of 10^{-3} or even smaller [12]. This implies an important feature of so-called low-Reynolds-number flows: Inertial effects can be neglected as compared to the viscous ones so that the non-linear convective term $\mathbf{u}\cdot\nabla\mathbf{u}$ in Eq. (1) can be taken as zero. In the absence of intrinsic time scales originating from high-frequency oscillatory or ultra-strong forcing of particles, the linear time derivative term on the left-hand-side of the Navier-Stokes equation can be likewise neglected.

The description of microparticle-induced hydrodynamics in a Newtonian fluid reduces then to the Stokes equations,

$$-\nabla p(\mathbf{r}) + \eta \nabla^2 \mathbf{u}(\mathbf{r}) + \mathbf{f}(\mathbf{r}) = 0, \tag{5}$$

$$\nabla \cdot \mathbf{u}(\mathbf{r}) = 0, \tag{6}$$

also referred to as creeping flow equations. These equations have no explicit time dependence and are linear in the velocity and pressure fields.

Eq. (5) expresses the balance, at any instant of time and for every fluid element, of pressure gradient, viscous and external force densities. In the absence of external force density, the instantaneous values of velocity and pressure, and consequently the fluid stress field, depend solely on the momentary configuration and shape of particles and system boundaries, and on the surface boundary conditions taken at the particle surfaces and system boundaries. There is thus no dependence on the earlier flow history. Note that motion under Stokes flow conditions can be unsteady, with the velocities of particles and surrounding fluid changing as a function of time. An important example illustrating this fact is the settling of a spherical particle towards a stationary wall in its vicinity. This settling is discussed in Subsec. 4.7 in relation to the effect of lubrication. At any instant, however, the net force and torque on each particle and each fluid element are zero, with accordingly instantaneous linear force-velocity relations characteristic of non-inertial fluid *and* immersed microparticles motions. The flow and pressure fields pattern readjust quasi-instantaneously to the moving system boundaries and particle surfaces.

In consequence, the hydrodynamic drag force $\mathbf{F}^h$ and torque $\mathbf{T}^h$ acting on a particle due to its surface friction with the surrounding fluid are exactly balanced, according to

$$\begin{aligned} \mathbf{F}^h + \mathbf{F} &= \mathbf{0}, \\ \mathbf{T}^h + \mathbf{T} &= \mathbf{0}, \end{aligned} \tag{7}$$

by a non-hydrodynamic 'external' force $\mathbf{F}$ and torque $\mathbf{T}$, respectively, caused by direct interactions with other particles and system boundaries, and by external force fields. Only a force-free and torque-free particle will move quasi-inertia-free. There is an addition a so-called thermodynamic force contribution to $\mathbf{F}$ proportional to the system temperature T which accounts for the on average isotropic thermal bombardment of a microparticle by the surrounding fluid molecules. If viewed on the time and length scales where creeping flow applies this bombardment leads to an erratic Brownian motion of the particles which persists even in the absence of additional force contributions to $\mathbf{F}$.

The strength of the Brownian motion of a particle can be characterized by the diffusion time τ_D which is the time required by a particle to diffuse by Brownian motion over a distance comparable to its size. For a spherical particle of radius a, this characteristic time is

$$\tau_D = \frac{a^2}{D^0} \propto \eta \frac{a^3}{T}, \tag{8}$$

where

$$D^0 = \frac{k_B T}{C\eta a}, \tag{9}$$

is the single-sphere Stokes-Einstein translational diffusion coefficient. This coefficient decreases with increasing particle size and fluid viscosity, and it increases with increasing temperature T. The numerical coefficient C depends on the hydrodynamic boundary condition for the flow at the sphere surface. According to [1]

$$\left\langle [\mathbf{R}(t) - \mathbf{R}(0)]^2 \right\rangle = 6D^0 t, \tag{10}$$

where D^0 quantifies the magnitude of the mean-squared displacement, after the time span t, of the position vector $\mathbf{R}$ of an isolated Brownian particle immersed in an unbounded fluid. The brackets denote here an average over an equilibrium ensemble of non-interacting Brownian particles.

The diffusion time grows strongly with increasing particle size. For water at room temperature as the suspending fluid, it increases from $\tau_D \sim 5$ ms for $a = 0.1$ μm to $\tau_D \sim 0.3$ h for $a = 5$ μm. Brownian motion is thus negligibly small for particles of several micrometers in size or larger. These particles are therefore referred to as non-Brownian. A dispersion of non-Brownian particles requires external driving agents to keep them in motion. This agent can be gravity, provided some of the particles are lighter or heavier than the fluid, or an applied electric, magnetic or temperature gradient field. Additionally, the particles are hydrodynamically moved by incident flows created by moving system boundary parts (e.g., in cylindrical Couette cell flow) or applied pressure gradients (e.g., in pipe flow).

The distinguishing and to some extent surprising properties of fluid flows described by the Stokes equations, and of the associated microparticles motions, are and important theme of the present lecture notes, in addition to interfacial effects related to the fluid dynamics. In our discussion we will make ample use of streamlines pattern in order to visualize Stokes flow fields formed around particles in the bulk fluid and at interfaces. A streamline is tangential to the local velocity field at any fluid point, and for stationary flow it agrees with the pathway of a fluid element. For each streamline segment $d\mathbf{r}$, we have thus

$$d\mathbf{r} \times \mathbf{u}(\mathbf{r}) = \mathbf{0}. \tag{11}$$

The three Cartesian components of this vectorial equation form a coupled set of differential equations, for given $\mathbf{u}(\mathbf{r})$, from which the streamlines can be determined.

2.1.1 Hydrodynamic stresses

To every solution, $\{\mathbf{u}, p\}$, of the Stokes equations, referred to as a Stokes flow solution, one can associate a fluid stress field described in terms of a stress tensor $\boldsymbol{\sigma}$. This symmetric second-rank tensor consists of nine elements σ_{ij} with $i, j \in \{1,2,3\}$ which at a given fluid position $\mathbf{r}$ have values depending on the considered (rectan-

gular) coordinate system spanned by its three basis vectors $\{\mathbf{e}_1, \mathbf{e}_2, \mathbf{e}_3\}$. The stress tensor has the following physical meaning: Imagine a small planar surface element dS in the fluid with unit normal vector $\mathbf{n}$. The hydrodynamic drag force, d$\mathbf{F}$, exerted by the fluid on this surface element, located on the side where $\mathbf{n}$ points to, is then given by $\mathrm{d}\mathbf{F} = \boldsymbol{\sigma} \cdot \mathbf{n}\mathrm{d}S$. The tensor (matrix) element σ_{ij} is therefore the hydrodynamic force component per unit area (referred to as stress) acting in the direction $\mathbf{e}_i$ on an areal element with normal vector equal to $\mathbf{e}_j$ [17]. The stress field of an incompressible Newtonian fluid is given in terms of the flow fields $\mathbf{u}$ and p by

$$\boldsymbol{\sigma}(\mathbf{r}) = -p(\mathbf{r})\mathbf{I} + \eta \mathbf{E}(\mathbf{r}), \tag{12}$$

where $\mathbf{I}$ is the unit tensor, and

$$\mathbf{E}(\mathbf{r}) = [\nabla \mathbf{u}(\mathbf{r})] + [\nabla \mathbf{u}(\mathbf{r})]^T \tag{13}$$

is the symmetric fluid rate-of-strain tensor, with the superscript T denoting the transposition operation.

While the polyadic tensor expression for $\boldsymbol{\sigma}(\mathbf{r})$ in Eqs. (12) and (13) applies to all coordinate systems, the explicit form of its elements depends on the selected coordinates [15]. In Cartesian coordinates where the orthonormal basis vectors $\{\mathbf{e}_1, \mathbf{e}_2, \mathbf{e}_3\} = \{\mathbf{e}_x, \mathbf{e}_y, \mathbf{e}_z\}$ are constant, the stress tensor elements are simply given by

$$\sigma_{ij} = -p\delta_{ij} + \eta \left[\frac{\partial u_i}{\partial r_j} + \frac{\partial u_j}{\partial r_i} \right], \tag{14}$$

where $\{r_1, r_2, r_3\} = \{x, y, z\}$ are the Cartesian components of the fluid element position vector $\mathbf{r}$.

The hydrodynamic stress field depends on the properties of the fluid flow which in turn is influenced by the characteristics of the particles and confining walls, namely their porosity and fluid permeability, and other non-hydrodynamic surface properties such as surface charge density, van der Waals attraction etc. The knowledge of stresses in the fluid is of importance, since it allows for the calculation of hydrodynamic drag forces and torques acting on bodies immersed in the fluid. It is also of key importance for the calculation of rheological properties such as the effective suspension viscosity of a fluid with immersed microparticles [21]. Once the hydrodynamic stresses are known, the hydrodynamic drag force and torque, $\mathbf{F}^h$ and $\mathbf{T}^h$, acting on a particle can be calculated as the sum (integral) of the local surface force and torque contributions, respectively, according to

$$\begin{aligned} \mathbf{F}^h &= \int_S dS \boldsymbol{\sigma}(\mathbf{r}) \cdot \mathbf{n}(\mathbf{r}) \\ \mathbf{T}^h &= \int_S dS (\mathbf{r} - \mathbf{R}) \times \boldsymbol{\sigma}(\mathbf{r}) \cdot \mathbf{n}(\mathbf{r}) \end{aligned} \tag{15}$$

The surface S can be replaced by any fluid surface S^* enclosing the considered particle without intersecting another one, provided there is no body force density acting on the enclosed fluid part, since the hydrodynamic force and torque on a

particle are transmitted loss-free through the fluid [9]. The vector **n** is normal to the surface of the particle and points into the fluid. See here Fig. 2.

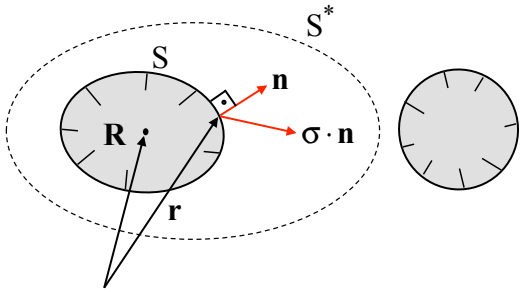

Fig. 2 Surface stress or traction (force per area), $\boldsymbol{\sigma}(\mathbf{r}) \cdot \mathbf{n}(\mathbf{r})$, exerted by the fluid on a particle surface element dS at position $\mathbf{r}$. The surface normal vector $\mathbf{n}$ points into the fluid. The vector $\mathbf{R}$ points to a particle-fixed reference point. For the calculation of drag force and torque, the surface S^* enclosing the particle can be chosen rather arbitrarily (see text).

It is important to realize that the arguments used to neglect the effects of inertia and the explicit time dependence of the fluid velocity and pressure fields are not applicable (i) if one studies processes on very short time and length scales where the time-dependence of $\mathbf{u}$ and p becomes essential, such as sound propagation in the fluid, and (ii) for processes which occur at different length scales so that the effective Reynolds number becomes large as compared to one. For a detailed discussion of the involved time and length scales of fluid and immersed microparticles, we refer to [1, 8, 12].

2.2 Boundary conditions

Fluid flows close to interfaces are strongly influenced by the interfacial properties. There exists an abundance of soft matter systems in which interfacial effects are highly influential on the dynamics. Notable examples of interfaces include: A smooth solid wall or particle surface; an engineered nano-structured surface; an interface between two immiscible fluids such as water and oil; liquid-gas free interfaces such as for gas bubbles in a liquid; surfactant-covered interfaces, and polymer-coated and grafted particle surfaces. To describe and understand the effect of interfaces on the flow behaviour, one needs to consider the appropriate boundary conditions imposed on the fluid at the surface or interface. The no-slip boundary condition for rigid impermeable surfaces noted in Eq. (3), first described by Navier in 1823, has been given considerable attention over the past two centuries, concerning in particular its applicability and validity [22]. It is generally accepted as the proper

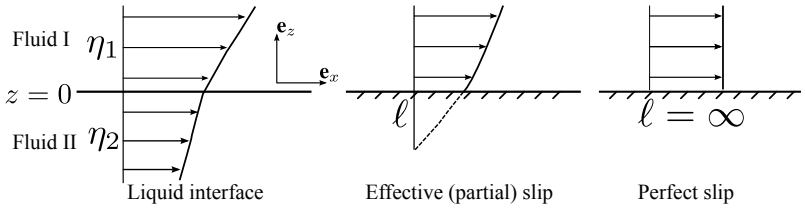

Fig. 3 Schematic flow profiles close to different interfaces as discussed in the notes. Left: A clean interface between two immiscible fluids of different viscosities $\eta_1 < \eta_2$, where du_x/dz changes discontinuously. Middle: Flow above a stationary rigid partial-slip surface, characterized by the Navier slip length ℓ equal to the distance to an apparent no-slip plane inside the stationary wall. Right: Plug-like flow above a stationary (perfect) slip wall where $\ell = \infty$. The same flow is observed near an ideal liquid-gas interface where $\eta_2/\eta_1 = 0$, and where the gas phase is situated in the lower half-space $z < 0$.

boundary condition for smooth solid hard walls, and for rigid particles with smooth non-permeable surfaces and sizes exceeding ~ 30 nm.

We discuss in the following two additional types of boundary conditions which are also frequently applied to soft matter systems. The first one concerns a clean liquid interface between two immiscible Newtonian fluids of viscosity ratio

$$\lambda = \eta_2/\eta_1, \tag{16}$$

with the associated near-interface flow sketched in the left part of Fig. 3. The appropriate boundary conditions are here the continuity of tangential velocities and tangential (shear) stresses of the two fluids at the interface, and the impermeability of the interface. The latter condition implies the equality of the normal velocity components of both fluids. Assuming a planar interface stretching out in the $x-y$ plane at $z=0$, these continuity conditions read

$$u_z^{(1)} = u_z^{(2)}, \qquad u_{x,y}^{(1)} = u_{x,y}^{(2)}, \qquad E_{xz}^{(1)} = \lambda E_{xz}^{(2)}, \qquad E_{yz}^{(1)} = \lambda E_{yz}^{(2)}, \tag{17}$$

where the $E_{\alpha\beta}^{(i)}$ are the Cartesian elements of the rate-of-strain tensor $\mathbf{E}$ of the fluid introduced in Eq. (13). The liquid-liquid BCs include as limiting cases firstly a free interface (e.g., a water-air interface) where the viscosity of the second fluid is negligible, so that $\lambda = 0$, and secondly a fluid above a rigid no-slip wall with the latter described as a fluid of infinite viscosity, so that $\lambda \to \infty$. In fact, $\lambda = 0$ implies a (perfect) slip surface of zero tangential stress while $\lambda \to \infty$ implies the no-slip condition $\mathbf{u}(z=0,x,y) = 0$ for a stationary wall.

The equality of the tangential stresses of both fluids at their interface is valid for uniform interfacial tension γ only, i.e. for constant free energy per area went into the formation of the interface. Any mechanism creating a gradient, $\nabla\gamma$, in the interfacial tension breaks the shear stress continuity and drives motions in the two fluids. These motions are referred to as Marangoni flows [23]. One possible way to

cause Marangoni flow is to establish a sufficiently strong temperature gradient along the interface [19].

For a planar liquid-liquid interface with zero motion of both fluids, the hydrostatic pressure on both sides is the same in order to maintain a stationary interface. However, for a stationary spherical droplet of radius a in a stationary fluid. the hydrostatic pressure in its interior exceeds the outside fluid pressure by the capillary (Laplace) pressure contribution γ/a. Any deformation of the droplet away from its equilibrium spherical shape of constant curvature and minimal surface free energy will cause flows and associated droplet motion which tend to re-establish its spherical shape. See Ref. [23] for a lucid discussion of droplet motions and Marangoni flow effects.

The second type of a boundary condition describes the partial-slip of fluid along the surface of a fluid-impermeable solid material, as illustrated in the middle and right parts of Fig. 3 where the solid extends to $z < 0$ with the fluid residing on top. The so-called Navier BCs for a stationary partial-slip surface demand, in addition to a vanishing normal velocity component at the surface, the proportionality of surface-tangential fluid velocity and shear stress according to

$$\mathbf{t}\cdot\mathbf{u} = \frac{\ell}{\eta}\mathbf{t}\cdot\boldsymbol{\sigma}\cdot\mathbf{n}, \qquad \mathbf{n}\cdot\mathbf{u} = 0\,. \tag{18}$$

Here, ℓ is the Navier slip length, and $\mathbf{t}$ and $\mathbf{n}$ are tangential and normal unit vectors at a surface point. For the planar stationary surface at $z = 0$ depicted in Fig. 3, the partial-slip BC for the surface-tangential velocity part simplifies to

$$u_{x,y} = \ell\,\frac{\partial u_{x,y}}{\partial z}, \qquad u_z = 0. \tag{19}$$

The slip length ℓ is here the distance into the interior of the wall for which the near-surface flow linearly extrapolates to zero, defining in this way an effective no-slip plane at $z = -\ell$. In the limit $\ell = 0$, the no-slip BC with zero surface slip velocity is recovered. In the opposite limit $\ell \to \infty$, the free-surface boundary condition of zero tangential stress is obtained, with fluid slipping perfectly along the surface in a plug-flow-like manner.

The Navier partial-slip BCs can serve as an effective description for a hydrophobic wall, a rigid particle with surface roughness or corrugations [24], and to some extent also for a wall grafted with polymer brushes acting as depletants [25]. Moreover, it can be used for a fluid-solid interface with free polymers in the fluid, and a polymer depletion layer at the interface [26]. An effective (apparent) fluid slip is also found in electrokinetic [21] and other phoretic flows where the no-slip boundary condition holds right at the wall and particle surfaces. Outside a thin fluid boundary layer with viscous flow, however, flow slip is observed [22]. In Subsec. 4.5, effective slip is discussed in relation to phoretic motion of a microsphere.

3 Generic features of Stokes flows

Creeping flows have interesting generic properties which appear counter-intuitive from the perspective of our macroscopic world experience where inertia and high-Reynolds-number effects prevail, with the flow governed by the non-linear Navier-Stokes equations. The three generic features of the Stokes equations are linearity, kinematic reversibility, and instantaneity. In this section, their implications for the colloidal dynamics are described.

3.1 Linearity

The Stokes equations are linear in contrast to the underlying Navier-Stokes equations. This means that the pressure, velocity and stress field are linearly related. The consequences of linearity are far-reaching. For instance, in a slow viscous channel flow, on doubling the applied pressure gradient a doubling of the flow rate is obtained. Moreover, a twofold increase in the rate of flow of viscous fluid through a porous medium will results in an unchanged pattern of streamlines of the flow, but with the magnitude of the fluid elements velocities doubled. For a sphere settling in a viscous liquid, doubling the settling velocity gives rise to a correspondingly doubled hydrodynamic drag force. The fact that the hydrodynamic force on a particle and the associated velocity (increment) are linearly related is exploited further in Subsec. 4.1, where we discuss the hydrodynamic friction and mobility coefficients in many-particle dispersions.

For linear evolution equations such as the Stokes equations, the superposition principle is valid: If $\mathbf{u}_1$ and $\mathbf{u}_2$ are two velocity solutions of the Stokes equations, then

$$\mathbf{u} = \lambda_1 \mathbf{u}_1 + \lambda_2 \mathbf{u}_2 \tag{20}$$

$$\nabla p = \lambda_1 \nabla p_1 + \lambda_2 \nabla p_2 \tag{21}$$

are likewise solutions with coefficients λ_1 and λ_2. Here, ∇p_i is the pressure gradient field solution to the Stokes equations associated with $\mathbf{u}_i$. For a given flow problem boundary value problem, the unique velocity field $\mathbf{u}$ can be obtained from the linear superposition of two (simpler) flows with unchanged geometry, provided the velocity BCs of the two partial flows superimpose correspondingly, with the same coefficients, to the BCs of the full flow solution.

The linearity of the Stokes flow solutions can lead to rather unexpected conclusions; Consider a particle, moving through the fluid with the velocity $\mathbf{V}$ with Cartesian components V_i, $i = 1,2,3$. The particle experiences then the drag force $-\mathbf{F}$ which we can decompose into forces acting along the axes of the coordinate system according to $\mathbf{F} = \{F_i\}$. From linearity, we conclude that the force F_1 acting on a particle moving with velocity $(V_1,0,0)$ must be of the form $F_1 = \alpha V_1$, with α being a positive constant. Imagine now that the particle is a cube with its edges

aligned along the coordinate axes. Then, from symmetry, $F_2 = \alpha V_2$ and $F_3 = \alpha V_3$, and in general $\mathbf{F} = \alpha \mathbf{V}$. Hence the drag force experienced by a cube does not depend on its orientation, and it is collinear with the velocity. As everyday experience teaches us, this is obviously not valid any more for large *Re*. In fact, a more general

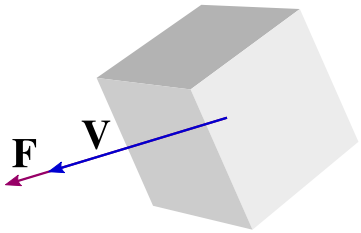

Fig. 4 A cube translating through a viscous fluid with velocity **V** under the influence of force **F** acting on its centre. For highly symmetric particles, linearity of Stokes equation implies that the force and velocity are collinear, with the drag force being independent of the particle orientation.

statement is true: Any homogeneous body with three orthogonal planes of symmetry (such as spheroids, rods, cylinders, disks, or rings), will translate under the action of force without rotating, although in general with a sidewise velocity component perpendicular to the driving force. The sidewise motion is absent only if the force is acting along the rotational symmetry axis of the particle. In addition, force and velocity are collinear independently of the particle orientation for highly symmetric particles, namely for a homogeneous sphere and the five regular polyhedra (tetrahedron, cube, etc.), and also for homogeneous bodies made from the polyhedra by equally rounding off their corners, provided the hydrodynamic BCs are homogeneous [9, 11]. For this statement to be true, the particle centre must be selected as the reference point.

As noted earlier, linearity can be used to decompose a complex flow problem into a number of simpler ones: one can for instance consider the problem of a spherical particle translating and rotating in a viscous fluid as the two separate problems of sole rotation and sole translation of a sphere, provided a corresponding linear decomposition of the surface boundary conditions (3) is used. Such a decomposition proves useful in various numerical schemes for the calculation, e.g., of the hydrodynamic drag forces on an ensemble of spherical particles at a given fixed configuration. One has to bear in mind, however, that the imposed BCs must be simultaneously satisfied at the surfaces of all the particles. For more than two particles, this requires in general a complicated numerical analysis.

3.2 Instantaneity

On the time and length scales where significant motion of colloidal microparticles is observed, the accompanying viscous flows are described by the quasi-stationary

linear Stokes equations which have no explicit time dependence. As noted before, this means that the pressure and velocity fields adjust themselves instantaneously, on the coarse-grained colloidal time and length scales, to changes in the driving forces. The flow disturbances propagate in the fluid with an (apparently) infinite speed. A slight change in a particle's position or velocity is instantaneously communicated to the whole system. The fluid flow $\{\mathbf{u}, p\}$ at a given time is therefore fully determined by the instantaneous positions and velocities of the particle surfaces and wall boundaries, independently of how the momentary boundary values have been reached (history independence). In particular, the instantaneous fluid flow pattern does not depend on whether the boundary velocities will stay constant in the future or change, such as in oscillatory motions.

This feature of Stokes flows appears counter-intuitive on the first sight. Yet, there exist nice demonstrations highlighting its validity, provided the frequency of oscillatory boundary motions and the probed distances are not too large. Otherwise, hydrodynamic retardation effects come into play reflecting the actually non-instantaneous spreading of flow perturbations by pressure (sound) waves, and by the diffusional spreading of flow vorticity in the viscous fluid with an associated vorticity diffusion coefficient, η/ρ_f, equal to the kinematic viscosity [19, 27].

3.3 Kinematic reversibility

Kinematic reversibility is a remarkable feature of viscosity-dominated flows. The linearity of the Stokes equations in the flow fields $\{\mathbf{u}, p\}$ and the applied forces, including the ones due to the fluid boundaries, implies that under the reversion of the driving forces, the flow fields are also reversed to $\{-\mathbf{u}, -p\}$. Moreover, if the forces and also the history of their application is reversed, all fluid elements retrace their motion in the opposite direction along the unchanged streamlines.

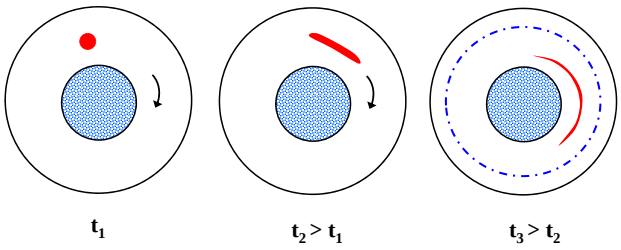

Fig. 5 Ink-spreading experiment by G. I. Taylor. An ink droplet inserted in a high-viscosity Newtonian fluid at time t_1 is smeared out in a thin concentric filament when the inner cylinder is rotated subsequently. The initial droplet shape is recovered after reversal of the rotation, independent of the rotation rate.

Kinematic reversibility was beautifully demonstrated in G. I. Taylor's video [20] from 1966, where a drop of coloured ink is immersed in highly viscous glycerine, to maintain low-Reynolds-number flow, filling the gap between two concentric cylinders (Couette cell geometry). See here Fig. 5. On rotating the inner cylinder, the drop is smeared out along concentric streamlines into a thin filament. When the rotation is reversed subsequently by the same number of turns, the original droplet is reconstituted up to a small amount of blurring originating from the irreversible residual Brownian motion of the dye particles. The length of the filament depends on the number of turns only, independent of the rate at which the inner cylinder is rotated. This nicely illustrates the earlier discussed instantaneity of Stokes flows.

The kinematic reversibility in combination with specific symmetries puts general constraints on the motion of microparticle in a viscous fluid. A classical example is a spherical rigid microparticle settling under gravity near a stationary vertical hard wall (see Fig. 6). While the particle is rotating clockwise during settling, owing to the larger wall-induced hydrodynamic friction on its semi-hemisphere facing the wall (see Subsec. 5.2 for details), a question arises whether it will approach the wall or recede from it. Given that gravity acts vertically downwards parallel to the wall, assume for the time being that the sphere approaches the wall while settling (see Fig. 6(a)). Kinematic reversibility requires that once the direction of the motion-driving gravitational force is reversed, the Stokes flow pattern remains unchanged except for the directional reversal of the fluid elements motion, provided the translational and angular particle velocities are likewise reversed. According to Fig. 6(b), this implies that the sphere sediments upwards while receding from the wall. On rotating Fig. 6(b) by 180° around the horizontal symmetry axis line going through the sphere centre, Fig. 6(c) is obtained in conflict with Fig. 6(a) wherein the sphere had been assumed to approach the wall. A contradiction is avoided only if the sphere remains at a constant distance from the wall while settling, as in Fig. 6(d). An analogous reasoning can be employed to show that in Poiseuille channel flow, a non-Brownian microsphere translates along the flow streamline, without any cross-flow velocity component.

As discussed in Subsec. 5.3, a non-spherical rigid particle, such as a rod, can move sidewise while settling and so approach the vertical wall. The wall-induced rotation of the particle can lead to a subsequent motion away from the wall. A deformable liquid droplet settling close to a vertical wall will deform into a shape which makes it glide away from the wall.

While non-spherical rigid particles and deformable particles can migrate across streamlines under Stokes flow conditions, this is not the case for an isolated non-Brownian spherical particle. However, the non-linear hydrodynamic coupling of the motions of three or more nearby spheres in a driven system such as in the pipe flow of a suspension, can lead to irregularly looking trajectories which depend sensitively on the initial particle configuration. Any reversibility-breaking slight perturbation of the initial particle configuration caused, e.g., by direct particle interactions in the form of surface roughness, flexibility or electric charge, or residual Brownian motion and inertia effects, becomes exponentially amplified, giving rise to chaotic trajectories causing cross-stream migration and the mixing of the particles. A macro-

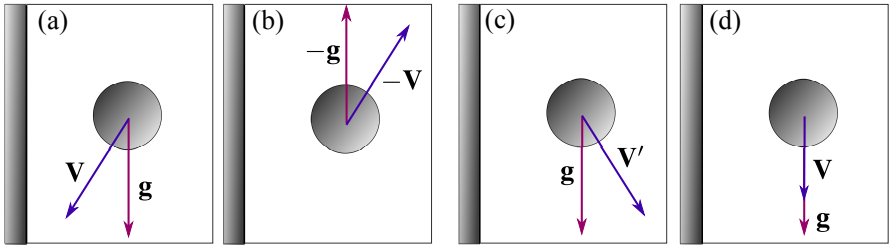

Fig. 6 A non-Brownian sphere settling with translational velocity **V** under gravity of field strength **g** near a vertical hard wall. The principle of kinematic reversibility in conjunction with the flow geometry leads to the conclusion that the sphere maintains a fixed distance from the wall while settling and rotating. See the text for details.

scopic manifestation of this so-called (anisotropic and temperature-independent) hydrodynamic diffusion is the flow-induced migration of spherical particles in concentrated suspensions from the regions of high to low shear rates. The shear-induced diffusion has an application, e.g., in the inside-out microfiltration (enrichment) of a particle suspension pumped through a microfluidic filter pipe where it reduces the formation of irreversible particle deposits at the filter membrane (fouling reduction).

Already on the particle pair-interaction level, the kinematic reversibility of rigid particles is broken by physical processes modifying the Stokes equations or the evolution of the particle trajectories such as non-Newtonian terms in the stress-shear relation (cf. Eq. (14)) occurring in viscoelastic media (e.g., in polymer solutions and melts), short-range repelling forces, significant Brownian motion and non-inertial hydrodynamic effects. For example, for Reynolds numbers significantly larger than zero, a particle immersed in a pipe flow experiences an inertia-induced lift force driving it away from the pipe wall. This so-called tubular pinch or Segre-Silberberg effect, named after its discoverers, appears already on the single-particle level and should be distinguished from the many-particle shear-induced diffusion effect which takes place under Stokes flow conditions of zero inertia.

4 Colloidal hydrodynamics in bulk fluid

On the time and length scales of colloidal dynamics, the fluid flow is described by means of the Stokes equations supplied by appropriate boundary conditions at interfaces and surfaces of suspended particles. Since the dynamics of these particulates is often of interest, one needs to construct a description of their interaction including the solvent-mediated hydrodynamic effects. In this Section, we introduce the notion of friction and mobility, and show how linearity of the Stokes equations can be used to construct relations between forces and velocities of particles in a many-body system in the case where the interfaces are far away and the fluid may be regarded to be unbounded. We then proceed to explore the basic solutions of the creeping

flow equations for point forces which are the simplest approximation to the flow field generated by the immersed particles. The set of solutions is then extended by multipole expansion to include more subtle flow effects. We apply this formalism to investigate the motion of shape-anisotropic slender bodies, such as rod-like colloids, and later on construct a solution for a spherical particle moving through the fluid as a result of a force, or by a phoretic motion. We conclude this Section by a discussion of more advanced approaches to hydrodynamic interactions and of the lubrication effects which are essential when the particles are very close together.

4.1 Friction and mobility of microparticles

We outline here the theoretical framework for the description of dynamics of a dispersion consisting of N rigid microparticles of basically arbitrary shape evolving under Stokes flows conditions [14]. Consider the particles to be at the instantaneous configuration $\mathbf{X} = (\mathbf{R}, \boldsymbol{\Theta}) = (\mathbf{R}_1, \ldots, \mathbf{R}_N, \boldsymbol{\Theta}_1, \ldots, \boldsymbol{\Theta}_N)$, with body-fixed particle position vectors $\{\mathbf{R}_i\}$ and orientations $\{\boldsymbol{\Theta}_i\}$. Here, $\boldsymbol{\Theta}_i$ abbreviates the three Euler angles characterizing the orientation of the particle i.

Suppose now that the particles are subjected to external forces $\mathbf{F} = (\mathbf{F}_1, \ldots, \mathbf{F}_N)$ and torques $\mathbf{T} = (\mathbf{T}_1, \ldots, \mathbf{T}_N)$ where we have introduced $3N$-dimensional supervectors $\mathbf{F}$ and $\mathbf{T}$ for notational convenience. As a consequence of this forcing, motion of the particles and the fluid is induced, and the particles acquire quasi-instantaneously the translational velocities $\mathbf{V} = (\mathbf{V}_1, \ldots, \mathbf{V}_N)$ and the rotational velocities $\boldsymbol{\Omega} = (\boldsymbol{\Omega}_1, \ldots, \boldsymbol{\Omega}_N)$. We have assumed a quiescent fluid for simplicity, meaning that the fluid would be at rest in the absence of particles. This implies, in particular, that there is no ambient flow caused, e.g., by confining boundary parts in relative motion. In the inertia-free Stokes flow system under consideration, each external force and torque are balanced by hydrodynamic drag force and torque. Owing to the linearity of the Stokes equations and the hydrodynamic boundary conditions, the forces (torques) and translational (rotational) velocities are linearly related according to

$$\begin{pmatrix} \mathbf{V} \\ \boldsymbol{\Omega} \end{pmatrix} = \boldsymbol{\mu}(\mathbf{X}) \cdot \begin{pmatrix} \mathbf{F} \\ \mathbf{T} \end{pmatrix}, \tag{22}$$

where the $6N \times 6N$ hydrodynamic mobility matrix $\boldsymbol{\mu}$ has the four $3N \times 3N$ submatrices

$$\boldsymbol{\mu}(\mathbf{X}) = \begin{pmatrix} \boldsymbol{\mu}^{tt}(\mathbf{X}) & \boldsymbol{\mu}^{tr}(\mathbf{X}) \\ \boldsymbol{\mu}^{rt}(\mathbf{X}) & \boldsymbol{\mu}^{rr}(\mathbf{X}) \end{pmatrix}. \tag{23}$$

The superscripts tt and rr label the purely translational and rotational mobility matrix parts, respectively. The off-diagonal matrices with superscripts tr and rt describe the hydrodynamic coupling between translational and rotational particle motions. The tensor elements of these matrices have a straightforward physical meaning. To give an example, the tensor $[\boldsymbol{\mu}^{tt}(\mathbf{X})]_{ij}$ relates the instant force $\mathbf{F}_j$ on particle j with the translational velocity $\mathbf{V}_i$ of particle i, in a situation where particles differ-

ent from j are all force- and torque-free. The coupling tensor $[\boldsymbol{\mu}^{rt}(\mathbf{X})]_{ij}$, on the other hand, relates the force $\mathbf{F}_j$ on particle j to the resulting angular velocity $\boldsymbol{\Omega}_i$ of particle i. It is important to note here that the mobility matrix $\boldsymbol{\mu}$ and its $4N^2$ mobility tensor elements depend on the configuration of the whole system, i.e. the instant positions and orientations of all particles, as well as on the particle shapes and sizes, and the surface boundary conditions. Finding the mobility tensor is therefore a very difficult problem which for arbitrary particle shapes can be addressed only numerically for a small number of particles.

It should be further noted that the form of the mobility matrix depends also on the selection of reference points $\mathbf{R}$ inside the particles. For these points, the so-called center of mobility of each particle should be selected which in Stokes flow dynamics plays a similar role as the center-of-mass position in Newtonian dynamics. For an axisymmetric homogeneous rigid body, the center-of-mobility and the center-of-mass are both located on the symmetry axis but they coincide not necessarily. They coincide, however, for a homogeneous sphere. Different from the center-of-mass, the center-of-volume is depending on the shape of the particle surface only, for uniform surface BC, independent of the mass distribution inside the particle. For a more detailed discussion of this important issue, see [14, 28].

In the simplest case of hydrodynamically non-interacting spherical particles of equal radius a, the tt and rr tensors reduce to the 3×3 unit matrices,

$$[\boldsymbol{\mu}^{tt}(\mathbf{X})]_{ij} = \mu_0^t \delta_{ij}, \qquad [\boldsymbol{\mu}^{rr}(\mathbf{X})]_{ij} = \mu_0^r \delta_{ij} \tag{24}$$

describing the free translation and rotation of isolated spheres. This limiting case is approached for an ultra-dilute dispersion where the mean distance between two particles is very large compared to their sizes. The single-particle mobility coefficients of a no-slip sphere are explicitly (see Subsec. 5.2)

$$\mu_0^t = \frac{1}{6\pi\eta a}, \qquad \mu_0^r = \frac{1}{8\pi\eta a^3} \tag{25}$$

with $\mathbf{V}_i = \mu_0^t \mathbf{F}_i$ and $\boldsymbol{\Omega}_i = \mu_0^r \mathbf{T}_i$. The tr and rt mobility tensors are here zero implying that there is no coupling between the translational and rotational motion of the particles.

Eq. (22) describes the so-called mobility problem where the forces and torques acting on the particles are given, and the translational and rotational velocities are searched for. The inverse problem where the velocities are given and the forces are searched for, referred to as the friction problem, is straightforwardly formulated by introducing the $6N\times 6N$ friction matrix

$$\boldsymbol{\zeta} = \boldsymbol{\mu}^{-1}. \tag{26}$$

defined as the inverse of the mobility matrix. That this inverse exists is due to the fact that $\boldsymbol{\mu}$ is symmetric and positive definite, for all physically allowed particle configurations. This follows from general principles of the Stokes flows, and it implies physically that the power supplied to the particles by external forces is completely

and quasi-instantaneously dissipated by heating the fluid. We quantify this statement for the motion of N torque-free microparticles in an infinite quiescent fluid where the rate of change of the particles kinetic energy, $W(t)$, instantaneously dissipated into heat by friction is given by

$$0 < \frac{dW(t)}{dt} = \begin{pmatrix} \mathbf{F} \\ \mathbf{T} \end{pmatrix} \cdot \begin{pmatrix} \mathbf{V} \\ \boldsymbol{\Omega} \end{pmatrix} = \begin{pmatrix} \mathbf{F} \\ \mathbf{T} \end{pmatrix} \cdot \boldsymbol{\mu}(\mathbf{X}) \cdot \begin{pmatrix} \mathbf{F} \\ \mathbf{T} \end{pmatrix}. \tag{27}$$

Since the $6N$-dimensional supervector with the particles forces and torques as elements is arbitrary, the second equality expresses the positive definiteness of the $6N \times 6N$ symmetric mobility matrix $\boldsymbol{\mu}^{tt}$. Any violation of the positive definiteness of this matrix would imply thus the violation of the second law of thermodynamics. In specializing Eq. (27) to torque-free and force-free particles, respectively, it follows readily the positive definiteness likewise of the $3N \times 3N$ symmetric submatrices $\boldsymbol{\mu}^{tt}$ and $\boldsymbol{\mu}^{rr}$ for all physically allowed particle configurations $\mathbf{X}$.

The knowledge of the configuration-dependence of $\boldsymbol{\mu}$, or likewise that of $\boldsymbol{\zeta}$, allows for exploration of the microparticles' dynamics using numerical simulations, without having to address explicitly the accompanying fluid flow. For torque-free particles large enough for their Brownian motions to be negligible, the $3N$ coupled first-order equations of motion for the particles centre-of-mobility positions, in presence of external and also non-hydrodynamic particle interaction forces all subsumed in $\mathbf{F}$, are given by

$$\frac{\mathrm{d}\mathbf{R}(t)}{\mathrm{d}t} = \boldsymbol{\mu}^{tt}(\mathbf{R}(t)) \cdot \mathbf{F}(t). \tag{28}$$

Integration of these evolution equations gives the positional trajectories of the particles. This is referred to as Stokesian dynamics [29]. Due to the non-linearity of the Stokesian dynamics evolution equations in Eq. (28), originating from the non-linear positional dependence of the mobility matrix, the trajectories are highly sensitive to the initial particle configuration: A slight change in the initial configuration can lead to large differences in the trajectorial evolution. Deterministic chaos in the trajectories of as little as three hydrodynamically interacting non-Brownian particles settling under gravity has been observed first in the point-particle limit [30] and later also for extended spheres [31].

For smaller Brownian particles, on the other hand, the mobility matrix is needed as input not only for the generation of Stokesian particle displacements, but also for the generation of additional stochastic displacements caused by the thermal fluctuations of the solvent. These displacements are the essential ingredients of the so-called Brownian dynamics numerical scheme for the generation of Brownian stochastic trajectories [32]. For a pedagogical introduction to Brownian dynamics simulations, see [33]. From the generated trajectories, quantities such as the particle mean-squared displacement in Eq. (10) can be calculated, for the general case of interacting microparticles. The positive definiteness of the mobility matrix plays a key role for Brownian particles. It guarantees that a perturbed suspension evolves towards thermodynamic equilibrium, in the absence of external forcing and ambient flow.

Complementary to the Stokesian dynamics and Brownian dynamics simulation schemes, the evolution of microparticle dispersions is studied theoretically also in terms of the probability density distribution function $P(\mathbf{X},t)$, where $P(\mathbf{X},t)d\mathbf{X}$ is the probability of finding N particles at time t in a small $6N$-dimensional neighbourhood $d\mathbf{X}$ of the configuration $\mathbf{X}$. The evolution equations for $P(\mathbf{X},t)$ for Brownian and non-Brownian particles under Stokes-flow conditions are, respectively, the many-particle Smoluchowski diffusion equation and the Stokes-Liouville equation. An introductory discussion of these equations is given in Ref. [9].

4.2 Method of singularity flow solutions

Linearity of the Stokes equations allows for the representation of the fluid velocity and pressure in dispersions of microparticles in terms of a discrete or continuous superposition of elementary flow solutions. We discuss in the following a very useful set of singularity incompressible flow solutions for an unbounded quiescent fluid which decay all to zero far away from a specified fluid point where they exhibit a pole singularity [14, 34, 35]. For simple geometries, this set can be profitably used to obtain, with little effort, exact Stokes flow solutions by linear superposition. We will exemplify this for the forced and phoretic motions of a microsphere, and for the velocity field of a point force in front of a fluid-fluid interface (see Subsec. 5.1). To solve the latter problem, an image method is used similar to that in electrostatics [36]. For more complicated geometries such as for a complex-shaped particle, the singularity method remains useful to gain information about the flow at far distances from the particle, in the form of a multipolar series. We shall demonstrate this in our discussion of the swimming trajectories of a self-propelling microswimmer near a surface.

The important observation is that for a given solution, $\{\mathbf{u},p\}$, of the homogeneous Stokes equations, its derivatives are likewise flow solutions. We can thus construct a complete set of singularity solutions by taking derivatives of increasing order, of two fundamental flow solutions, namely those due to a point force and a point source.

We should add that for dispersions of spherical particles, specialized elementary sets of Stokes flow solutions can be constructed, which are different from the singularity set discussed below, and which account for the high symmetry of spheres. These specific sets are used in numerically precise methods [37, 38] of calculating the many-sphere hydrodynamic mobility and friction coefficients required in Brownian and Stokesian dynamics simulations.

Point-force solution and Oseen tensor: The fundamental flow solutions, $\{\mathbf{u}_{\rm St},p_{\rm St}\}$, due to the body force density $\mathbf{f}(\mathbf{r})=\delta(\mathbf{r}-\mathbf{r}_0)\mathbf{F}$ of a point force $\mathbf{F}=F\mathbf{e}$, directed along the unit vector $\mathbf{e}$ and acting on a quiescent, infinite fluid at a position $\mathbf{r}_0$, can be obtained in several ways (see [39]). We only quote here the result

$$\mathbf{u}_{\mathrm{St}}(\mathbf{r}) = \mathbf{T}(\mathbf{r}-\mathbf{r}_0)\cdot\mathbf{F} \tag{29}$$

$$p_{\mathrm{St}}(\mathbf{r}) = \frac{1}{4\pi}\mathbf{U}_{\mathrm{S}}(\mathbf{r}-\mathbf{r}_0)\cdot\mathbf{F}. \tag{30}$$

The second-rank Oseen tensor, $\mathbf{T}(\mathbf{r})$, has the form

$$\mathbf{T}(\mathbf{r}) = \frac{1}{8\pi\eta}\frac{1}{r}\left(\mathbf{1}+\hat{\mathbf{r}}\hat{\mathbf{r}}\right), \tag{31}$$

where $\mathbf{1}$ is the unit tensor, $\mathbf{r} = r\hat{\mathbf{r}}$, and $\hat{\mathbf{r}}\hat{\mathbf{r}}$ is a dyadic tensor formed with the positional unit vector $\hat{\mathbf{r}}$. In Cartesian coordinates, the Oseen tensor elements read

$$T_{ij} = \frac{1}{8\pi\eta}\left(\frac{\delta_{ij}}{r}+\frac{r_i r_j}{r^3}\right). \tag{32}$$

The pressure field $p_{\mathrm{St}}(\mathbf{r})$ due to the point force at $\mathbf{r}_0$ is expressed here in terms of the elementary source vector field

$$\mathbf{U}_{\mathrm{S}}(\mathbf{r}) = \frac{\hat{\mathbf{r}}}{r^2} = -\nabla\frac{1}{r}. \tag{33}$$

If multiplied by a constant $c > 0$ with the dimension of volume per time, $c\,\mathbf{U}_{\mathrm{S}}(\mathbf{r})$ describes the radially directed outflow of fluid from the source point $\mathbf{r}_0 = \mathbf{0}$. The flow rate through a surface S enclosing the source point is thus equal to

$$c\int_S dS\,\mathbf{U}_{\mathrm{S}}\cdot\mathbf{n} = 4\pi c\,. \tag{34}$$

The elementary velocity field $\mathbf{u}_{\mathrm{St}}(\mathbf{r})$ of a point-force is called a Stokeslet of strength F in the direction of $\mathbf{e}$, and with the centre at $\mathbf{r}_0$ where it has a simple pole singularity. Note here that T_{ij} is the i-th component of the Stokeslet velocity field generated by a unit force acting in the j direction. The streamlines of the Stokeslet are drawn as dashed lines in the left part of Fig. 9, together with those generated by a spherical no-slip particle subjected to the same force. The hydrodynamics of a translating sphere is discussed in detail further down. A significant difference between the two streamlines pattern exterior to the impermeable sphere is visible only near its surface. The streamlines generated by the translating sphere are further out indistinguishable from those of the point-force Stokeslet.

The Stokeslet velocity field decays like $1/r$ at far distances from the point force. This slow decay can be ascribed to the conservation of momentum injected into the fluid by the point force, which is spread out quasi-instantaneously. It creates major difficulties in dealing theoretically with the hydrodynamics of suspensions, since forced velocity disturbances influence even well-separated particles. An additional difficulty is that the hydrodynamic interactions between three and more non-point-like particles is not pairwise additive, i.e. the hydrodynamic interactions of two nearby particles is changed in a rather complicated way if a third one is in their vicinity.

According to Eq. (33), the pressure field of a point force decays faster than the velocity field by the factor of $1/r$. Note that the pressure itself, and not just its gradient, has been uniquely specified by demanding $p \to 0$ for $r \to \infty$. Employing Eq. (14), the stress on a fluid surface element at position $\mathbf{r}$ and normal $\mathbf{n}$, due to a point force at the coordinate system origin, is

$$\boldsymbol{\sigma}_{\mathrm{St}}(\mathbf{r}) \cdot \mathbf{n}(\mathbf{r}) = -\frac{3}{4\pi}\mathbf{F} \cdot \left(\frac{\hat{\mathbf{r}}\hat{\mathbf{r}}\hat{\mathbf{r}}}{r^2} \right) \cdot \mathbf{n} = -\frac{3}{4\pi} \frac{(\hat{\mathbf{r}} \cdot \mathbf{F})(\hat{\mathbf{r}} \cdot \mathbf{n})}{r^2} \hat{\mathbf{r}}. \tag{35}$$

On integrating the stress over a surface enclosing the point force, the expected result $\mathbf{F}^h = -\mathbf{F}$ is obtained.

That the pressure field decays by the factor $1/r$ faster than the associated velocity field is a general rule. It follows from the homogeneous Stokes equation written in the form $\nabla p = \eta \nabla^2 \mathbf{u}$, where the first-order derivatives of p are expressed by the second-order derivatives of $\mathbf{u}$. It can be also noticed here that the pressure in Stokes flows is a subsidiary quantity, fully determined by the velocity field for BCs invoking velocities only. The velocity field can be calculated without reference to the pressure as a solution of the bi-harmonic differential equation

$$\nabla^2 \nabla^2 \mathbf{u}(\mathbf{r}) = \mathbf{0}, \tag{36}$$

which readily follows from the application of the divergence operation to the homogeneous Stokes equation, using in addition the flow incompressibility constraint.

For completeness, consider also the vorticity field, $\nabla \times \mathbf{u}(\mathbf{r})$, associated with a velocity field $\mathbf{u}(\mathbf{r})$. The vorticity is twice the angular velocity of a fluid element at $\mathbf{r}$. The vorticity due to a point force at position $\mathbf{r}_0$ is

$$\nabla \times \mathbf{u}_{\mathrm{St}}(\mathbf{r}) = -\frac{1}{4\pi\eta} \mathbf{U}_{\mathrm{S}}(\mathbf{r} - \mathbf{r}_0) \times \mathbf{F}, \tag{37}$$

identifying the Stokeslet as an incompressible rotational flow solution.

The Oseen tensor for an unbounded infinite fluid is of key importance not only in generating higher-order elemental force singularity solutions (see below), but also for the so-called boundary integral method of calculating the flow around complex-shaped bodies. The disturbance flow, i.e. the flow taken relative to a given ambient flow field $\mathbf{u}_{\mathrm{amb}}(\mathbf{r})$, observed in the exterior of a rigid no-slip particle in infinite fluid is given by the integral

$$\mathbf{u}(\mathbf{r}) - \mathbf{u}_{\mathrm{amb}}(\mathbf{r}) = \int_{S_p} dS' \, \mathbf{T}(\mathbf{r} - \mathbf{r}') \cdot \boldsymbol{\sigma}(\mathbf{r}') \cdot \mathbf{n}(\mathbf{r}'), \tag{38}$$

over the particle surface S_p, i.e. by a continuous superposition of surface-located Stokeslets of vectorial strength $\boldsymbol{\sigma} \cdot \mathbf{n}$. We emphasize here that if the fluid at S_p is tangentially mobile such as for a rigid particle with Navier partial-slip BC, and a liquid droplet or gas bubble, there is an additional surface integral contribution to the exterior flow. The form of this additional contribution is discussed in detail in textbooks on low-Reynolds-number fluid dynamics [14, 35, 40].

The ambient velocity field $\mathbf{u}_{\text{amb}}(\mathbf{r})$ is a Stokes flow caused by sources exterior to the considered particle. In a non-quiescent situation it can be, e.g., a linear shear or quadratic Poiseuille flow. The ambient flow can be also the flow due to the motion of other rigid or non-rigid particles. If the considered particle was not present, the ambient flow would be measured in the system.

Integrating Eq. (38) with respect to $\mathbf{r}$ over the particle surface, and using the no-slip BC in Eq. (3) for its left-hand side, results in a linear surface integral equation for the surface stress field $\boldsymbol{\sigma}\cdot\mathbf{n}$ in terms of the given translational and rotational particle velocities $\mathbf{V}$ and $\boldsymbol{\Omega}$, and the ambient flow field (friction problem). The integral equation can be solved numerically by an appropriate surface discretization (triangulation). For given particle force and torque (mobility problem), and given ambient flow, the velocities are determined from substituting the calculated stress field into the likewise discretized Eq. (15) for $\mathbf{F}^h$ and $\mathbf{T}^h$. See here [8, 9, 35] for details on the boundary integral method which has the main advantage of requiring only a two-dimensional surface mesh for a three-dimensional flow calculation.

Force multipoles solutions: Singularity solutions of increasing multipolar order are obtained from derivatives of the fundamental flow solution $\mathbf{u}_{\text{St}}(\mathbf{r})$. They also show up in the expansion of $\mathbf{u}_{\text{St}}$ in a Taylor series about the force placement (singularity) point $\mathbf{r}_0$. Recall now that point force $\mathbf{F}=F\mathbf{e}$ oriented along the direction $\mathbf{e}$ generates the velocity field

$$\mathbf{u}_{\text{St}}(\mathbf{r}-\mathbf{r}_0)=\frac{F}{8\pi\eta}\mathbf{G}(\mathbf{r}-\mathbf{r}_0;\mathbf{e})\,, \tag{39}$$

with

$$\mathbf{G}(\mathbf{r};\mathbf{e})=8\pi\eta\mathbf{T}(\mathbf{r})\cdot\mathbf{e}=\frac{\mathbf{e}}{r}+\frac{\mathbf{e}\cdot\mathbf{r}}{r^3}\mathbf{r}\,. \tag{40}$$

We select $\mathbf{G}(\mathbf{r};\mathbf{e})$ as the starting element of the singularity set, quoting it as the fundamental $\mathbf{e}$-directed Stokeslet. It is actually equal to a Stokeslet of unit force in the direction $\mathbf{e}$, made non-dimensional by multiplication with $8\pi\eta$ and division by the force unit. The first two singularity solutions obtained from directional derivatives of the fundamental Stokeslet are the Stokeslet doublet $\mathbf{G}_{\text{D}}$, and the Stokeslet quadrupole $\mathbf{G}_{\text{Q}}$ [26, 41]

$$\mathbf{G}_{\text{D}}(\mathbf{r}-\mathbf{r}_0;\mathbf{d},\mathbf{e})=(\mathbf{d}\cdot\nabla_0)\,\mathbf{G}(\mathbf{r}-\mathbf{r}_0;\mathbf{e})\sim\mathscr{O}\left(r^{-2}\right), \tag{41}$$

$$\mathbf{G}_{\text{Q}}(\mathbf{r}-\mathbf{r}_0;\mathbf{c},\mathbf{d},\mathbf{e})=(\mathbf{c}\cdot\nabla_0)\,\mathbf{G}_{\text{D}}(\mathbf{r}-\mathbf{r}_0;\mathbf{d},\mathbf{e})\sim\mathscr{O}\left(r^{-3}\right), \tag{42}$$

where the gradient operator ∇_0 acts on the singularity placement $\mathbf{r}_0$, and $\mathbf{d}$ and $\mathbf{c}$ are arbitrary vectors. We have indicated here the decay of these velocity fields far distant from the singularity point. Higher-order singularity flow solutions with an $\mathscr{O}(r^{-4})$ asymptotic decay are obtained accordingly by repeated differentiation. For later use, we explicitly quote the Stokeslet doublet,

$$\mathbf{G}_{\mathrm{D}}(\mathbf{r};\mathbf{d},\mathbf{e}) = \mathbf{d}\cdot\frac{1}{r^2}\left[\hat{\mathbf{r}}\mathbf{1} - \mathbf{1}\hat{\mathbf{r}} - {}^{T}(\hat{\mathbf{r}}\mathbf{1}) + 3\,\hat{\mathbf{r}}\hat{\mathbf{r}}\hat{\mathbf{r}}\right]\cdot\mathbf{e} \tag{43}$$

$$= \frac{1}{r^2}\Big[\mathbf{e}(\hat{\mathbf{r}}\cdot\mathbf{d}) - \mathbf{d}(\hat{\mathbf{r}}\cdot\mathbf{e}) - (\mathbf{d}\cdot\mathbf{e})\hat{\mathbf{r}} + 3\,(\hat{\mathbf{r}}\cdot\mathbf{e})(\hat{\mathbf{r}}\cdot\mathbf{d})\hat{\mathbf{r}}\Big]\,. \tag{44}$$

where the pre-transposition symbol implies the interchange of the first two Cartesian indices. The Stokes doublet $\mathbf{G}_{\mathrm{D}}(\mathbf{r};\hat{\mathbf{d}},\mathbf{e})$, with $\hat{\mathbf{d}}$ denoting a unit vector, has the following physical interpretation: It is the velocity field times $8\pi\eta$, of two opposing Stokelets of vector strengths $\pm F\mathbf{e}$ and singularity locations at $\mathbf{r}_0 \pm \mathbf{d}$ (with $\mathbf{d} = d\hat{\mathbf{d}}$), in the limits $d \to 0$ and $F \to \infty$ with the force dipole moment $p = 2Fd$ kept constant equal to one. The unit vector $\hat{\mathbf{d}}$ points from the Stokeslet of strength $-F\mathbf{e}$ to the one of strength $F\mathbf{e}$. This interpretation is obviated from the explicit calculation of the flow field,

$$\begin{aligned}\mathbf{u}_{\mathrm{D}}(\mathbf{r}) &= \left[\mathbf{T}(\mathbf{r}-\mathbf{r}_0-\mathbf{d}) - \mathbf{T}(\mathbf{r}-\mathbf{r}_0+\mathbf{d})\right]\cdot\mathbf{e}F = 2dF\left(\hat{\mathbf{d}}\cdot\nabla_0\right)\mathbf{T}(\mathbf{r}-\mathbf{r}_0)\cdot\mathbf{e} + \mathscr{O}(d^2)\\ &= \frac{p}{8\pi\eta}\mathbf{G}_{\mathrm{D}}(\mathbf{r}-\mathbf{r}_0;\hat{\mathbf{d}},\mathbf{e}) + \mathscr{O}(d^2)\,.\end{aligned} \tag{45}$$

The force doublet provides the far-field behaviour of flows caused by force-free microparticles. It is named asymmetric when $\hat{\mathbf{d}}$ is not collinear with the force direction $\pm\mathbf{e}$, and referred to as symmetric otherwise. The symmetric force doublet $\mathbf{G}_{\mathrm{D}}(\mathbf{r}-\mathbf{r}_0;\mathbf{e},\mathbf{e})$ is also called a linear force dipole. It plays a major role in the discussion of the flow created by many autonomous microswimmers, including various types of prokaryotic bacteria and eukaryotic unicellular microorganisms. Microswimmers in the bulk fluid and near interfaces are discussed in Sec. 6.

The force doublet can be split into an anti-symmetric part, named Rotlet $\mathbf{R}$, and a symmetric part named Stresslet $\mathbf{S}$, each of which has a direct physical meaning. We exemplify this for the Rotlet and in the special situation where the force strengths of the two opposing Stokeslets are orthogonally displaced, and aligned with the z-axis and x-axis, respectively. Then, $\mathbf{F}\cdot\mathbf{d} = 0$ and the dipole moment $T = 2dF$ has the meaning of an applied torque. The Rotlet at the singularity point $\mathbf{r}_0 = \mathbf{0}$ is in this case

$$\mathbf{R}(\mathbf{r};-\mathbf{e}_y) = \frac{1}{2}\left[\mathbf{G}_{\mathrm{D}}(\mathbf{r};\mathbf{e}_x,\mathbf{e}_z) - \mathbf{G}_{\mathrm{D}}(\mathbf{r};\mathbf{e}_z,\mathbf{e}_x)\right] = -\mathbf{e}_y\times\frac{\hat{\mathbf{r}}}{r^2}\,, \tag{46}$$

and after division by the factor $8\pi\eta$ it describes the rotational flow field due to a unit point torque aligned with the negative y-axis.

The symmetric Stresslet part reads

$$\begin{aligned}\mathbf{S}(\mathbf{r};\mathbf{e}_\pm) &= \frac{1}{2}[\mathbf{G}_{\mathrm{D}}(\mathbf{r};\mathbf{e}_x,\mathbf{e}_z) + \mathbf{G}_{\mathrm{D}}(\mathbf{r};\mathbf{e}_z,\mathbf{e}_x)] = \frac{3\,\hat{\mathbf{r}}}{r^2}(\hat{\mathbf{r}}\cdot\mathbf{e}_x)(\hat{\mathbf{r}}\cdot\mathbf{e}_Z)\\ &= \mathbf{G}_{\mathrm{D}}(\mathbf{r};\mathbf{e}_+,\mathbf{e}_+) - \mathbf{G}_{\mathrm{D}}(\mathbf{r};\mathbf{e}_-,\mathbf{e}_-)\,.\end{aligned} \tag{47}$$

It describes a straining fluid motion [14] originating from the superposition two linear force dipoles oriented along the diagonal stretching axis $\mathbf{e}_+$ and the anti-diagonal compression axis $\mathbf{e}_-$, respectively, where $\mathbf{e}_\pm = (\mathbf{e}_x \pm \mathbf{e}_z)/\sqrt{2}$. The streamlines of a linear force dipole are discussed in Sec. 6, and are drawn in Fig. 27.

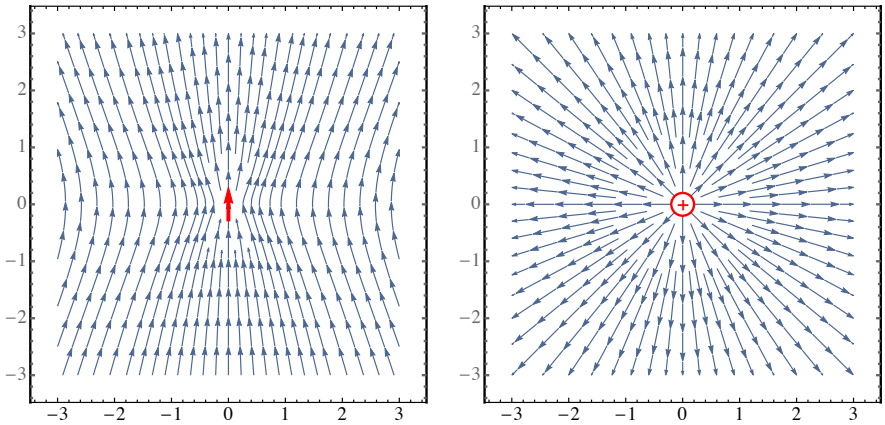

(a) Stokeslet $\mathbf{G}(\mathbf{e}_z) \sim \mathscr{O}(r^{-1})$ (b) Source $\mathbf{U}_\mathrm{S}(\mathbf{r}) \sim \mathscr{O}(r^{-2})$

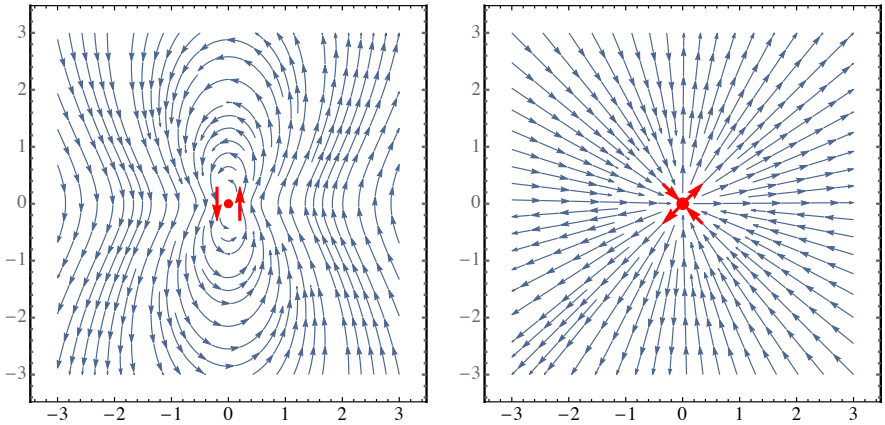

(c) Stokeslet doublet $\mathbf{G}_\mathrm{D}(\mathbf{r};\mathbf{e}_x,\mathbf{e}_z) \sim \mathscr{O}(r^{-2})$ (d) Stresslet $\mathbf{S}(\mathbf{r};\mathbf{e}_\pm) \sim \mathscr{O}(r^{-2})$

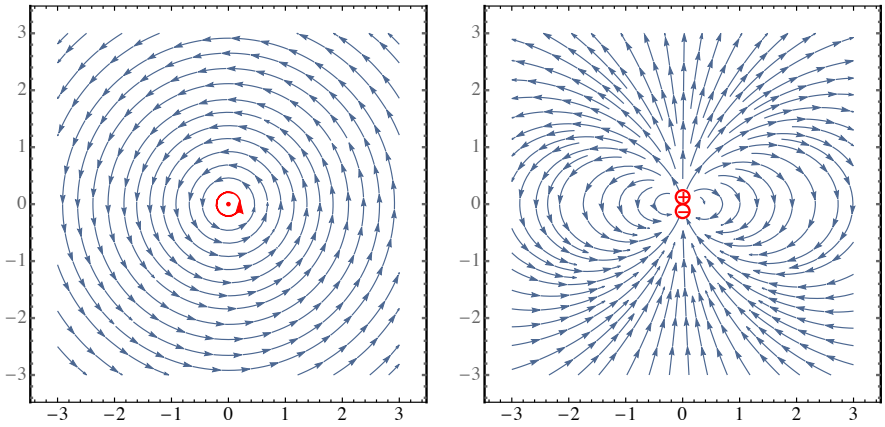

(e) Rotlet $\mathbf{R}(\mathbf{r};-\mathbf{e}_y) \sim \mathscr{O}(r^{-2})$ (f) Source doublet $\mathbf{D}_\mathrm{S}(\mathbf{r};\mathbf{e}_z) \sim \mathscr{O}(r^{-3})$

Fig. 7 A few elemental singularity solutions used in constructing specific Stokes flow solutions. The x-axis points horizontally to the right, and the z-axis vertically upwards. The singularities are marked in red with pictograms reflecting their structure. Note here that $\mathbf{G}_\mathrm{D}(\mathbf{r};\mathbf{e}_x,\mathbf{e}_z) = -\mathbf{G}_\mathrm{D}(\mathbf{r};\mathbf{e}_z,\mathbf{e}_x)$, and $\mathbf{e}_\pm = (\mathbf{e}_x \pm \mathbf{e}_z)/\sqrt{2}$ span the stretching and compression axes. The elemental source, $-\mathbf{U}_\mathrm{S}(\mathbf{r})$, is marked as a circle with a minus sign inside.

The key point to notice here is that the stresses $\boldsymbol{\sigma}_{\mathbf{S}} \cdot \mathbf{n}$ and $\boldsymbol{\sigma}_{\mathbf{R}} \cdot \mathbf{n}$, associated with the Stresslet and Rotlet force doublet parts, respectively, are decaying as $\mathscr{O}(1/r^3)$. When these stresses are integrated over a surface enclosing the singularity point, according to Eq. (15) they do not contribute a hydrodynamic drag force. Differently from the Stresslet which is torque-free, the Rotlet contributes a hydrodynamic torque of magnitude equal to $8\pi\eta$ times the torque unit. The stress fields of all the higher-order force singularity solutions including the one by the force quadrupole $\mathbf{G}_Q$ are all of $\mathscr{O}(1/r^4)$, so that they contribute neither a drag force nor a torque [8, 9].

Source multipoles solutions: Elementary singularity solutions in addition to the force singularities are obtained from derivatives of the source vector field $\mathbf{U}_{\mathrm{S}}(\mathbf{r}-\mathbf{r}_0)$ in Eq. (33) with respect to the singularity (source) point $\mathbf{r}_0$. The two leading-order flows obtained in this way are the source doublet (dipole) and quadrupole,

$$\mathbf{D}_{\mathrm{S}}(\mathbf{r}-\mathbf{r}_0;\mathbf{e}) = (\mathbf{e}\cdot\nabla_0)\mathbf{U}_{\mathrm{S}}(\mathbf{r}-\mathbf{r}_0) \sim \mathscr{O}(r^{-3}) \tag{48}$$

$$\mathbf{Q}_{\mathrm{S}}(\mathbf{r}-\mathbf{r}_0;\mathbf{d},\mathbf{e}) = (\mathbf{d}\cdot\nabla_0)\mathbf{D}_{\mathrm{S}}(\mathbf{r}-\mathbf{r}_0;\mathbf{e}) \sim \mathscr{O}(r^{-4})\,. \tag{49}$$

The source doublet multiplied by a constant c of dimension volume per time describes the flow due to a source flow with outflow rate $4\pi c$, and a sink flow of the same inflow rate. The source at $\mathbf{r}_0 + d\mathbf{e}$ and the sink of the doublet at $\mathbf{r}_0 - d\mathbf{e}$ are an infinitesimal vector distance $2d\mathbf{e}$ separated from each other and have the moment $2dc$ equal to one. Explicitly,

$$\mathbf{D}_{\mathrm{S}}(\mathbf{r};\mathbf{e}) = \frac{1}{r^3}\left[3\hat{\mathbf{r}}\hat{\mathbf{r}} - \mathbf{1}\right]\cdot\mathbf{e} = \frac{1}{r^3}\left[3\,(\hat{\mathbf{r}}\cdot\mathbf{e})\,\hat{\mathbf{r}} - \mathbf{e}\right]. \tag{50}$$

The source singularity solutions are related to the force singularity solutions by

$$\mathbf{D}_{\mathrm{S}}(\mathbf{r}-\mathbf{r}_0) = -\frac{1}{2}\nabla_0^2\mathbf{G}(\mathbf{r}-\mathbf{r}_0)\,, \tag{51}$$

and its derivatives. Eq. (51) identifies the source doublet as a degenerate force quadrupole, which explains its faster decay than that of the force doublet. The stress fields of the source multipoles decay as $\mathscr{O}(1/r^4)$ or faster, except for the source flow $\mathbf{U}_{\mathrm{S}}$ itself, implying that they make no force and torque contributions. As the derivatives of the Coulomb-type potential $1/r$ (see Eq. (33)), the source multipoles belong to the class of irrotational potential flows (where $\nabla\times\mathbf{u} = \mathbf{0}$) with associated constant pressure fields. To understand the pressure constancy, note with $\mathbf{u} = \nabla\psi$ for some scalar (potential) function that incompressibility implies $\Delta\psi = 0$. It follows with the Stokes equation that $\nabla p = \eta\Delta\,(\nabla\psi) = \eta\nabla(\Delta\psi) = \mathbf{0}$.

Superposition of singularity solutions: Linear superposition of fundamental singularity solutions, appropriately selected and positioned to conform with the system symmetry and BCs under consideration, can be profitably used to construct (approximate) flow solutions. The coefficients in the superposition series can be determined from the prescribed BCs.

As an example of such a superposition, in Subsec. 4.3 we discuss the gravitational settling of a slender body whose flow field can be described in decent approximation by a continuous distribution of Stokeslets placed along the body's center line.

For a particle axisymmetric along the direction **e**, and in a flow situation sharing this axial symmetry, the appropriate superposition describing the far-distance velocity field is

$$\mathbf{u}(\mathbf{r}) = c_1 \left(a\,\mathbf{G}(\mathbf{r};\mathbf{e})\right) + c_2 \left(a^2\,\mathbf{G}_{\mathrm{D}}(\mathbf{r};\mathbf{e};\mathbf{e})\right) + c_3 \left(a^3\,\mathbf{S}_{\mathrm{D}}(\mathbf{r};\mathbf{e})\right) + \mathscr{O}(r^{-4})\,, \quad (52)$$

with scalar coefficients $\{c_i\}$ having the physical dimension of a velocity. The centroid $\mathbf{r}_0$ of the particle placed is placed here in the origin, and a can be taken as the lateral length of the particle. The Rotlet part of the symmetric force doublet $\mathbf{G}_{\mathrm{D}}$ is zero here, since a torque-free, non-rotating particle is required by the symmetry of the flow problem. If the particle moves force-free along its axial direction, as it is the case for a self-propelling microswimmer, there is no Stokeslet contribution so that $c_1 = 0$. On the other hand, if the particle is sedimenting along its axis, the co-linear driving force is given by

$$\mathbf{F} = c_1\,(8\pi\eta a)\,\mathbf{e}\,, \quad (53)$$

with the coefficient c_1 determining the strength of the Stokeslet depending on the particle BCs. In Subsec. 4.4, we show that the flow created by a sphere translating through a quiescent fluid, is exactly represented by the superposition of a Stokeslet and a source dipole, owing to the high symmetry of this flow problem. If the sphere is placed in an ambient linear shear flow where the stress distribution on its surface becomes non-uniform, then a more general superposition of singularity solutions must be used including a source quadrupole, which in addition accounts for all relevant Cartesian directions, to obtain the exact flow solution [42]. Note also that for a translating spheroid, a line distribution of Stokeslets and source doublets extending between the focal points must be used [34]. As it is explained in Sec. 5.1, an appropriate placement of elemental singularity solutions at a reflection point provides an analytic solution for the velocity field of a point force in the presence of a fluid-fluid interface.

4.3 Slender body motion

As a first application, we use the force singularity method to determine the hydrodynamic friction experienced by a settling rigid slender body, that is a particle without sharp corners whose contour length, L, is large compared to its thickness d. Examples of such bodies include rod-like particles, and elongated or prolate spheroids. Owing to the shape anisotropy, the friction force depends on the orientation of the body relative to the direction of motion. The slenderness of the body renders it possible, in place of having to solve a complicated boundary integral problem for a no-slip particle on the basis of Eq. (38), to describe approximately the disturbance flow

field caused by its motion as that of a line of Stokeslets, uniformly distributed along the axis of the particle. The surface integration reduces then to a one-dimensional integral over a line of Stokeslets. This concept is originally due to Batchelor [43].

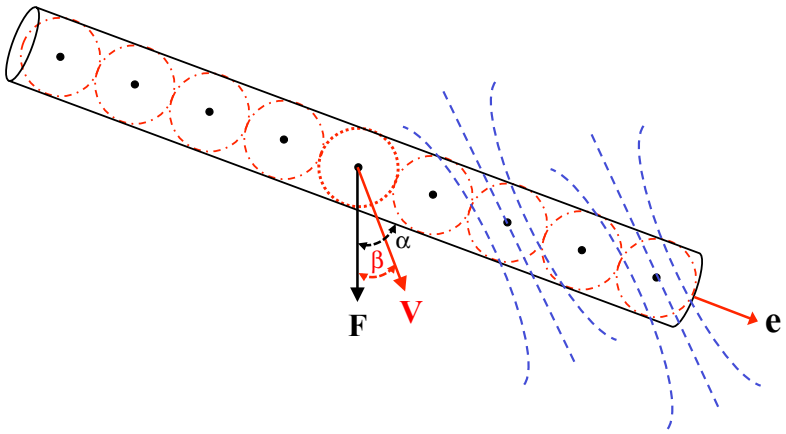

Fig. 8 A thin rod-shaped particle translating with velocity **V** under the action of an applied force **F** pointing downwards. The stress distribution on the rod surface is approximated by a line of equally-spaced and equally strong Stokeslets placed in the centres of the large number of spherical beads building up the rod. The flow lines of two of the superposing Stokeslets are sketched. The tilt angle α of the rod with respect to the applied force is in general different from the sedimentation angle β, resulting in a sidewise velocity component. Reproduced from the COMPLOIDS book [9] with kind permission of the Societa Italiana di Fisica.

To demonstrate this, consider the sedimentation of a thin rigid rod of length L and diameter $d \ll L$ translating with velocity **V** through an unbounded quiescent fluid, in response to an external force **F** due, e.g., to gravity. We approximate the flow created by the particle by the sum of $2n+1$ Stokeslets, placed in the centres of spherical beads of diameter d building up the rod in the form of a necklace (see Fig. 8). Each Stokeslet is assumed to have the same strength $(d/L)\mathbf{F}$, disregarding the end effects which are small for long rods. The rod is oriented along the unit vector **e** as depicted in the figure. On identifying, according to $\mathbf{V} = \mathbf{u}(\mathbf{0})$, the rod velocity with the velocity of the central bead under the hydrodynamic influence of the $2n$ other ones, the superposition of the $2n$ Stokeslets fields at the central bead position gives

$$\mathbf{V} = \frac{d}{\zeta^0_{\text{bead}} L}\mathbf{F} + \sum_{\substack{i=-n,\\ n\neq 0}}^{n} \mathbf{T}(id\mathbf{e})\cdot\frac{d}{L}\mathbf{F} \approx \frac{1}{4\pi\eta L}\left(\sum_{i=1}^{n}\frac{1}{i}\right)(\mathbf{1}+\mathbf{ee})\cdot\mathbf{F}, \qquad (54)$$

where the sum behaves like $\log n \approx \log L/d$ for large n, and where $\zeta^0_{\text{bead}} = 3\pi\eta d$ is the no-slip single-bead friction coefficient. On noting that $\mathbf{F}^h = -\mathbf{F}$, the result of this summation is the force-velocity friction problem relation

$$\mathbf{F}^h = -\left[\zeta_{\parallel}^{tt}\mathbf{ee} + \zeta_{\perp}^{tt}(\mathbf{1}-\mathbf{ee})\right]\cdot\mathbf{V}, \tag{55}$$

and likewise the inverse relation,

$$\mathbf{V} = -\left[\mu_{\parallel}^{tt}\mathbf{ee} + \mu_{\perp}^{tt}(\mathbf{1}-\mathbf{ee})\right]\cdot\mathbf{F}^h, \tag{56}$$

for the mobility problem of given force. The friction and mobility coefficients for the translation of a thin rod parallel and perpendicular to its axis **e** have been obtained here as

$$\zeta_{\parallel}^{tt} = \frac{1}{\mu_{\parallel}^{tt}} = \frac{2\pi\eta L}{\log(L/d)}, \qquad \zeta_{\perp}^{tt} = \frac{1}{\mu_{\perp}^{tt}} = 2\zeta_{\parallel}^{tt}. \tag{57}$$

Corrections to this asymptotic result from a refined hydrodynamic calculation for a cylinder with end effects included are provided in [44]. Note that the application, i.e. dot-multiplication, of the dyadic $(\mathbf{1}-\mathbf{ee})$ to a vector gives the component of this vector perpendicular to **e**.

Remarkably, the friction coefficient for the broadside motion of a thin rod is only twice as large as that for the axial motion. Both coefficients scale essentially with the length L of the rod, so that the drag force acting on a thin rod is not far less than that experienced by a sphere of diameter L enclosing it. It should be noted here that from general properties of Stokes flows it follows that the magnitude of the drag force on an arbitrarily-shaped body is always in between those for the inscribing and enclosing spheres [8, 14].

It is interesting to analyse the effect of the friction anisotropy on the direction of sedimentation. Denoting as α the angle between the rod axis $\hat{\mathbf{e}}$ and the applied force **F**, and as β the angle between rod velocity and applied force, we can relate the two angles by decomposing the external force into its components along and perpendicular to the rod axis, with the accompanying components of **V** determined by the mobility coefficients. In this way, one obtains

$$\beta = \alpha - \arctan\left(\tfrac{1}{2}\tan\alpha\right). \tag{58}$$

For a vertically or horizontally oriented rod and the applied force pointing downwards (see again Fig. 8), there will be no sidewise rod motion due to symmetry. Except for these special configurations, however, the tilt angle α of the rod is different from its sedimentation angle β, although both will remain constant during the motion. The maximum settling angle $\beta_{\max} = \arctan(\sqrt{2}/4) \approx 19.5^\circ$ corresponds to $\alpha \approx 54.7^\circ$.

Kinematic reversibility in conjunction with the system symmetry (no nearby walls are present here) commands that the rod is settling without rotation. The friction asymmetry of rod-shaped particles discussed here is a key ingredient in the swimming strategy of microswimmers with helical flagellar propulsion.

An elementary introduction to the concept of slender body motion is contained in the works [11, 14]. For a general discussion of slender bodies, which may also be curved, see [45, 46].

4.4 Forced translation of a microsphere

We consider here a microsphere of radius a with Navier partial slip BCs, which translates with constant velocity $\mathbf{V}_0 = V_0\mathbf{e}$ and without rotation through an unbounded quiescent fluid. The origin of the coordinate system is placed at the momentary sphere center. We attempt to describe the exterior fluid velocity ($r \geq a$) by the linear superposition of a Stokeslet and source doublet in accord with Eq. (52), and with the coefficients c_1 and c_3 determined by the BCs. It is convenient to express $\mathbf{u} = u_r\hat{\mathbf{r}} + u_\theta\mathbf{e}_\theta$ and $\mathbf{V}_0 = V_{0,r}\hat{\mathbf{r}} + V_{0,\theta}\mathbf{e}_\theta$ in polar coordinates with components

$$\begin{aligned} u_r(r,\theta) &= 2\cos\theta\left[c_1\left(\frac{a}{r}\right) + c_3\left(\frac{a}{r}\right)^3\right], \;\; V_{0,r} = V_0\cos\theta \\ u_\theta(r,\theta) &= -\sin\theta\left[c_1\left(\frac{a}{r}\right) - c_3\left(\frac{a}{r}\right)^3\right], \;\; V_{0,\theta} = -V_0\sin\theta \end{aligned} \tag{59}$$

where $\mathbf{e}\cdot\hat{\mathbf{r}} = \cos\theta$ and $\mathbf{e}\cdot\mathbf{e}_\theta = -\sin\theta$ have been used, with θ denoting the angle between polar axis $\mathbf{e}$ and fluid position vector $\mathbf{r}$. The two coefficients can be determined from enforcing the BC of zero normal velocity difference between the sphere and the fluid at the surface, $u_r(a,\theta) = V_{0,r}$, in conjunction with the Navier partial slip condition in Eq. (18) for the tangential velocity part. The latter is formulated in terms of the fluid velocity in the particle rest frame,

$$\mathbf{u}'(\mathbf{r}) = \mathbf{u}(\mathbf{r}) - \mathbf{V}_0\,, \tag{60}$$

labelled by the prime, where the fluid far away from the stationary sphere is moving with uniform velocity $-\mathbf{V}_0$. The Navier BC reads

$$u'_\theta(r,\theta) = \frac{\ell}{\eta}\left(\frac{\partial u'_\theta}{\partial r} - \frac{u'_\theta(r,\theta)}{a}\right), \quad (r=a) \tag{61}$$

The two coefficients are determined from the BCs as

$$c_1 = \frac{3V_0}{4}\left(\frac{1+2\ell^*}{1+3\ell^*}\right), \quad c_3 = -\frac{V_0}{4}\left(\frac{1}{1+3\ell^*}\right), \tag{62}$$

where $\ell^* = \ell/a$.

Using Eq. (53), the hydrodynamic drag force opposing the motion of the sphere follows from the Stokeslet contribution as

$$\mathbf{F}^h = -\left(8\pi\eta a c_1\right)\mathbf{e} = -6\pi\eta a\left(\frac{1+2\ell^*}{1+3\ell^*}\right)\mathbf{V}_0\,. \tag{63}$$

Note that the single-sphere friction coefficient, $\zeta_0^t = 1/\mu_0^t$, relating the velocity of an isolated sphere to its drag force according to

$$\mathbf{F}^h = -\zeta_0^t\,\mathbf{V}_0\,, \tag{64}$$

reduces from $6\pi\eta a$ for a no-slip sphere ($\ell^* = 0$) to $4\pi\eta a$ for a perfect-slip sphere with stress-free surface ($\ell^* = \infty$). For a perfect-slip sphere such as a gas bubble with clean surface without adsorbed contaminants, the drag force is entirely due to the pressure changes in the fluid without viscous stress contributions. Since $c_3 = 0$ for $\ell^* = \infty$, the flow exterior to a translating gas bubble is that of a Stokeslet of strength $\mathbf{F} = 4\pi\eta a\mathbf{V}_0$ placed in its center. The relation $F^h = Ca\eta V_0$ with undetermined constant C follows readily from linearity of the Stokes equations and BCs, and a dimensional analysis using the sphere radius as the only physical length scale. The difficult part is the determination of C which as we have shown requires an elaborate calculation.

The tangentially oriented slip velocity, $\mathbf{u}'_{\rm slip}(\theta) = u'_\theta(a,\theta)\mathbf{e}_\theta$, relative to the sphere surface is

$$\mathbf{u}'_{\rm slip}(\theta) = \frac{1}{2}\left(\frac{3\ell^*}{1+3\ell^*}\right) V_0 \sin\theta\, \mathbf{e}_\theta = -\frac{1}{2}\left(\frac{3\ell^*}{1+3\ell^*}\right)[\mathbf{1}-\hat{\mathbf{r}}\hat{\mathbf{r}}]\cdot\mathbf{V}_0\,. \qquad (65)$$

It is zero at the poles, where $\theta = \{0,\pi\}$ and $\hat{\mathbf{r}} = \pm\mathbf{e}$, and maximal in magnitude on the equator, where $\theta = \pi/2$ and $\hat{\mathbf{r}} \perp \mathbf{e}$. On the equator, the slip velocity points oppositely to $\mathbf{V}_0$ since $\mathbf{e}_\theta(\theta = \pi/2) = -\mathbf{e}$. For perfect slip, the result $\mathbf{u}_{\rm slip} = -\mathbf{V}_0/2$ is obtained at the sphere equator.

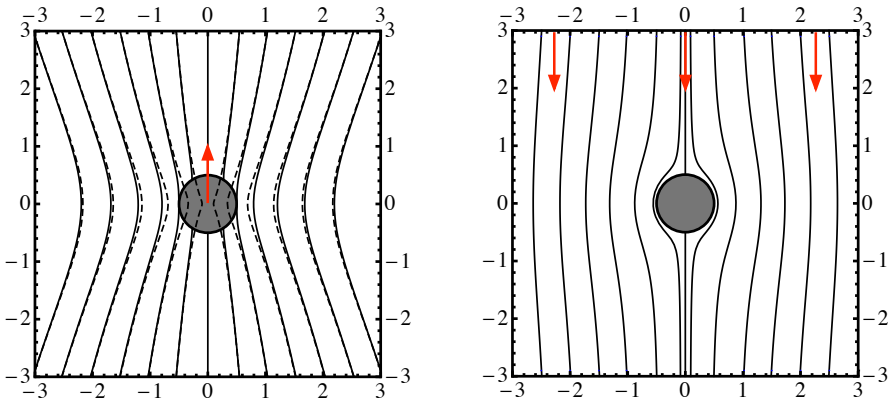

Fig. 9 Left: Comparison of flow streamlines generated by an upward point force centred at the origin (a Stokeslet), marked by dashed lines, and a spherical no-slip particle (solid lines) moving upwards with velocity $\mathbf{V}_0$ (red arrow) as viewed in the laboratory frame. Right: The streamlines circle around the sphere if viewed in its rest frame, owing to its experiencing of a uniform ambient flow equal to $-\mathbf{V}_0$. Note the fore-aft symmetry of the flow field related to the kinematic reversibility of Stokes flows. Reproduced from the COMPLOIDS book [9] with kind permission of the Societa Italiana di Fisica.

We proceed by discussing the lab frame velocity field of a translating no-slip microsphere, given in dyadic notation by

$$\mathbf{u}(\mathbf{r}) = \left[\left(\frac{a}{r}\right)(\mathbf{1}+\hat{\mathbf{r}}\hat{\mathbf{r}}) - \frac{1}{3}\left(\frac{a}{r}\right)^3(3\hat{\mathbf{r}}\hat{\mathbf{r}}-\mathbf{1})\right]\cdot\frac{\mathbf{F}}{8\pi\eta a}, \tag{66}$$

with $\mathbf{F} = 6\pi\eta a\mathbf{V}_0$, and with r measuring the distance from the center of the sphere. This result has been first calculated by Stokes more than 150 years ago [47], in a way different from the one described above. The velocity field in Eq. (66) has two interesting features: Firstly, far away from the particle it reduces to a Stokeslet flow field. The far-distance form is also recovered from taking the limit $a \to 0$ with the applied force kept constant. Secondly, the shorter-ranged source doublet potential flow contribution accounting for non-zero sphere volume is of importance in the near-distance region of the sphere only. The streamlines for a no-slip sphere and for an equal-force Stokeslet are drawn in Fig. 9. They are shown both in the lab frame where the sphere is moving and the fluid is quiescent, meaning that $\mathbf{u} \to \mathbf{0}$ for $r \to \infty$ (left part), and in the rest frame of the sphere where $\mathbf{u} \to -\mathbf{V}_0$ for $r \to \infty$ (right part). The vorticity field $\nabla \times \mathbf{u}$ around a translating sphere describing the local rotation of fluid elements is due to the Stokeslet part only, since the potential part has no vorticity. It is given by Eq. (37) restricted to the exterior of the sphere. Differently from $\mathbf{u}$, the associated vorticity field is invariant under a Galilean change of the reference frame.

4.5 Phoretic particle motion

So far we have dealt with the translational motion of an isolated microsphere and a rod settling subjected to an external body force such as the buoyancy-corrected gravitational force. The $\mathscr{O}(1/r)$ far-distance decay of the velocity field outside the moving particle is due to the momentum imparted to the fluid by the applied force.

Another mechanism for creating motion of a suspended microparticle is due to an imposed field gradient, such as an electric field $\mathbf{E}_\infty = -\nabla\phi_\infty$, a temperature gradient ∇T, or a concentration gradient, ∇c, in the concentration field c of small solutes surrounding the colloidal particle. Depending on the physical field, one refers to electrophoresis, thermophoresis or diffusiophoresis, respectively. The field gradients drive a so-called phoretic fluid flow relative to the particle surface in an interfacial region surrounding the particle. The effective hydrodynamic slip associated with the relative motion of the particle and the surface-phoretic flow results in a non-zero phoretic velocity, $\mathbf{V}_{\text{phor}}$, of the particle in the lab frame where the fluid velocity is zero at infinity (quiescent fluid). The phoretic particle motion occurs even though the total direct force and torque on the particle plus its interfacial layer are zero, i.e.

$$\mathbf{F}_T = \mathbf{0}, \quad \mathbf{T}_T = \mathbf{0}, \tag{67}$$

with the balancing hydrodynamic drag force and torque being likewise equal zero. There is no Stokeslet involved in the velocity field exterior to the particle and its boundary layer, referred to as the outer flow region. The velocity field in the outer region decays thus asymptotically like $\mathscr{O}(r^{-2})$ or faster, with r measuring the radial

distance to the sphere center. As we are going to show in the context of the electrophoresis of a charged colloidal sphere, the outer velocity field is actually a source doublet potential flow with the characteristic $\mathscr{O}(r^{-3})$ far-distant decay. A classical review of phoretic motions is given in [48]. For recent lecture notes on electrophoresis, and the dynamics of charge-stabilized suspensions in general, see [10] .

Consider now an insulating, charged colloidal sphere of radius a immersed in an infinite electrolyte solution. For the matter of definiteness, the sphere is assumed to carry a uniform negative surface charge (see Fig. 10).

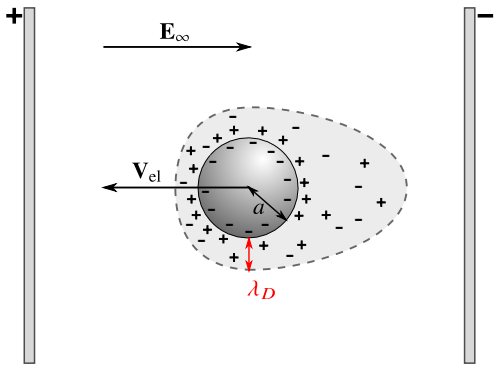

Fig. 10 Electrophoretic migration, with velocity $\mathbf{V}_{\rm el}$, of a negatively charged colloidal sphere in a uniform electric field of strength $\mathbf{E}_\infty$. The oppositely charged interfacial layer of electrolyte ions with extension $\sim \lambda_{\rm D}$ is slightly distorted (polarized) from the spherical shape at zero external field. The counterions in the near-surface interfacial region drive an electro-osmotic flow. Figure redrawn after [49].

In thermal equilibrium without an externally applied electric field, the charged sphere is surrounded by a diffuse spherical layer of mainly oppositely charged electrolyte counterions which screen its electric effect to the outside fluid region. On the length scale of the colloidal sphere, this interfacial region can be considered as an oppositely (here: positively) charged fluid of charge charge density $\rho_{\rm el}(r)$. This density decays exponentially with outgoing radial distance from the sphere surface at $r = a$. The outer electrolyte fluid in the region $r > a + \lambda_{\rm D}$ is practically electroneutral, since the influence of the surface charge is screened out across the interface. Here, $\lambda_{\rm D}$ is the Debye screening length characterizing the thickness of the charged interfacial layer. It describes the, at least for larger distances, exponential radial decay of the interfacial charge density

$$\rho_{\rm el}(r > a) \propto \exp\{-r/\lambda_{\rm D}\}\,. \tag{68}$$

The charged sphere and its neutralizing interfacial fluid region form an electric double layer (EDL) sphere of radius $a + \lambda_{\rm D}$ whose net charge content is zero. The total electric force and torque on the EDL sphere are consequently zero. The thickness, $\lambda_{\rm D}$, of the interfacial region decreases with increasing concentration of electrolyte ions. This can be triggered experimentally by the addition of salt, or through osmotic contact with an electrolyte reservoir (buffer). For an aqueous strong 1-1 electrolyte at 25 °C, the Debye length in nanometres is

$$\lambda_{\mathrm{D}} = \frac{0.304}{\sqrt{n_s[M]}}\,, \tag{69}$$

where $n_s[M]$ is the concentration of salt ion pairs in mol per litre. For a 1 M solution is $\lambda_{\mathrm{D}} = 0.3$ nm. An upper bound is set by the self-dissociation of water requiring that $\lambda_{\mathrm{D}} < 961$ nm.

If exposed to an uniform electric field, $\mathbf{E}_\infty = E_\infty \mathbf{e}$, created by distant sources such as a pair of electrode plates with an applied voltage, the negatively charged sphere migrates with constant electrophoretic velocity

$$\mathbf{V}_{\mathrm{el}} = \mu_{\mathrm{el}} \mathbf{E}_\infty\,, \tag{70}$$

opposite to the direction of the applied electric field. The field-independent electrophoretic mobility, μ_{el},, characterizing the phoretic particle motion, has a negative sign for a negatively charged particle. The electrophoretic drift velocity $\mathbf{V}_{\mathrm{el}}$ is determined by two retarding electrokinetic effects, termed the electro-osmotic flow and the ion cloud polarization effect, respectively. Both effects lower the magnitude of the electrophoretic velocity below the limiting value, $V_{\mathrm{el}}^0 = |QE_\infty|/(6\pi\eta a)$, for a sphere of surface charge Q without an electrolyte boundary layer, which is determined by the balance of the electric and hydrodynamic friction forces on the sphere. This limiting velocity is reached by a charge-stabilized colloidal sphere with an ultra-extended, and therefore ultra-dilute, diffuse layer where $\lambda_{\mathrm{D}} \gg a$.

The osmotic flow effect represents the hydrodynamic drag exerted on the sphere surface by the counter-flowing (since oppositely charged) fluid forming the diffuse layer. The electro-osmotic counterflow is driven by the electric body force density,

$$\mathbf{f}(\mathbf{r}) = \rho_{\mathrm{el}}(\mathbf{r})\mathbf{E}(\mathbf{r}). \tag{71}$$

in the inhomogeneous Stokes Eqs. (5). Here, $\mathbf{E}(\mathbf{r})$ is the local electric field inside the diffuse layer which in general differs from the externally applied field.

The charge polarization effect, on the other hand, describes the field-induced slight distortion of the interfacial EDL zone from its spherically symmetric equilibrium shape at zero field. This distortion or polarization sets up diffusion currents of electrolyte ions which tend to equilibrate the EDL system back to spherical symmetry, with the net effect of slowing the sphere motion. The polarization effect becomes stronger with increasing particle charge and electric surface potential, and with decreasing mobilities of the electrolyte ions.

We restrict ourselves in the following to a charged colloidal sphere with an ultrathin interfacial layer for which $\lambda_{\mathrm{D}} \ll a$. We further assume a weak surface charge density. The electrophoresis problem in this limiting situation was first treated in some detail by Smoluchowski (1903). It is therefore referred to as the Smoluchowski limit. Since the diffuse interfacial region reduces now to a thin boundary layer coating the sphere, the fluid can be mentally divided into an extended outer region $r > a + \lambda_{\mathrm{D}}$ where $\rho_{\mathrm{el}} = 0$, and in a thin boundary layer region $a \le r < a + \lambda_{\mathrm{D}}$ which is locally flat. The flows in the two regions are first determined independently and afterwards matched (asymptotically) to fix the remaining integration

constants. We just outline here the major steps of this calculation. For details see, e.g., [10, 50]. For the assumed low surface charge density, $\rho_{\rm el}$ remains radially symmetric (i.e., unpolarized) in the presence of the external field. The sphere plus its boundary layer have the appearance in the outside fluid region of a neutral, non-conducting sphere of radius $a+\lambda_{\rm D}$ (the EDL sphere). This gives rise to a dipolar electric field, $\mathbf{E}_{\rm out}(\mathbf{r})$, in the outer region whose field lines must bend tangentially near the sphere surface, for otherwise there would be an electric current perpendicular to the non-conducting sphere surface. The surface-tangential electric field acts on the charged fluid inside the boundary layer through the body force term in Eq. (5), creating a surface-tangential flow profile as depicted in Fig. (11) which sketches the locally flat interfacial region. While the fluid sticks to the actual sphere surface

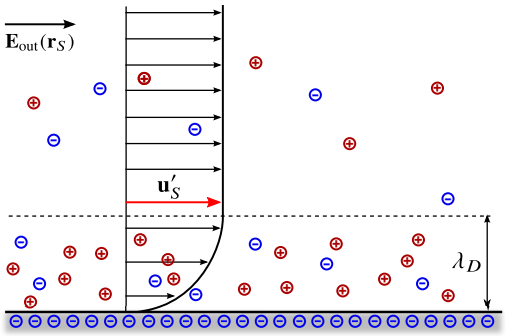

Fig. 11 Electro-osmotic flow profile of an electrolyte solution flowing tangentially past the locally flat surface of a negatively charged microsphere, viewed in its rest frame. The flow outside the thin boundary layer of thickness $\lambda_{\rm D}$ is plug-like with slip velocity $\mathbf{u}'_s(\mathbf{r}_s)=-\mu_{\rm el}\mathbf{E}_{\rm out}(\mathbf{r}_s)$. Redrawn after [9].

S_a (i.e., the no-slip surface BC is used here), outside the enclosing surface $S_{a+\lambda_{\rm D}}$ of the EDL sphere a plug-like local flow is observed, reminiscent of perfect slip. Incidentally, this plug-like electro-osmotic flow outside the Debye layer region is used in microfluidic devices to drive ion-containing aqueous media through narrow micro-channels where the Stokes flow conditions apply. In micro-channels, electro-osmotic flow transport is far more efficient than using an imposed pressure gradient along the channel [49]. See Fig. 12 for the sketch of such a device.

The velocity field at the slip surface, in the rest frame of the sphere, is calculated as [48, 10]

$$\mathbf{u}'_s(\mathbf{r}_s)=-\frac{\varepsilon\zeta}{4\pi\eta}\mathbf{E}_{\rm out}(\mathbf{r}_s)=-\frac{3\varepsilon\zeta}{8\pi\eta}\,(\mathbf{1}-\hat{\mathbf{r}}\hat{\mathbf{r}})\cdot\mathbf{E}_\infty\,, \tag{72}$$

where $\mathbf{r}_s\in S_{a+\lambda_{\rm D}}$, and ε is the static dielectric constant of the fluid. Since $\lambda_{\rm D}\ll a$, we were allowed in the second equality to identify the slip surface $S_{a+\lambda_{\rm D}}$ with the actual particle surface S_a. The so-called zeta potential, ζ, is likewise identified with the electric potential at the actual sphere surface. The surface potential decays exponentially to zero in going outwards radially from a to $a+\lambda_{\rm D}$.

Since the outer fluid is uncharged, the outer velocity field in the lab frame is found from a purely hydrodynamic consideration, namely from the solution of the homogeneous Stokes equations with inner inner and outer BCs,

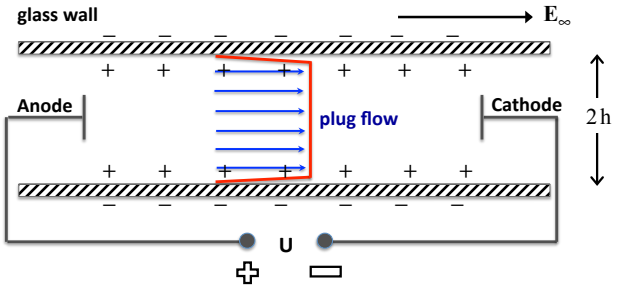

Fig. 12 Sketch of electro-osmotic plug flow in an open microcapillary tube with negatively charged glass walls. The non-dissipative plug flow is driven by the field-induced migration of counterions accumulated in the thin Debye interfacial layer of thickness $\lambda_D \ll 2h$ at the glass walls. In a tube closed at both ends, a pressure difference is created along the channel which drives a Poiseuille-type backflow of fluid in the central region of the tube [49].

$$\mathbf{u}_{\rm out}(\mathbf{r}_s) = \mathbf{V}_{\rm el} + \mathbf{u}'_s(\mathbf{r}_s)\,, \quad \mathbf{u}_{\rm out}(\mathbf{r}\to\infty) = \mathbf{0}\,. \tag{73}$$

respectively, where $\mathbf{r}_s \in S_{a+\lambda_D} \approx S_a$, and the sphere located momentarily at the coordinate frame origin. The electrophoretic velocity $\mathbf{V}_{\rm el}$ is still unknown to this point. The boundary value problem has a unique flow solution if one demands in addition the EDL sphere to be force- and torque free, in accord with its overall electroneutrallity.

To determine $\mathbf{u}_{\rm out}$ using the singularity method, we notice first that the Stokeslet and Rotlet are ruled out as flow contributions since they would result in a non-zero drag force and torque. Therefore, we use the ansatz,

$$\mathbf{u}_{\rm out}(\mathbf{r}) = c_3 a^3 \mathbf{D}_{\rm S}(\mathbf{r};\mathbf{e})\,. \tag{74}$$

for the out flow in the lab frame, with a source doublet in direction $\mathbf{e}$ of the applied electric field. With this ansatz, the inner and outer BCs are fulfilled with c_3 determined as $c_3 = \varepsilon\zeta E_\infty/(8\pi\eta)$, and the electrophoretic velocity as

$$\mathbf{V}_{\rm el} = \mu_{\rm el}\mathbf{E}_\infty\,, \quad \mu_{\rm el} = \frac{\varepsilon\zeta}{4\pi\eta}\,, \tag{75}$$

respectively. The so-called Smoluchowski electrophoretic mobility $\mu_{\rm el}$ scales linearly with the electric zeta potential, and it is independent of the particle radius. The outer velocity field in the lab frame is thus

$$\mathbf{u}_{\rm out}(\mathbf{r}) = \frac{1}{2}\left(\frac{a}{r}\right)^3 [3\hat{\mathbf{r}}\hat{\mathbf{r}} - \mathbf{1}]\cdot\mathbf{V}_{\rm el} = \mu_{\rm el}\mathbf{E}_{\rm out}(\mathbf{r}) + \mathbf{V}_{\rm el}\,. \tag{76}$$

In the second equality, we have expressed the velocity field in terms of the outer electric dipole field.

Being an incompressible potential flow field, $\mathbf{u}_{\rm out}$ fulfils $\Delta\mathbf{u}_{\rm out} = \mathbf{0}$ with $\nabla p_{\rm out} = 0$, so that the outer pressure field is uniform. The source doublet streamlines of the

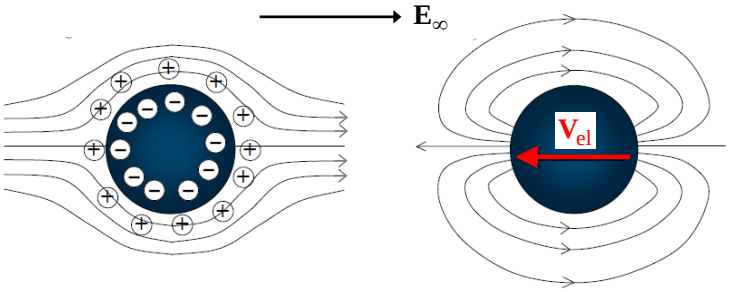

Fig. 13 Streamlines of the velocity field, $\mathbf{u}_{\text{out}}(\mathbf{r})$, outside the thin boundary layer of a negatively charged microsphere in electrophoretic motion. Left: Streamlines in the rest frame of the sphere for which $\mathbf{u}_{\text{out}}(\mathbf{r}\to\infty) = -\mathbf{V}_{\text{el}}$. Right: Streamlines in the lab frame where the fluid is at rest at infinity. The sphere migrates in the direction opposite to the external field $\mathbf{E}_\infty$.

outer velocity field are shown in the right part of Fig. 13. They diverge in front of the moving sphere and curve back at its rear side. There are no closed streamlines, which are not allowed for a potential flow where $\nabla\times\mathbf{u}=\mathbf{0}$. Since $\mathbf{u}_{\text{out}}$ decays asymptotically like $\mathscr{O}(r^{-3})$ there is indeed no hydrodynamic torque exerted on the EDL sphere. Moreover, the absence of a $\mathscr{O}(r^{-2})$ Stresslet contribution to $\mathbf{u}_{\text{out}}$ is consistent with the fact that a non-uniform ambient flow was not considered. The streamlines, shown in the left part of Fig. 13, are different if viewed in the particle rest frame where distant from the sphere the fluid moves with uniform velocity $-\mathbf{V}_{\text{el}}$.

Without requiring the outer flow solution, the electrophoretic velocity for a spherical colloidal particle can be obtained directly as the surface average of the slip velocity field in the particle rest frame. In fact, it follows from Eq. (72) that

$$\frac{1}{4\pi a^2}\int_{S_a} dS\,\mathbf{u}'_s(\mathbf{r}_s) = -\mathbf{V}_{\text{el}}\,. \tag{77}$$

This result implies that the surface average of the outer velocity field in the lab frame is zero. This should be contrasted with the lab-frame Stokeslet velocity field for $r\geq a$,

$$\mathbf{u}(\mathbf{r}) = \frac{1}{2}\left(\frac{a}{r}\right)[\mathbf{1}+\hat{\mathbf{r}}\hat{\mathbf{r}}]\cdot\mathbf{V}_0\,, \tag{78}$$

due to a Navier perfect-slip sphere translating with velocity $\mathbf{V}_0$, which was discussed earlier in relation to Eq. (65). On taking the surface average of this Stokeslet field, the non-zero result $\mathbf{V}_0/3$ is obtained. This highlights the difference between a phoretically moving sphere with an *effective* slip, and a forced perfect-slip sphere without the phoretic boundary layer. The electrophoretic mobility becomes different from the Smoluchowski result in Eq. (75), if in place of the no-slip BC at S_a the Navier partial-slip BC is used. The Smoluchowski mobility is then enhanced by the factor $(1+\ell/\lambda_{\text{D}})$, for the Navier slip length small compared to the sphere radius [51]. Measured slip lengths are typically of the order of nanometres.

For the general case of a phoretically moving microsphere, it can be shown that its drift velocity is given by the surface average [52, 53]

$$\mathbf{V}_{\text{phor}} = -\frac{1}{4\pi a^2}\int_{S_a} dS\,\mu_s(\mathbf{r}_s)\,[\mathbf{1}-\hat{\mathbf{r}}\hat{\mathbf{r}}]\cdot\nabla\phi(\mathbf{r}_s)\,, \tag{79}$$

where ϕ stands likewise for the potential of the applied electric field, temperature or solute concentration. Here, $\mu_s(\mathbf{r}_s)$ is a local surface mobility coefficient allowed to vary over the sphere surface. In our discussion of electrophoresis the potential gradient and mobility are taken as constant, with the latter equal to $(3/2)\mu_{\text{el}}$.

On recalling the steps which led to Eq. (75), one notices that owing to the local surface flatness on the scale of λ_{D}, the inner boundary value problem for the interfacial region is independent of the global shape of the microparticle. Therefore, the second equality in Eq. (76) remains valid for arbitrarily shaped, non-conducting rigid particles, provided the local radius of curvature at all surface points is large compared to λ_{D}. What varies with the particle shape is only the near-distance form of $\mathbf{E}_{\text{out}}(\mathbf{r})$. The latter is determined by the electrostatic boundary value problem of a non-conducting particle in an external field, with its field lines bending tangentially close to the particle surface to satisfy the non-conductance condition. The crucial point here is that the explicit form of $\mathbf{E}_{\text{out}}(\mathbf{r})$ is not required for the determination of the electrophoretic mobility. In fact, on noting $\mathbf{E}_{\text{out}} \to \mathbf{E}_\infty$ and $\mathbf{u}_{\text{out}} \to \mathbf{0}$ for $r \to \infty$, the Smoluchowski mobility result in Eq. (75) is readily recovered from the second equality in Eq. (76), but now for arbitrary particle shape and size, under the proviso that the particle has *uniform* surface zeta potential ζ. This remarkable result is supplemented by the likewise remarkable feature that the particle migrates phoretically without rotating. This follows from the fact that the far-distant form of $\mathbf{E}_{\text{out}}(\mathbf{r})$ is a dipolar electric field of $\mathscr{O}(r^{-3})$, independent of the particle shape. This in turn implies that $\mathbf{u}_{\text{out}}(\mathbf{r})$ is a potential flow field with a likewise $\mathscr{O}(r^{-3})$ far-distance decay. Such a flow exerts no hydrodynamic torque on the particle which consequently is non-rotating while translating.

However, the remarkable finding of shape-independent mobility has been obtained based on various restrictions. We quote here the most important ones: Firstly, the surface zeta potential is assumed to be weak enough for the polarization of the diffuse layer to be negligible, i.e. $|\zeta e|$ is small compared to $k_B T$, with e denoting the elementary charge. Secondly, the diffuse boundary layer must be very thin. Moreover, the applied electric field should be uniform on the scale of the particle size, and the small excluded volume of the electrolyte ions should not matter. The ions must be monovalent, and the dielectric constant and electrolyte viscosity should not change across the boundary layer. See [54] for a quantitative theory for the concentration dependence of the electrolyte viscosity.

For an isolated charge-stabilized sphere, surface uniformity of zeta potential and surface charge density go hand in hand. However, this is not the case for a non-spherical particle which has surface regions of varying curvature. A particle with uniform surface charge density has a larger zeta potential in the regions of higher curvature. This causes the particle to reorient while translating.

We proceed with the interesting generalization that a force $\mathbf{F} = F\mathbf{e}$ co-linear with the applied field is acting on the electrophoretically moving sphere. The sphere velocity $\mathbf{V} = V\mathbf{e}$ and the flow for this situation can be constructed by the addition of a Stokeslet field of strength $\mathbf{F}$ to the source doublet, i.e

$$\mathbf{u}(\mathbf{r}) = \left\{ \left(\frac{a}{r}\right)[\mathbf{1} - \hat{\mathbf{r}}\hat{\mathbf{r}}] \left(\frac{F}{8\pi\eta a}\right) + \frac{c_3}{2}\left(\frac{a}{r}\right)^3 [3\,\hat{\mathbf{r}}\hat{\mathbf{r}} - \mathbf{1}] \right\} \cdot \mathbf{e}\,. \tag{80}$$

The two conditions determining c_3 and the sphere velocity are

$$\begin{aligned} \mathbf{u}(\pm a\mathbf{e}) &= \mathbf{V} \\ \mathbf{u}(a\hat{\mathbf{r}}) - \mathbf{V} &= -\frac{3}{2}\,(\mathbf{1} - \hat{\mathbf{r}}\hat{\mathbf{r}}) \cdot \mathbf{V}_{\mathrm{el}}\,. \end{aligned} \tag{81}$$

The first condition assures that the fluid velocity at the poles of the sphere agrees with its velocity. The second condition demands the phoretic surface flow in the rest frame of the sphere to be the same as in unforced electrophoresis. This is a reasonable requirement since for negligible EDL polarization the local osmotic flow in the boundary layer does not depend on whether the sphere is forced or not. To evaluate the second condition, one selects a unit vector $\hat{\mathbf{r}} = \mathbf{e}_\perp$ perpendicular to $\mathbf{e}$. The results is

$$\begin{aligned} V &= V_{\mathrm{el}} + \frac{F}{6\pi\eta a} = \mu_0^t F + \mu_{\mathrm{el}} E_\infty \\ c_3 &= V_{\mathrm{el}} - \frac{F}{12\pi\eta a}\,. \end{aligned} \tag{82}$$

The first equation expresses the expected linear superposition of the particle velocities of the two problems of a phoretically moving sphere without body force, and a forced no-slip sphere without phoresis. It can be likewise formulated as a mobility problem for given forces F and eE_∞. The second force contribution, however, is not a body force.

The sphere becomes stationary, with $V = 0$, when the body force is equal to

$$F = -(6\pi\eta a)V_{\mathrm{el}}\,, \tag{83}$$

i.e. equal to the hydrodynamic drag force on a no-slip and non-phoretic sphere moving with velocity V_{el}. Stationarity can be achieved experimentally, up to the inevitable undirected Brownian motion for smaller particles, using optical tweezers. The flow field of a stationary phoretic sphere is thus

$$\mathbf{u}(\mathbf{r}) = -\frac{3}{4}\left\{ \left(\frac{a}{r}\right)[\mathbf{1} - \hat{\mathbf{r}}\hat{\mathbf{r}}] - \left(\frac{a}{r}\right)^3 [3\,\hat{\mathbf{r}}\hat{\mathbf{r}} - \mathbf{1}] \right\} \cdot \mu_{\mathrm{el}}\mathbf{E}_\infty\,. \tag{84}$$

The surface average of this velocity field yields $\mu_{\mathrm{el}}\mathbf{E}_\infty$, which expresses again the body-force independence of the surface osmotic flow.

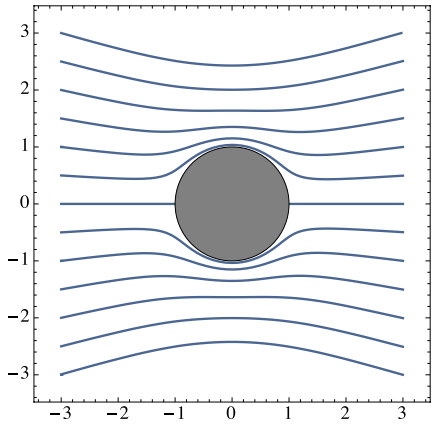

Fig. 14 Streamlines around an electrophoretically driven negatively charged sphere in quiescent fluid, held stationary by an applied body force according to Eq. (83). The flow is maintained by the electro-osmotic counterions current in the boundary layer region near the sphere surface.

The flow in Eq. (84) describes an interesting situation: Even though the sphere is held stationary in a quiescent fluid, it maintains a non-zero flow driven by the osmotic current along its surface. For a negatively charged sphere where $\mu_{\rm el}$ is negative, the flow is oriented in direction of the external electric field. The flow lines of the stationary sphere are shown in Fig. 14. At large distances from the sphere, the Stokeslet term dominates and the streamlines converge in the rear and diverge in front. If the sphere is placed close to an interface, using optical tweezers, a sufficiently strong temperature gradient, gravity, or electric wall attraction, the streamlines facing the wall will bent along the interface. This sets up an attractive hydrodynamic force which favors the formation of particle clusters at the interface [55].

4.6 Many-particle hydrodynamic interactions

As explained in Subsec. 4.1, when a colloidal particle moves in a viscous liquid in the presence of other particles, it creates a flow pattern which affects not only the motion of neighbouring particles, but through hydrodynamic back reflection also the motion of the particle itself, and this even in the (hypothetical) absence of direct interactions between the particles. The velocity field generated by a moving particle is quasi-instantaneously transmitted through the fluid, inducing forces and torques on all the other particles. These solvent-mediated interactions are referred to as hydrodynamic interactions (HIs) [1]. For a quiescent dispersion of N microparticles, these interactions are characterized by the $6N\times 6N$ mobility matrix, $\boldsymbol{\mu}(\mathbf{X})$, in Eq. (23), or likewise by the associated $6N\times 6N$ friction matrix, $\boldsymbol{\zeta}(\mathbf{X})$, which both linearly relate translational and angular particles velocities with drag forces and torques. There are three major distinguishing features of HIs which render them difficult to deal with. Firstly, they are long-ranged, i.e. the long-distance decay of the velocity field due to a moving particle decays for forced motion with the distance r as $1/r$. Secondly, they are of genuinely many-body character, meaning that the HIs between

a pair of particles are changed through the presence of a third one in their vicinity. To account for the non-additivity requires the consideration of multiple flow reflections by neighbouring microparticles, with the reflections being responsible for the deviations of the exact HIs from the approximate form in terms of a superposition of pair contributions. The approximate pairwise additivity treatment of the HIs where flow reflections are disregarded altogether can be justified for dilute dispersions only, for conditions where all particles are mutually well separated on the scale of their sizes. Non-pairwise additive higher-order HIs effects are important in particular in the dynamics of concentrated dispersions. The third distinguishing feature of the HIs is that, differently from direct interactions, they do not affect the equilibrium microstructure (i.e., the configurational distribution function $P_{\rm eq}(\mathbf{X})$), in dispersions without external fields or imposed macroscopic flows. This is reflected by the fact that owing to their interrelation with hydrodynamic friction forces, HIs are not derivable from a many-particle conservative potential energy function determining the equilibrium distribution function.

Since diffusion transport properties of suspensions are expressible as configurational averages of certain tensor elements of $\boldsymbol{\mu}(\mathbf{X})$, and since $\boldsymbol{\mu}(\mathbf{X})$ is a key ingredient in the many-particle Smoluchowski and Stokes-Liouville equations governing the evolution of the configurational distribution function $P(\mathbf{X},t)$ of Brownian and non-Brownian microparticles, respectively, it is essential to be able to calculate this matrix for a many-particle system. Over the years, various numerical methods have been developed for this purpose, and a number of review articles [29, 37] and books [1, 14, 21] dealing with HIs are available.

If the microparticles are mutually well separated, with relative distances large compared to their size, the flow induced by their motion can be regarded approximately as originating from point forces concentrated at their centres. This liberates one from the severe complications of having to invoke the prescribed hydrodynamic BCs simultaneously on the particle surfaces. The tensorial mobility coefficients describing the linear relations between applied forces and resulting velocities are then straightforwardly approximated by the superposition of Stokeslets at the particle centres according to (point-particles model)

$$\boldsymbol{\mu}_{ii}^{tt} \approx \mu_0^t \mathbf{1}, \tag{85}$$

$$\boldsymbol{\mu}_{ij}^{tt} \approx \mathbf{T}(\mathbf{R}_i - \mathbf{R}_j) \tag{86}$$

for $i \neq j$. Here, μ_{0i}^t is the single-particle translational mobility coefficient of particle i, and $\mathbf{1}$ is the unit tensor. Only the leading-order long-distance behaviour of the flow field is included in the point-particles model, with the off-diagonal mobility tensors decaying as r^{-1} in the inter-particle distance r. While the pairwise additive point-particles model is applicable to well-separated particles, it usually fails when particles are close to each other or to a confining wall, as indicated by the possible violation of the positive definiteness of the mobility matrix approximation in Eq. (85). At large concentrations and for smaller inter-particle distances, more refined theoretical methods and numerical schemes are required to account for the near-distance and non pairwise additive contributions to the HIs.

The next important step in going beyond the point-particles model is to account for the non-zero volumes of the particles while still maintaining the pairwise additive single-particle flow superposition. For spherical no-slip particles this is referred to as the Rotne-Prager (RP) mobility matrix approximation [56], and with an appropriate extension to overlapping no-slip spheres also as the Rotne-Prager-Yamakawa (RPY) approximation [57, 58]. The RP approximation is still pairwise additive, with the RP mobility tensors exhibiting a long-distance decay of $\mathscr{O}(r^{-3})$. All the hydrodynamic back reflections, which give rise to more steeply decaying flow field contributions of $\mathscr{O}(r^{-4})$, are hereby disregarded. The main merit of the RP approximation, in addition to its convenient simplicity, is that is leads to a translational mobility matrix approximation, $\boldsymbol{\mu}^{tt,RP}$, which is positive definite for all physically allowed configurations of non-overlapping spheres. Moreover, $\boldsymbol{\mu}^{tt,RP}$ is an upper bound to the exact translational mobility matrix, $\boldsymbol{\mu}^{tt}$, in the sense that $\mathbf{b}\cdot\left(\boldsymbol{\mu}^{tt,RP}-\boldsymbol{\mu}^{tt}\right)\cdot\mathbf{b}>0$ for all non-zero $3N$-dimensional vectors $\mathbf{b}$ and all allowed configurations. This property of the RP approximation can be used for constructing upper bounds to certain transport properties of concentrated dispersion such as the (short-time) mean sedimentation velocity. The RP approximation can be profitably used for dilute to moderately concentrated dispersions of no-slip microspheres which strongly repel each other over larger distances. Examples in case are like-charged colloidal particles, and lower-salinity aqueous solutions of globular proteins.

The derivation of the translational mobility matrix in RP approximation proceeds as follows: Consider first an isolated no-slip microsphere j of radius a in an infinite quiescent fluid, translating without rotation under the action of the force $\mathbf{F}_j$ acting at its centre at $\mathbf{R}_j$. From Eq. (38), one notices that $\boldsymbol{\sigma}\cdot\mathbf{n}=\mathbf{F}_j/(4\pi a^2)$ is consistent with the no-slip BC on the sphere surface, i.e. the surface shear stress in this special situation is constant. Consequently,

$$\mathbf{u}_j^{(0)}(\mathbf{r})=\int dS'\,\mathbf{T}(\mathbf{r}-\mathbf{r}')\cdot\frac{\mathbf{F}_j}{4\pi a^2}=\left(1+\frac{a^2}{6}\nabla^2\right)\mathbf{T}(\mathbf{r}-\mathbf{R}_j)\cdot\mathbf{F}_j \tag{87}$$

where for the second equality, the mean-value theorem for bi-harmonic functions has been used [59], on recalling that $\nabla^2\nabla^2\mathbf{T}(\mathbf{r})=\mathbf{0}$ for all non-zero vectors $\mathbf{r}$. From performing the second-order differentiation, one verifies that $\mathbf{u}_j^{(0)}(\mathbf{r})$ is equal to the velocity field in Eq. (66) which we had obtained earlier using the singularity flow solutions.

Consider next the incident flow, $\mathbf{u}_{\rm inc}^{(N-1)}(\mathbf{r})$, created by the motion of $(N-1)$ no-slip spheres at the position $\mathbf{R}_i$ of another sphere i. It should be noticed here that $\mathbf{u}_{\rm inc}^{(N-1)}(\mathbf{r})$ is determined by the BCs on all N spheres, including the singled-out sphere i. In the RP treatment, the incident flow is crudely approximated by the superposition of the single-sphere flow fields,

$$\mathbf{u}_{\rm inc}^{(N-1)}(\mathbf{r})\approx\sum_{j\neq i}^{N}\mathbf{u}_j^{(0)}(\mathbf{r})\,. \tag{88}$$

In this incident flow field approximation, the $(N-1)$ no-slip BCs are only approximately fulfilled for configurations of mutually well separated spheres.

The velocity, $\mathbf{V}_i$, of a no-slip microsphere i of radius a in an infinite fluid, subjected a force $\mathbf{F}_i$ and an incident flow field $\mathbf{u}_{\rm inc}(\mathbf{r})$, is given by the exact translational Faxén law

$$\mathbf{V}_i = \mu_0^t \mathbf{F}_i + \left(1 + \frac{a^2}{6}\nabla_i^2\right)\mathbf{u}_{\rm inc}(\mathbf{R}_i)\,, \tag{89}$$

where μ_0^t is the translational single-particle mobility of a no-slip sphere. The only restriction on the form of the incident flow is that it has to be a Stokes flow solution, created by sources located outside the volume of sphere i. These sources could be, e.g., other microparticles or confining walls, whereby the wall influence can be described by an image system as discussed in the following section. A derivation of the present Faxén theorem is given, e.g., in [14, 35]. According to the Faxén theorem, freely advected, i.e. force- and torque-free, small particles can be used to trace out the streamlines caused by the motion of big ones. For an example, consider a small tracer sphere i placed in the (incident) flow of, say, a phoretically moving big sphere. Since on the small length scale a of the tracer the curvature contribution in Eq. (89) described by the Laplacian can be neglected, one has

$$\mathbf{V}_i \approx \mathbf{u}_{\rm inc}(\mathbf{r} = \mathbf{R}_i) \tag{90}$$

for the velocity of the tracer dragged along in the flow field of the big particle. Small tracer tracer particles have been used experimentally, e.g., to visualize the thermophoretic quasi-slip flow around a big polystyrene or silica sphere near a surface, driven by a temperature gradient in the fluid oriented perpendicular to the surface [60].

We use now the Faxén theorem to obtain the velocity of a no-slip sphere i of radius a in the incident flow of $(N-1)$ other ones of equal radii, using the single-spheres flow superposition. The result is

$$\mathbf{V}_i \approx \mu_0^t \mathbf{F}_i + \sum_{j\neq i}^{N}\left(1 + \frac{a^2}{3}\nabla_i^2\right)\mathbf{T}(\mathbf{R}_i - \mathbf{R}_j)\cdot\mathbf{F}_j\,, \tag{91}$$

where $\nabla_i^2\nabla_j^2\,\mathbf{T}(\mathbf{R}_i - \mathbf{R}_j) = \mathbf{0}$ for $i \neq j$ has been used in the derivation. The translational mobilities in the RP approximation follow readily from this result as

$$\boldsymbol{\mu}_{ii}^{tt,RP} = \mu_0^t \mathbf{1} \tag{92}$$

$$\boldsymbol{\mu}_{ij}^{tt,RP} = \mu_0^t\left[\frac{3}{4}\left(\frac{a}{r}\right)(\mathbf{1} + \hat{\mathbf{r}}\hat{\mathbf{r}}) + \frac{1}{2}\left(\frac{a}{r}\right)^3(\mathbf{1} - 3\hat{\mathbf{r}}\hat{\mathbf{r}})\right] \tag{93}$$

with $\mathbf{r} = \mathbf{R}_i - \mathbf{R}_j$. The positive definiteness of the RP translational mobility matrix can be shown, e.g., using the double surface integral representation of its tensor elements,

$$\boldsymbol{\mu}_{ij}^{tt,RP} = \frac{1}{(4\pi a^2)^2} \int_{S_i} dS \int_{S_j} dS' \, \mathbf{T}(\mathbf{r} - \mathbf{r}') \,, \tag{94}$$

which is valid also for $i = j$. It has been assumed for the validity of this representation for $i \neq j$ that the two spheres do not overlap. For the details on how positive definiteness is shown using this representation we refer to [58].

The simplicity of the RP approximation renders it very attractive for practical applications. It has been generalized to no-slip spheres of different radii (see, e.g., [58]), and to overlapping particles configurations [61]. Moreover, the RP approximation has been employed for the calculation of the mobilities of complex-shaped particles using bead-modelling of the particles [62].

For problems where particles are close to each other, like in concentrated dispersions, more precise methods than the simple RP approximation are required. Various advanced numerical methods have been developed for this purpose. A very powerful and versatile method is the force multipoles method advanced by Cichocki and coworkers. It is based on a multipolar expansion of the flow field for a system of spherical particles which is used to construct a set of equations determining the a priori unknown stresses at the sphere surfaces. The addition of lubrication corrections for nearly-touching particles has led to an efficient numerical algorithm allowing for a controlled high-precision calculation of the many-spheres mobility matrix [37]. A review of this method is given in [38]. The force multipoles method has been extended to account for HIs with a planar wall [63], two parallel walls [64], and a cylindrical channel [65]. A particularly intriguing feature of the method is its facile adaptability to different hydrodynamic BCs such as the Navier partial-slip and liquid interface BCs, with has opened the possibility to study the dynamics of permeable particles, droplets, and surfactant-covered particles.

4.7 Lubrication effects

Hydrodynamic lubrication plays an important role when two or more particles are brought close to each other. This is sketched in Fig. 15 for two no-slip smooth spheres, and for three types of relative translational motions, namely squeezing and receding motions along the line of centres, and shearing motion.

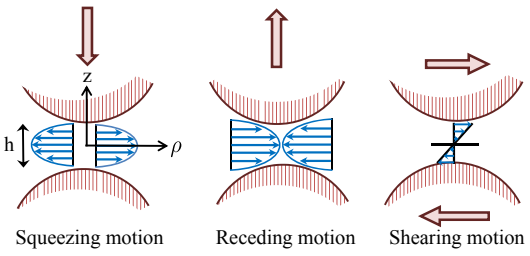

Fig. 15 A sketch of the flows in the thin gap region between two smooth spheres near contact, for relative translational motions as indicated.

Since the gap between the particles is small, large pressure gradient builds up in the gap region in order to squeeze out (or push in) the fluid in the form of an in-to-out Poiseuille flow in the gap area, as illustrated in Fig. 15. This leads to strong friction forces slowing down the motion of close particles and thus has the effect of strongly slowing the relative motion of nearly touching particles. As an example consider the squeezing motion of two no-slip spheres of radii a_1 and a_2, respectively (with sphere 1 on top) approaching each other with constant relative velocity V_{rel}. The lubrication flow analysis leads to the following expression [66]

$$p(\rho) - p_\infty \approx -\frac{3\eta a_1 a_2}{(a_1+a_2)h^2}\left[1+\left(\frac{a_1+a_2}{2a_1a_2h}\right)\rho^2\right]^{-2} V_{rel}\,, \tag{95}$$

for the pressure distribution inside the narrow gap with minimal surface-to-surface distance $h \ll \{a_1, a_2\}$. Here, $\rho \ll \sqrt{ah}$ is the lateral distance from the symmetry axis, and p_∞ is the inconsequential pressure far away from the gap region. The strong $\mathscr{O}(1/h^2)$ divergence of the pressure in the gap along the symmetry axis dominates the less severe $\mathscr{O}(1/h)$ divergence of the viscous contribution, $\sim \eta|\nabla \mathbf{u}|$, to the stress tensor. Thus only the pressure contribution is required in calculating the hydrodynamic drag force, $\mathbf{F}^h$, on the upper sphere 1 on the basis of Eq. (96). The result is [8, 21, 67]

$$\mathbf{F}^h \approx -\frac{6\pi\eta V_{rel}}{h}\left(\frac{a_1 a_2}{a_1+a_2}\right)^2 \mathbf{e}_z\,, \tag{96}$$

for the dominant near-contact lubrication part of the drag force which diverges like $\mathscr{O}(1/h)$. The main effect of lubrication is therefore a dramatic increase of hydrodynamic friction between closely spaced no-slip rigid surfaces. This effect can lead in concentrated suspensions to the formation of transient hydrodynamic clusters of particles with consequential shear thickening which has applications, e.g., in manufacturing of protective clothing.

The singular pressure concentration in the gap region of two no-slip spheres is less severe for shearing motion where it gives rise to weaker logarithmic singularity of the drag force at contact. Due to their mobile surfaces, two spherical drops slip past each other in shearing motion even when in contact, experiencing therefore non-divergent drag forces. For squeezing motion, however, there is still a $\mathscr{O}(1/\sqrt{h})$ singularity for two droplets with fully mobile interfaces. It is assumed here that the droplet interfacial tension is so large that flow-induced deviations from the spherical shape are negligible. For more information about lubrication effects under different surface BCs see [14, 66].

As an illustration of the dynamic effect of lubrication consider a no-slip sphere of radius a approaching a stationary, horizontal no-slip wall in squeezing motion (see Fig. 16). The sphere is driven by the *constant* external force $\mathbf{F} = -|F|\mathbf{e}_z = -\mathbf{F}^h$. This is a limiting case of Eq. (96), for $a = a_1$ and $a_2 \to \infty$ with the lower sphere 2 expanded into a planar wall. Here, h denotes now the distance from the wall to the closest surface point of the sphere. It follows that

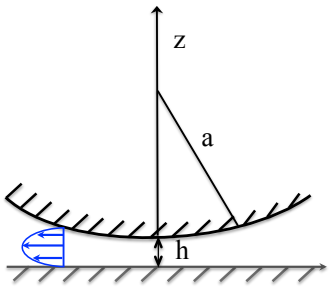

Fig. 16 Squeezing motion of a no-slip sphere towards a near-contact planar wall, driven by the constant force $\mathbf{F} = -|F|\mathbf{e}_z$.

$$\frac{dh(t)}{dt} = V_{rel}(t) \approx -\frac{\mu_0^t |F|}{a} h(t)\,, \tag{97}$$

with solution

$$h(t) \approx h_0 \exp\left\{ -\left(\frac{\mu_0^t |F|}{a} \right) t \right\}. \tag{98}$$

Here, h_0 is the near-contact starting distance with $h_0/a \sim 0.01$, and μ_0^t is the single-sphere translational mobility defined in Eq. (25). The exponentially slow vertical approach of the sphere to the wall is a good description in reality only until the gap distance h becomes comparable to the surface roughness of the sphere and plane which in fact leads to plane-sphere contact after a finite time. A finite contact time would be reached also due to the van der Waals attraction force between the planar wall and the sphere which in the distance range where lubrication applies scales as $\mathcal{O}(1/h^2)$ [68].

5 Single-particle dynamics near a flat interface

The preceding section was devoted to the effects of the solvent flow on the dynamics of suspended particulates in an unbounded fluid. Most realistic situations, however, involve the presence of a boundary that may considerably change the flow character, and by reflecting the flow incident upon it, may modify the hydrodynamic interactions between the particles. A pronounced example is the effect of sedimentation, where the backflow of fluid due to the presence of a container bottom, however far distant it may be, cannot be neglected in order to correctly determine the sedimentation velocity of dispersed microparticles [9]. Soft matter systems are very often bounded, especially in biophysical flows and in a number of technical applications. In this Section, we investigate the effects of the presence of an interface on the fluid flow, and in consequence on the suspended particles. We start by discussing a general solution for a point force in the presence of a boundary, and its dependence on the BCs at the interface. This allows to elucidate how the physical character of the interface may influence the flow close to it. We then consider in more detail the

motion of an isolated spherical particle close to a wall, with the BCs at the particle surface and lubrication effects taken into account. We discuss the commonly used approximations for the mobility of a microsphere near a no-slip wall, and present examples of experimental techniques capable of grasping the dynamic behaviour. Finally, we explore the motion of flexible particles and the effect of deformable boundaries, in situations where the elasticity of the surface or particles may not be neglected.

5.1 Point force near an interface

To demonstrate the effects of partial confinement on the hydrodynamics of a single particle, we will show explicit solutions for the velocity fields for a point force acting on a fluid bounded by a planar free surface, and a planar no-slip wall. These are limiting cases for a point-force near a planar liquid-liquid interface, in the limit that the viscosity ratio, $\lambda = \eta_1/\eta_2$, is reaching infinity and zero, respectively. The point force $\mathbf{F}$ is located at the point $\mathbf{r}_0 = (x_0, y_0, h)$ in the upper half space at vertical distance $h > 0$ above the $(x-y)$ interface at $z = 0$. Searched for is the flow field $\mathbf{u}(r)$ in the upper half space $z \geq 0$. We take advantage of the linearity of the Stokes equations to construct the flow field using the method of images. Akin to electrostatics [36], a number of hydrodynamic problems of higher symmetry can be solved by this elegant method. In this method, the fluid in the upper half-space of viscosity $\eta = \eta_1$ is mentally extended into the lower half-space, with the BCs imposed by the taken-out interface now accounted for in conjunction with the Stokeslet at $\mathbf{r}_0$ by an image system of elemental singularity solutions placed at appropriate positions in the lower half-space. The flow field constructed in this way is in the upper half-space identical to the original flow problem where the interface is present.

For a point force in front of a planar liquid-liquid interface, the image system multipoles are all located at the same image point

$$\mathbf{r}_0^* = \mathbf{P}_z \cdot \mathbf{r}_0 = (x_0, y_0, -h) \, . \tag{99}$$

Here

$$\mathbf{P}_z = \mathbf{1} - \mathbf{e}_z \mathbf{e}_z \tag{100}$$

is the $(x-y)$ plane reflection matrix. This matrix acting on an arbitrary vector turns the z-component of this vector into its negative.

Free surface: We explain the image method first for the simplest case of a Stokeslet above a free surface, e.g., a non-contaminated air-water interface or a Navier perfect-slip wall. The BCs for such an interface is that the surface flow has only an in-plane tangential component, and that there is no tangential stress across the interface. This is expressed by Eq. (17) in the limit that the viscosity, η_2, of the fluid in the lower half space vanishes, that is for $\lambda \to 0$. We shall assume the free surface not to deform

in response to the motion of the fluid. This is justified when the surface tension of the interface is large enough.

The image system is here simply the mirror Stokeslet of strength $\mathbf{F}^* = \mathbf{P}_z \cdot \mathbf{F}$ at the mirror location $\mathbf{r}_0^*$. The flow in the fluid occupying the upper half-space is thus

$$\mathbf{u}(\mathbf{r}) = \left[\mathbf{T}(\mathbf{R}) + \mathbf{T}(\mathbf{R}^*) \cdot \mathbf{P}_z\right] \cdot \mathbf{F}\,, \tag{101}$$

where $\mathbf{R} = \mathbf{r} - \mathbf{r}_0$ and $\mathbf{R}^* = \mathbf{r} - \mathbf{r}_0^*$ are the vectors to the observation point from the Stokeslet and image Stokeslet locations respectively. The Cartesian frame can be oriented here such that $\mathbf{F} = F_\parallel \mathbf{e}_x + F_\perp \mathbf{e}_z$. The flow components tangential and vertical to the interface are then

$$\begin{aligned} u_x(\mathbf{r}) &= \frac{F_\parallel}{8\pi\eta}\left[\mathbf{G}(\mathbf{e}_x) + \mathbf{G}^*(\mathbf{e}_x)\right] \\ u_z(\mathbf{r}) &= \frac{F_\perp}{8\pi\eta}\left[\mathbf{G}(\mathbf{e}_z) - \mathbf{G}^*(\mathbf{e}_z)\right]\,, \end{aligned} \tag{102}$$

where we use $\mathbf{G}(\mathbf{e}) = \mathbf{G}(\mathbf{R};\mathbf{e})$ and $\mathbf{G}^*(\mathbf{e}) = \mathbf{G}(\mathbf{R}^*;\mathbf{e})$ as abbreviations to shorten the notation.

The image system for a planar free surface, consisting simply of the mirror reflection of the actual flow singularity, is sketched in Fig. 17 for the two basic situations of the Stokeslet directed along and perpendicular to the plane, respectively. We use here the elemental singularity solution pictograms introduced in Fig. 7. The streamlines for the two cases, based on the flow fields in Eq. (102), are plotted in Fig. 18. By the reflection symmetry of the present image system, it is obvious that the velocity field at the interface is purely tangential. Moreover, since $\mathbf{u}(x,y,z) = \mathbf{u}(x,y,-z)$ by construction, the tangential stress at the interface proportional to $\partial u_{x,y}/\partial z$ is zero.

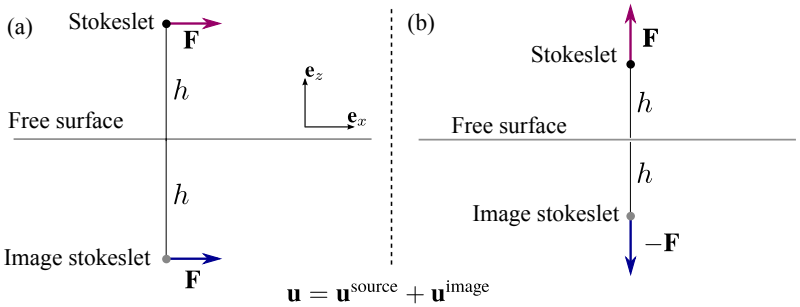

Fig. 17 The image system satisfying the boundary conditions of a free surface is simply the mirror Stokeslet of strength $\mathbf{F}^* = \mathbf{P}_z \cdot \mathbf{F}$. (a) For a point-force oriented parallel to the surface, the image has the same force direction, while (b) for the force pointing towards or away from the surface, the direction of the image force is reversed.

The flow solution for a Stokeslet in front of a planar interface can be used to construct, by superposition, the flow field due to a rigid no-slip body near the interface.

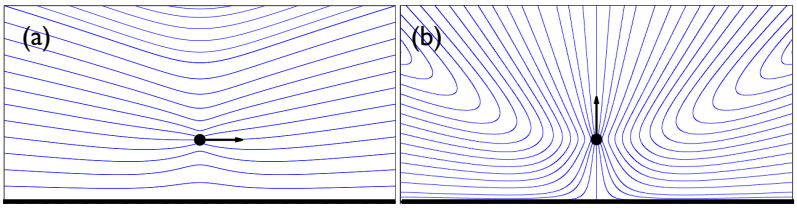

Fig. 18 Flow streamlines (a) due to a point-force oriented parallel to the free surface, and (b) due to a perpendicularly oriented point-fore. Reproduced from [69] with kind permission.

For a free interface, the flow field is determined by

$$\mathbf{u}(\mathbf{r}) = \int_{S_p} dS' \, \mathbf{T}(\mathbf{r}-\mathbf{r}') \cdot \left(\boldsymbol{\sigma}(\mathbf{r}) \cdot \mathbf{n}'\right) + \int_{S_p^*} dS' \, \mathbf{T}(\mathbf{r}-\mathbf{r}') \cdot \mathbf{P}_{z'} \cdot \left(\boldsymbol{\sigma}(\mathbf{r}') \cdot \mathbf{n}'\right) , \quad (103)$$

where S_p^* is the surface of the mirror body, and $\mathbf{P}_{z'} \cdot (\boldsymbol{\sigma}(\mathbf{r}') \cdot \mathbf{n}')$ is the mirror stress field on this surface. This is sketched in Fig. 19.

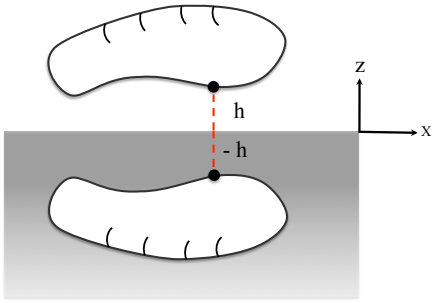

Fig. 19 To determine the flow due to a no-slip particle moving above a planar free surface at $z = 0$, one mentally replaces the surface by an image particle, with the fluid continued into the lower half-space. The surface stress and thus the translational and angular velocities of the image particle are the surface reflections of those of the real particle.

As an interesting problem related to Eq. (103), consider the tangential motion of an isolated no-slip sphere along a planar free interface, in the extreme situation that the sphere is permanently touching the interface in a single point. This quasi-two-dimensional motion is realized to good accuracy in an experimentally well studied system of super-paramagnetic microspheres at the air-water interface of a hanging drop. To determine the single-sphere mobilities starting from Eq. (103), it is crucial to account for lubrication effects in the zero gap case. Lubrication forbids the rotation of the surface-touching sphere along an axis parallel to the surface [70], i.e. $\mu_{\parallel}^{r} = 0$. Rotation is allowed only around the perpendicular sphere axis. While particle surface roughness and remnant undulations in the planar surface should give rise to a non-zero mobility $\mu_{\parallel}^{r}$, the actual effect of lubrication is to lower its value sig-

nificantly below the rotational mobility, μ_0^r, of a sphere in the bulk fluid. A precise calculation of the mobility tensors of hydrodynamically interacting spheres touching a free planar interface was made in [70]. The special result for the mobilities of an isolated sphere is

$$\mu_{\parallel}^t/\mu_t^0 \approx 1.380\,, \quad \mu_{\perp}^r/\mu_r^0 \approx 1.109\,. \tag{104}$$

Owing to the smaller friction experienced by the hemisphere facing the free surface, the translational mobility for motion parallel to the surface is raised above its bulk value by 38 percent, and the rotational mobility $\mu_{\perp}^r$ by mere 11 percent. Note that the sphere is not rotating while translating, since it can be considered as moving side by side in contact with its twin image sphere located just below the free interface. Each of the two twin spheres experiences the same hydrodynamic drag force parallel to the free surface. A microsphere above a no-slip wall which has the freedom to move away from the wall is discussed further down in relation to Fig. 22.

Liquid-liquid interface: The image system for a point force in the presence of a rigid no-slip wall, and more generally of a (clean) fluid-fluid interface was given by Blake in the 1970's [71, 72].

For a Stokeslet parallel, $\mathbf{G}(\mathbf{e}_x)$, and perpendicular, $\mathbf{G}(\mathbf{e}_z)$, to the $(x-y)$ fluid-fluid interface, the image system is given as a function of the viscosity ratio λ by [26]

$$\mathbf{G}_{\mathrm{Im},x}(\mathbf{r}) = \frac{1-\lambda}{1+\lambda}\mathbf{G}^*(\mathbf{e}_x) + \frac{2\lambda h}{\lambda+1}\mathbf{G}_{\mathrm{D}}^*(\mathbf{e}_x,\mathbf{e}_z) - \frac{2\lambda h^2}{\lambda+1}\mathbf{D}_{\mathrm{S}}^*(\mathbf{e}_x)\,, \tag{105}$$

$$\mathbf{G}_{\mathrm{Im},z}(\mathbf{r}) = -\mathbf{G}^*(\mathbf{e}_z) - \frac{2\lambda h}{\lambda+1}\mathbf{G}_{\mathrm{D}}^*(\mathbf{e}_z,\mathbf{e}_z) + \frac{2\lambda h^2}{\lambda+1}\mathbf{D}_{\mathrm{S}}^*(\mathbf{e}_z), \tag{106}$$

where $\mathbf{G}(\mathbf{e}) = \mathbf{G}(\mathbf{R};\mathbf{e})$ and $\mathbf{G}^*(\mathbf{e}) = \mathbf{G}(\mathbf{R}^*;\mathbf{e})$ are used as abbreviations, with analogous abbreviations used for the other elemental singularities. The superscript $(^*)$ indicates that the considered singularity is located at the position, $\mathbf{r}_0^*$, of the image. The Cartesian longitudinal and transversal components of the flow field in the upper half-space $z>0$ are expressed in terms of this image system as

$$u_x(\mathbf{r}) = \frac{F}{8\pi\eta}\left[\mathbf{G}(\mathbf{r};\mathbf{e}_x) + \mathbf{G}_{\mathrm{Im},x}(\mathbf{r})\right], \tag{107}$$

$$u_z(\mathbf{r}) = \frac{F}{8\pi\eta}\left[\mathbf{G}(\mathbf{r};\mathbf{e}_z) + \mathbf{G}_{\mathrm{Im},z}(\mathbf{r})\right], \tag{108}$$

with the force $\mathbf{F}$ of magnitude $F>0$ pointing along the x-axis and z axis, respectively. In the limit $\lambda = 0$ of zero viscosity of the lower half space fluid, the result for a Stokeslet above a free surface is recovered.

No-slip wall: The system of image multipoles at $\mathbf{r}_0^*$ for a no-slip rigid surface, obtained by taking the limit $\lambda \to \infty$ in Eq. (105), has more components than that for the free surface. The reason for this is that in addition to a zero normal velocity component at the interface, also the tangential fluid velocity component must be zero.

The pictogram representation of the image system for a no-slip wall is shown in Fig. 20, for the strength **F** of the Stokeslet oriented parallel (a) and (b) perpendicular to the wall. The image system for the general case of a tilted Stokeslet is obtained by linear superposition. The image system has now two members in addition to the image Stokeslet in the free surface case, namely a Stokes doublet of strength modulus $2hF$, and a source doublet of strength modulus $2h^2F$. The streamlines for a Stokeslet parallel and perpendicular to the no-slip wall are shown Fig. 21. Notice the pronounced flow vortices in the latter case, with fluid dragged in behind the up-pointing Stokeslet. For a detailed discussion of the image system solution we refer to Blake's original work. Quite interestingly, the presence of a no-slip wall changes the asymptotic behaviour of the flow field in the upper half-space at distances far from the Stokeslet and the wall. Although the image Stokes doublet and source doublet contributors to the velocity field decay faster than the two Stokeslet contributors, there is a long-distance flow cancellation. As a result, the velocity field decays asymptotically as $\mathscr{O}(r^{-2})$, for the Stokeslet oriented parallel to the wall, and an even faster $\mathscr{O}(r^{-3})$ decay is found for the perpendicularly oriented Stokeslet [71]. This is an example of hydrodynamic screening induced by a stationary no-slip boundary which takes momentum out from the fluid.

The method of images can be successfully applied also to the case of higher-order elemental singularities near a planar wall such as a Stokes dipole, Rotlet, Rotlet dipole and source doublet [26, 73]. These solutions are quite useful, e.g., to describe the hydrodynamic attraction of a bacterial microswimmer by an interface, and its resultant circular motion.

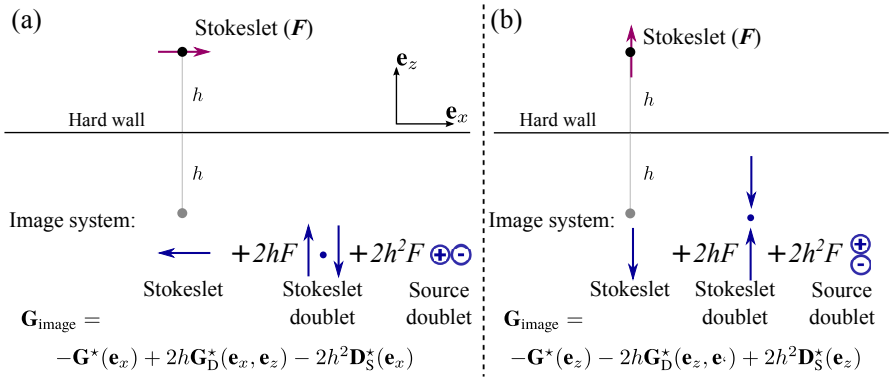

Fig. 20 The image system satisfying the no-slip BC at a rigid wall is more complex than that for a free surface. The three different flow singularities of the image system and their respective strengths are expressed as pictograms defined in Fig. 7(a)-7(f). The image singularity solutions are all located at the mirror point of the Stokeslet in the actual upper fluid. Note that in (a) the mirror Stokeslet is oppositely oriented. Redrawn after [71].

Partial-slip wall: The image system for a planar rigid wall with Navier partial-slip boundary conditions is more complicated than that for a liquid-liquid interface,

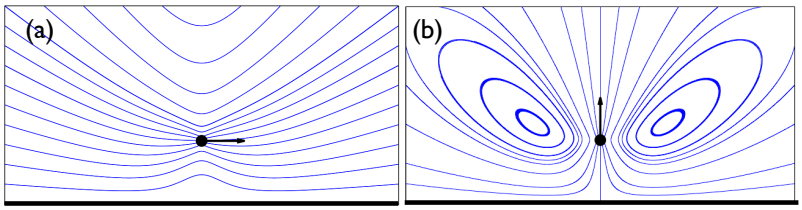

Fig. 21 Flow field streamlines for a point force located above a no-slip wall, with the wall represented by the thick bottom line. Parallel (a) and perpendicular (b) orientations of the Stokeslet are considered. Reproduced from [69] with kind permission.

except for the zero and infinite slip length limits where likewise the no-slip wall and free surface are recovered. As shown by Lauga and Squires in [74], the image system for the perpendicularly oriented Stokeslet contains the same set of elemental singularity solutions as that for a liquid-liquid interface. However, these are now continuously distributed along a line extending from the reflection point $\mathbf{r}_0^*$ into the negative $\mathbf{e}_z$ direction, with magnitudes that decay exponentially downside this line over the slip length ℓ. For $\ell \to 0$, Blake's solution for a no-slip wall is recovered. The image system for a Stokeslet parallel to the partial-slip wall involves a larger set of elemental singularity solutions, likewise distributed along the aforementioned singularity line. The system include now also a Rotlet and a Rotlet dipole. Here, not all singularity solution magnitudes decay exponentially in going downside along the line.

5.2 Spherical particle motion near a no-slip wall

The hydrodynamic problem of the motion of a spherical particle in a viscous liquid bounded by a planar no-slip wall has been studied since more than a century. The difficulty of the problem relates to the fact that BCs must be satisfied both at the wall and the sphere surface.

Anisotropic mobilities: Owing to the BCs both for the sphere and the wall, the 6×6 mobility matrix characterizing the translational and rotational motion of the sphere near the wall is of an anisotropic character, with scalar elements (mobility coefficients) depending on the distance z of the sphere centre to the wall extending into the $x-y$ plane. Five independent mobility coefficients are required to characterize the sphere motion, as depicted in Fig. 22. The four coefficients $\mu_{\parallel}^{t}$, $\mu_{\perp}^{t}$, $\mu_{\parallel}^{r}$, $\mu_{\perp}^{r}$ characterize the translational and rotational sphere motion parallel and perpendicular to the wall, while the additional coefficient μ^{tr} describes the wall-induced coupling of translational and rotational motion. A torque-free sphere translating parallel to a near-distant wall is rotating. This should be contrasted to the motion of a sphere far distant from the wall which is fully characterized by the two bulk coefficients μ_0^t and μ_0^r given in Eq. (25), without any translational-rotational coupling.

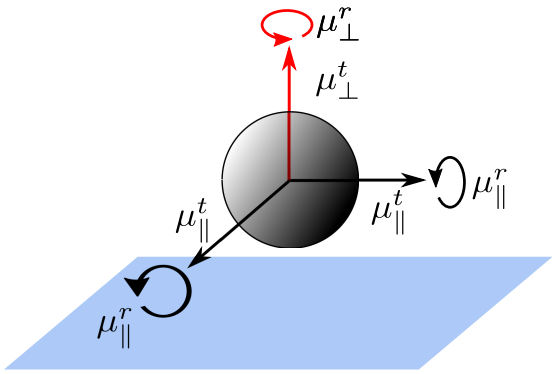

Fig. 22 Schematic representation of mobility coefficients describing the near-wall translational (superscript t) and rotational (superscript r) motions of a rigid microsphere parallel and perpendicular to a planar wall. Not depicted is an additional mobility coefficient, $\mu^{tr} = \mu^{rt}$, characterizing the wall-induced translation-rotation coupling of the sphere motion. See the text and [75] for details.

The mobility matrix for a sphere near a planar wall is of the form

$$\boldsymbol{\mu}(z) = \begin{pmatrix} \boldsymbol{\mu}^{tt}(z) & \boldsymbol{\mu}^{tr}(z) \\ \boldsymbol{\mu}^{rt}(z) & \boldsymbol{\mu}^{rr}(z) \end{pmatrix}, \tag{109}$$

with all coefficients depending on the sphere-wall distance z. The components of the tt submatrix have in the selected coordinate frame the simple structure

$$\boldsymbol{\mu}^{tt}(z) = \begin{pmatrix} \mu_\perp^{tt}(z) & 0 & 0 \\ 0 & \mu_\parallel^{tt}(z) & 0 \\ 0 & 0 & \mu_\parallel^{tt}(z) \end{pmatrix}, \tag{110}$$

with a similar structure for the rotational rr submatrix. The structure of the rt and tr coupling tensors is different (see, e.g., [76, 75]).

Numerous works have been devoted to the evaluation of the z-dependence of the mobility coefficients, dating back to Lorentz [77] and Faxén [78] more than a century ago who calculated the first terms in the expansion of the two translational coefficients in terms of the reciprocal sphere-wall distance, $t = a/z$, in units of the sphere radius, given by

$$\mu_\parallel^t(t) \approx 1 - \frac{9}{8}t, \tag{111}$$

$$\mu_\perp^t(t) \approx 1 - \frac{9}{16}t + \frac{1}{8}t^3 - \frac{45}{256}t^4 - \frac{1}{16}t^5. \tag{112}$$

These expressions provide a crude approximation of the exact translational coefficients for large sphere-wall distances $z/a \geq 10$. Subsequent refined calculations by Brenner *et al.* [15, 79, 80, 81] and Dean and O'Neill [82, 83] have led to formally exact expressions for part of the mobility coefficients in terms of infinite series. While frequently quoted, these series expressions are of limited practical importance owing to their slow convergence at near-contact distances. More recently, numerically precise and convenient inverse distance series results for all five mobility coefficients have been obtained, using a high-precision numerical scheme based on the

force multipoles method by Cichocki and Jones [76] combined with a Padé approximation used for incorporating near-contact lubrication effects.

For the presentation of these numerical results, we introduce dimensionless mobilities by division through respective bulk mobility coefficients according to

$$\widetilde{\mu}^t_{\parallel,\perp} = \frac{\mu^t_{\parallel,\perp}}{\mu^t_0}, \qquad \widetilde{\mu}^r_{\parallel,\perp} = \frac{\mu^r_{\parallel,\perp}}{\mu^r_0}, \qquad \widetilde{\mu}^{tr} = \frac{\mu^{tr}}{a\mu^r_0}. \tag{113}$$

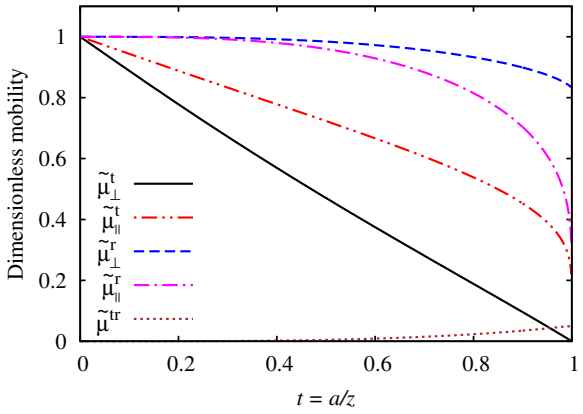

Fig. 23 Dimensionless mobility coefficients, defined in Eq. (113), of a no-slip microsphere near a planar no-slip wall, as functions of the dimensionless reciprocal sphere-wall distance $t = a/z$. At sphere-wall contact where $t = 1$, all mobilities except for $\mu^r_\perp$ are vanishing. The effect of translation-rotation coupling, absent both at contact and far away from the wall, is strongest near sphere-wall contact where $\tilde{\mu}^{tr}$ attains its largest value of about 0.05. Mobility coefficients have been obtained using the method in [76].

The dimensionless mobility coefficients for a no-slip sphere near a planar no-slip wall are plotted in Fig. 23, as functions of the inverse distance parameter t. Significant deviations from the bulk mobility values are observed for distances $z/a < 5$. The slowing hydrodynamic effect of the wall is in general more pronounced for translational than rotational motion. Physical processes where this can be of importance are cellular adhesion [6], and channel flows where translation is hindered but rotation is still strong enough to allow for the reorientation of particles in external fields [84]. All mobility coefficients except for $\mu^r_\perp$ go to zero in a non-analytical way when the contact distance $t = 1$ is approached. It follows from lubrication theory that the asymptotic behaviour of the mobility coefficients close to the wall can be expressed in terms of the dimensionless gap width $\varepsilon = (z-a)/a$ [76]. In the case of translational coefficients, one finds

$$\widetilde{\mu}^t_\perp \sim \varepsilon + \frac{1}{5}\varepsilon^2 \log\varepsilon, \qquad \widetilde{\mu}^t_\parallel \sim -2(\log\varepsilon)^{-1}. \tag{114}$$

Wall lubrication effects imply also that $\mu^r_{\parallel}(t \to 1) = 0$, whereas the sphere rotation with the angular velocity oriented perpendicular to the wall is possible even at contact where the related mobility coefficient $\mu^r_{\perp}$ is reduced by about 18 percent below the isotropic bulk value. The coefficient μ^{tr} relating translational motion to applied torque is zero at sphere-wall contact since lubrication implies zero translational velocity of the sphere at wall contact.

Mobility measurement by light scattering: The theoretical predictions for the distance dependence of the mobility coefficients of an isolated microsphere near a wall have been scrutinized in experimental studies, for sphere sizes ranging from about 100 nm up to several microns, using various optical techniques. These techniques include optical trap microscopy [85], nano-PIV [86, 87], dynamic light scattering (DLS) in presence of two parallel walls [88], low-coherence DLS [89], resonance-enhanced DLS [90, 91], and evanescent wave dynamic light scattering (EWDLS) in a system bounded by one or two walls [27, 92, 93, 94, 95]. However, only recently has it been possible to determine both the translational and rotational diffusion of a colloidal sphere in the vicinity of a planar wall [75, 96], using EWDLS from optically anisotropic spherical particles. In many experiments such as in EWDLS, the relation

$$\mathbf{D} = k_B T \boldsymbol{\mu}\,, \tag{115}$$

between the hydrodynamic mobility matrix and the diffusion matrix, $\mathbf{D}$, of a dispersed Brownian particle at system temperature T is used, on measuring the diffusion matrix coefficients instead of the associated hydrodynamic mobility coefficients.

Light scattering is a powerful tool to investigate the properties of sub-micron soft matter systems [97]. In evanescent wave scattering experiments, a colloidal suspension is typically illuminated by a monochromatic laser beam that is totally reflected from a planar glass surface bounding the sample, so that no refracted light enters into the suspension (which is placed above the glass surface in Fig. 24) except for an evanescent wave whose intensity decays exponentially in going away from the glass surface into the suspension. Thus, only a colloidal particle close to the glass surface scatters enough of the incident evanescent light to be detected. The penetration depth, $2/\kappa$, of the evanescent can be changed to probe the particle diffusion at different glass surface-particle distances. For a review of the EWDLS method including experimental details, see [98].

The key quantity determined in (EW)DLS experiments is the scattered light intensity time-autocorrelation function. Of particular significance is the short-time (initial) decay rate, Γ, of the intensity autocorrelation function referred to as the first cumulant. This quantity can be theoretically predicted on basis of the generalized Smoluchowski equation determining the evolution of the configurational probability density function of Brownian particles under Stokes flow conditions [1, 99]. Inside the bulk region of a very dilute suspension of colloidal hard spheres far away from confining walls, the first cumulant is proportional to $\Gamma = q^2 D^0$, where q is the modulus of the scattering vector $\mathbf{q}$, and $D^0 = k_B T \mu^t_0$ is the translational (Stokes-Einstein) diffusion coefficient of an isolated Brownian sphere.

In the data analysis gained from a typical EWDLS set-up such as the one sketched in Fig. 24, one conveniently decomposes the scattering vector into its components parallel and perpendicular to the wall, $q_\parallel$ and $q_\perp$, respectively. The first cumulant for the translational motion of a Brownian sphere near the glass wall is then given by

$$\Gamma = q_\parallel^2 \left\langle D_\parallel^0 \right\rangle_\kappa + \left(q_\perp^2 + \frac{\kappa^2}{4} \right) \left\langle D_\perp^0 \right\rangle_\kappa, \tag{116}$$

where $D_\parallel^0(z) = k_B T \mu_\parallel^t(z)$ and $D_\perp^0(z) = k_B T \mu_\perp^t(z)$, and $\langle \cdots \rangle_\kappa$ denotes a κ-dependent weighted average of the z-dependent diffusion coefficients over all sphere - glass wall separations z, for a given evanescent wave penetration parameter κ. The average diffusion coefficients in Eq. (116) for translational diffusion parallel and perpendicular to the glass wall are not purely statistical mechanical properties but are dependent on the value of κ selected in the optical setup: The smaller κ is the larger are the resulting average diffusion coefficients [95]. For a smaller κ, diffusion is detected in EWDLS over a larger distance from the glass wall, and $\mu_\parallel^t(z)$ and $\mu_\perp^t(z)$ are increasing with increasing wall-sphere distance z.

By determining Γ as a function of $q_\parallel$ for fixed $q_\perp$ and vice versa, the two average translational diffusion coefficients are obtained using Eq. (116). Moreover, on the basis of an analytic expression for the first cumulant generalized to optically anisotropic spherical particles, the distance-averaged rotational diffusion coefficients are obtained in a light polarization-sensitive EWDLS experiment in addition to the translational ones [75, 96].

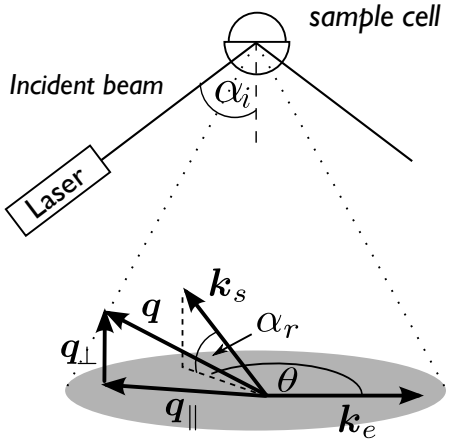

Fig. 24 Schematics of an EWDLS set-up. The wave vectors of the incident evanescent and scattered light beams are $\mathbf{k}_e$ and $\mathbf{k}_s$, respectively, with their difference defining the scattering vector $\mathbf{q} = \mathbf{k}_s - \mathbf{k}_e$. Independent experimental variation of the components $q_\parallel$ and $q_\perp$ of the scattering vector parallel and perpendicular to the confining glass wall allows for the determination of wall-distance averaged diffusion coefficients. See the text for details. Redrawn after [95].

Hydrodynamic radius models: Transport properties of colloidal suspensions such as the viscosity and translational and rotational diffusion coefficients depend in principle on the details of the hydrodynamic particle structure, e.g. on the particle surface BC, and the fluid permeability profile in the case of fluid-permeable particles. Important examples of particles with internal structure are micro- and nanogels, non-permeable rigid particles with surface corrugation, and core-shell particles consisting of a dry core coated by a polymer brush. The hydrodynamic effect of the in general quite complicated intra-particle structure can be characterized under surprisingly general conditions by a single parameter, namely the effective hydrodynamic radius a_{eff}. For globular particles, this radius can be determined experimentally in a DLS experiment on using the single-sphere Stokes-Einstein relation for the diffusion coefficient D^0. The hydrodynamic radius is the radius of an effective no-slip sphere with the same diffusion coefficient as the one of the actual internally structured particle. It has been shown in recent theoretical work [100] that the error introduced by simply using a_{eff} for the particle structure characterization can be well controlled.

5.3 Near-wall dynamics of anisotropic and flexible particles

The presence of a nearby wall or interface drastically affects the hydrodynamics experienced by a microparticle. This can be easily understood qualitatively using symmetry arguments. Since the hydrodynamic friction experienced by a particle is in general larger on the side of the particle facing the wall, there is translational-rotational coupling even for a highly symmetric particle such as a sphere with uniform surface BC. For a non-spherical particle, there is an additional dependence of the friction coefficients on the particle orientation giving rise to interesting dynamic effects.

For an example, consider the sedimentation of a rod-like rigid particle near a vertical rigid wall. As we have discussed earlier, an inclined rod in an unbounded fluid has a horizontal side drift while settling but it does not reorient its body axis. This absence of rod reorientation/rotation does not hold any more in sedimentation close to a vertical wall. It has been experimentally observed and numerically calculated by Russel *et al.* [101] for a no-slip rod sedimenting near to a no-slip vertical wall that there are two possible sedimentation scenarios. The first one is a glancing motion, where one tip of the rod always points downwards while the rod is reorienting close to the wall, and the second one a reversing motion, where the rod tumbles while approaches its closest distance to the wall. In both scenarios, the wall to centre-of-rod distance decreases initially during sedimentation, increasing again subsequently. Which of the two scenarios is taking place depends on the initial wall distance and inclination angle of the rod. To gain a quantitative understanding of the rod Stokesian dynamics, a slender-body analysis for the motion of an elongated microparticle close to a flat fluid-fluid interface has been made for determining the drag force and torque acting on it for a fixed spatial orientation [102].

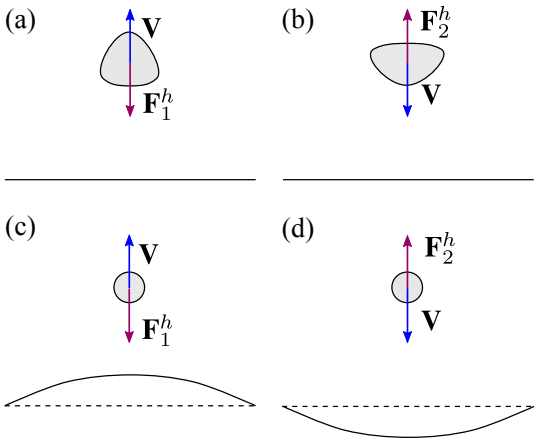

Fig. 25 Sketch of two physical situations where kinematic reversibility is not applicable owing to hydrodynamically induced particle (in (a)-(b)) or interface (in (c)-(d)) deformations. In (a)-(b), a flexible particle is deformed differently if moving towards or away from a rigid flat interface. In (c)-(d), the flexible interface experiences a local deformation different for a rigid particle moving towards or away from the interface. The frictional force, $\mathbf{F}^h$, experienced by the particle is likewise dependent on the motion direction, since the distance to the deformed interface in (c) is smaller than in (d).

The motion of a flexible microparticle is more complicated than that of a rigid one, owing to inevitable hydrodynamically induced particle surface deformations which invalidate the simple kinematic reversibility arguments for the associated Stokes flows. As an illustration, consider in Fig. 25 (a) and (b) a flexible particle (say a droplet or vesicle) moving away or towards a rigid planar wall, respectively. During its motion, the particle will deform in a way controlled by the interplay of fluid stresses and particle surface tension. The latter tends to restore the spherical particle shape of minimal surface free energy which it would have if the fluid and particle were stationary. The particle deformations are different for (a) and the oppositely directed motion in (b), since the distribution of friction forces (stresses) along the particle surface is different in the two cases. Since symmetry is here obviously broken, kinematic reversibility arguments can not be used to gain information on the particle motion. The changing shape of an elastic body approaching a rigid flat wall has been numerically calculated, e.g., for a liquid droplet sedimenting in another fluid [103]. Elasticity effects can lead to cross-stream migration of flexible particles [40] which is of importance in blood flows, where the suspended corpuscles are often highly elastic, in cell adhesion problems in shear flows [104], and for industrial processes involving macromolecules or polymer flows [105].

So far we have assumed that the interface in the proximity of a particle is rigid. This is a valid assumption for non-deformable container walls or liquid-liquid interfaces of large interfacial tension. Deformable interfaces give rise to additional effects. The motion of a rigid particle towards or away from a flexible interface causes a motion-dependent local deformation of the interface. This is related to a

special type of particle-interface interaction through the geometric coupling of local interface shape and flow [106]. A rigid particle moving away from the interface sketched in Fig. 25(c) pulls the fluid along with it which in turn causes a local deformation in the flexible interface extending in the direction of the particle motion. This results in an enlarged hydrodynamic friction force on the particle as compared to the flat-surface situation, i.e. $F_1^h > F_{\text{flat}}^h$. The geometric coupling for the oppositely oriented particle motion in figure part (d) leads to a frictional force on the particle smaller than in the flat interface case so that $F_2^h < F_{\text{flat}}^h$. This is reminiscent of the lift force acting on deformable particles in flow, and is of interest for biological system flows under elastic confinement. Quite interestingly, the vicinity of a soft interface or object can be used by microorganisms in their propulsion even if performing reciprocal motions [107], since the micro-scallop theorem discussed in Sec. 6 does not apply near a flexible surface [108].

6 Self-propelling microswimmers

The locomotion and transport of autonomous (self-propelling) biological and artificial microswimmers under low-Reynolds-number flow conditions has generated a lot of interest over the past years. See here [108, 109] for two very informative overview articles, and a classical book by Lighthill [110]. The motility of microorganisms such as bacteria, sperm cells, and algae affects many biological processes including reproduction and infection. Appropriate swimming strategies are essential for microorganisms in their search for food or the avoidance of toxic environments (chemotaxis), the reaction to light (phototaxis), and the orientation under gravity (gravitaxis). The theoretical design and fabrication of synthetic (robotic) microswimmers who can transport cargo or remove toxins bears the perspective of highly useful applications in medicine, biology and environmental science.

Autonomous swimmers are characterized by the absence of an external forcing agent driving their translational and rotational motion. For microswimmers under Stokes-flow conditions, this means

$$\mathbf{F}^h(t) = \mathbf{0}, \quad \mathbf{T}^h(t) = \mathbf{0}, \tag{117}$$

expressing that the total hydrodynamic drag force and torque exerted on the swimmers are zero at any instant of time. The long-distance decay of the disturbance fluid velocity field caused by the swimmer's motion is thus of $\mathcal{O}(r^{-2})$ or faster.

There are a variety of autonomous propulsion mechanisms. For instance, a microobject could swim by self-diffusiophoresis, by creating through a surface-active site a small gradient, $\nabla\phi$, in the concentration ϕ of a dissolved species (solute). This self-created gradient, in turn, propels the microobject through the phoretic osmotic solute flow in its interfacial region [48, 52], with the self-phoretic velocity, $\mathbf{V}_{\text{phor}}$, of the object determined by Eq. (79). The potential flow outside the self-phoretic object has thus the characteristic $\mathcal{O}(r^{-3})$ far-distance decay.

6.1 Purcell's micro-scallop theorem

We focus here on purely mechanical microswimmers which self-propel by continuously changing their body shape in a periodic way. After one cycle, the microswimmer returns to its initial body shape.

Two conditions have to be fulfilled to achieve a net translational displacement after one cycle of body shape deformations. The first one known as Purcell's micro-scallop theorem [22, 111] is related to the kinematic reversibility of Stokes flows. It reads

> *In the absence of inertia, the periodic sequence of body shape configurations must be non-reciprocal, that is it must be different when viewed in a time-reversed way.*

This excludes in particular cyclic shape changes depending on a single parameter only. For the scallop theorem to apply, it is understood that the single-parametric microobject is far away from a flexible interface which invalidates kinematic reversibility arguments (c.f. Subsec. 5.3). As an illustrative example of the no-go scallop theorem consider with Purcell in Fig. 26 a (one-hinge) symmetric micro-scallop in the bulk fluid periodically opening and closing its legs. While shaking back and forth, the net displacement after one cycle is zero. The opening angle φ is here the only parameter characterizing different shapes, and the sequence of different shapes is thus necessarily reciprocal.

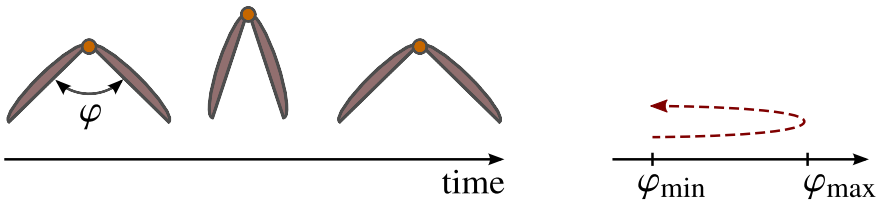

Fig. 26 Left: A symmetric micro-scallop shakes back and forth during one motion cycle without a net vertical translation. Right: The sequence of shape configurations in the one-dimensional parameter space is necessarily reciprocal.

A non-reciprocal sequence of cyclic shape deformations is not sufficient to achieve a net propulsion under Low-Reynolds-number conditions. An additional requirement, applying also to non-small Reynolds number locomotion, is:

> *Successful self-propulsion requires an anisotropy or asymmetry in the fluid friction experienced by the moving swimmer.*

The net displacement of an isolated microswimmer does not depend on the rate at which a given non-reciprocal sequence of shape configurations occur (rate independence) but only on their geometry.

Many microorganisms such as bacteria and spermatozoa have an elongated body with a distinct body axis or polarity which dictates the direction of their motion. Roughly speaking, such a microorganism consists of a passive head part and a slender active filament (flagellum). Animalcules such as sperms are propelled by wave-like beating of their flagellum which causes them to move in the direction opposite to that of the flagellar wave travelling away from the head. Unlike eukaryotic flagella, bacterial flagella are passive fibers incapable of active bending. They use instead a helical wave propulsion, in the form of a rotating rigid helical bundle of flagella driven by a molecular motor at the cell body. If viewed from behind in swimming direction, the flagellar bundle rotates counter-clockwise. The torque introduced by this rotation is balanced by the clockwise rotation of the cell body.

In both propulsion mechanisms, swimming is possible because of the friction anisotropy and non-reciprocal travelling wave deformations of the flagellum. The slender flagellum can be mentally subdivided, at any instant, into rod-like segments characterized by two segmental friction coefficients $\zeta_\perp \approx 2\zeta_\parallel$. The force $\Delta\mathbf{F}_\mathrm{s}$ exerted on the fluid by a segment moving with instantaneous velocity $\mathbf{v}$ is

$$\Delta\mathbf{F}_\mathrm{s} = \zeta_\parallel \mathbf{v}_\parallel + \zeta_\perp \mathbf{v}_\perp \,, \tag{118}$$

where $\mathbf{v}_\parallel$ and $\mathbf{v}_\perp$ are the velocity projections parallel and perpendicular to the segment, determined by the instant shape and rate of change of shape of the swimmer. Integration over the filament contour leads to the momentary propulsion (thrust) force,

$$\mathbf{F}_\mathrm{prop} \propto \left(\zeta_\perp - \zeta_\parallel\right) \mathbf{e} \,, \tag{119}$$

along the body axis $\mathbf{e}$ of the swimmer who is kept stationary for this first calculation step. The propulsion force is proportional to the difference of the segment friction coefficients and points from the filament to the head. See [108] for the details of such a calculation, e.g., for a simplified sperm model with a two-dimensional wave-like beating pattern. The propulsion force must be balanced at any instant by a hydrodynamic drag force, $F^h(t) = -F_\mathrm{prop}(t)$, exerted by the fluid on the instantaneously frozen-in shape of the swimmer, which is moving in this second calculation step with the searched for instantaneous axial swimming velocity $V(t)$. From a decent estimate of the axial friction coefficient of the frozen-in swimmer appearing in the relation $F^h(t) = -\zeta_\mathrm{froz}(t)V(t)$, the instantaneous swimming velocity is approximately obtained. The here outlined procedure is once again a direct consequence of the additivity of Stokes flow solutions, and of the associated particle velocities. Since both F_prop and F^h are proportional to η, the swimming velocity is independent of the fluid viscosity. However, the rate of dissipated energy caused by swimming depends on the viscosity.

6.2 Dipole swimmers

The flow around an isolated axial microswimmer with flagellar propulsion is in general well approximated by a linear force dipole (linear Stresslet), $\mathbf{G}_D(\mathbf{r};\mathbf{e},\mathbf{e})$, in the direction of the swimmer's body axis $\mathbf{e}$. The two infinitesimally distant Stokeslets pointing away from each other represent the balance of propulsive and drag forces discussed above. This far-distance flow model is valid for distances larger than the axial extension L of the swimmer. Higher-order elemental multipoles containing additional information on the shape and near-distance motion come into play when microswimmers get close to each other or to a boundary [26, 41, 108, 109].

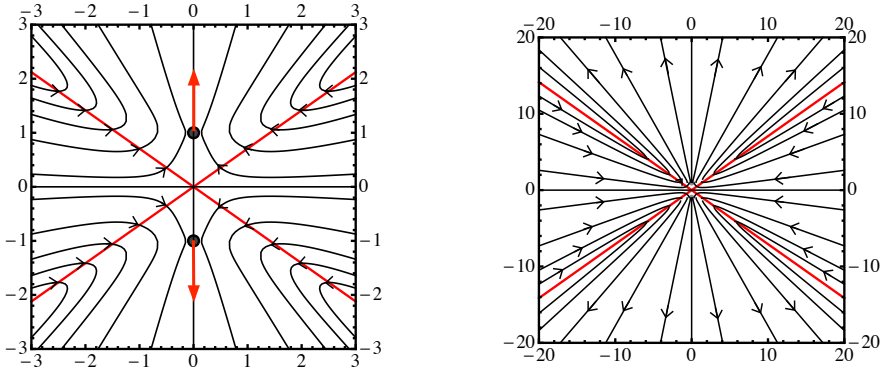

Fig. 27 Streamlines of a linear Stokeslet dipole (force dipole) oriented along the z axis with positive dipole moment $p > 0$ (pusher). Lengths are scaled in units of d, and $p/(8\pi\eta d^2) = 1$. Left: Near-field streamlines of the oppositely oriented Stokeslets. Right: Streamlines of the ideal force dipole. The two separatrix lines $z = \pm x/\sqrt{2}$ separate the sectors of in- and outflowing fluid. Reproduced from the COMPLOIDS book [9] with kind permission of the Societa Italiana di Fisica.

With the dipole singularity positioned at the origin, and the dipole orientation along $\mathbf{e} = \mathbf{e}_z$, the dipole flow field is

$$\mathbf{u}_{\mathrm{D}}(\mathbf{r};\mathbf{e}) = \frac{p}{8\pi\eta}\mathbf{G}_{\mathrm{D}}(\mathbf{r};\mathbf{e}_z,\mathbf{e}_z) = \frac{p}{8\pi\eta\, r^2}\left[3\,(\hat{\mathbf{r}}\cdot\mathbf{e})^2 - 1\right]\hat{\mathbf{r}}. \tag{120}$$

Note that $(\hat{\mathbf{r}}\cdot\mathbf{e}) = \cos(\psi)$, with ψ denoting the angle between the dipole (swimmer) axis $\mathbf{e}$ and the fluid observation point at $\mathbf{r}$. The streamlines of the dipole velocity field are depicted in Fig. 27 for $p > 0$, where the two Stokeslets are pointing away from each other. The dipole strength scales as $|p| \sim \eta |V| L^2$ where V is the swimming speed and L the axial length of the elongated swimmer. Notice here the distinct differences in the linear Stresslet field of a dipolar microswimmer, and the source doublet potential flow field of an auto-phoretic microswimmer. The Stresslet velocity field is in particular longer-ranged than the potential flow velocity field of a phoretic swimmer.

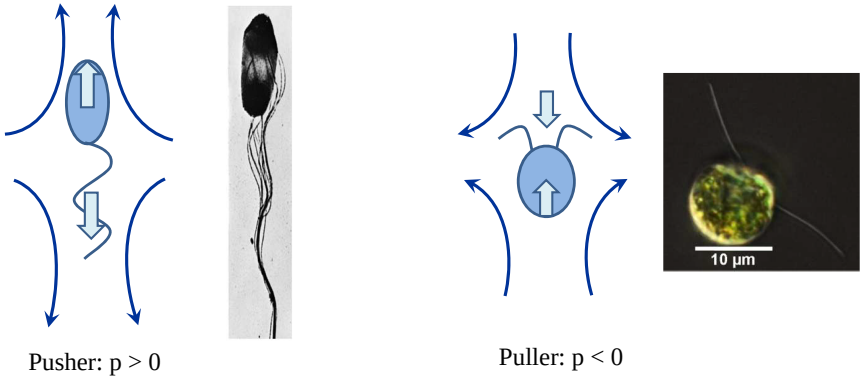

Fig. 28 Left: Schematics of the far-distant flow and associated linear force dipole (arrows) of a pusher ($p > 0$) with the *Salmonella* bacterium as an example. Right: Schematics of a puller ($p < 0$) with the green algae *Chlamydomonas* as an example. The swimming direction (unit vector) **e** is here in the upward direction. Reproduced from the COMPLOIDS book [9] with kind permission of the Societa Italiana di Fisica.

Microswimmers with a positive dipole moment are called *pushers*. They have their active propelling part on their rear side, and as seen in Fig. 28 they push the fluid out along the long (swimming) axis (repulsive flow) and draw fluid in on their side (attractive flow field). The aforementioned microrganisms are all pushers in addition to many types of bacteria. Microswimmers with a negative dipole moment ($p < 0$) are termed *pullers*. Their streamline pattern is the same as that for pushers, however with the flow direction reversed since the two Stokeslets are now pointing towards each other. Pushers pull in fluid along their long swimming sides (attractive flow) and push it out at their side (repulsive flow). An example of a puller is the green algae *Chlamydonamas rheinhardtii* which swims with two head-sided flagella in a breast-stroke-like motion.

6.3 Hydrodynamic interactions between swimmers

Two pushers swimming side-by-side attract each other, while being repulsive if swimming one behind the other into the same direction. While this behaviour can be obviated qualitatively from the dipole flow pattern for $p > 0$ depicted in Fig. 27, it can be more quantitatively discussed by considering the motion of one force dipole in the incident dipolar flow field of the other one. On employing the translational Faxén theorem for point-like torque- and force-free objects (see Eq. (90)), the velocity increments, $\mathbf{V}_i$, of the two equal-moment dipoles at positions $\mathbf{R}_i$ are

$$\mathbf{V}_1 = \mathbf{u}_\mathrm{D}(\mathbf{R}_{12};\mathbf{e}_2) = \frac{p}{8\pi\eta\,(R_{12})^2}\left[3\left(\hat{\mathbf{R}}_{12}\cdot\mathbf{e}_2\right)^2 - 1\right]\hat{\mathbf{R}}_{12} \tag{121}$$

$$\mathbf{V}_2 = \mathbf{u}_\mathrm{D}(\mathbf{R}_{21};\mathbf{e}_1)\,, \tag{122}$$

respectively, with $\mathbf{R}_{ij} = \mathbf{R}_i - \mathbf{R}_j$ and $i,j \in \{1,2\}$.

If the two swimmers move momentarily side-by-side in the same direction so that $\hat{\mathbf{R}}_{12}\cdot\mathbf{e}_i = 0$, they acquire the relative velocity increment

$$\mathbf{V}_1 - \mathbf{V}_2 = -\frac{p}{4\pi\eta\,(R_{12})^2}\hat{\mathbf{R}}_{12}\,, \tag{123}$$

expressing that pusher 1 is hydrodynamically attracted to pusher 2, and vice versa. To see this just view the relative motion in the rest frame of pusher 2 where $\mathbf{V}_2 = \mathbf{0}$. For pusher 2 following pusher 1, we have $\left(\hat{\mathbf{R}}_{12}\cdot\mathbf{e}_i\right)^2 = 1$, and the velocity difference describes now the hydrodynamic attraction of the two swimmers. The opposite trends apply to two pullers owing to their negative force dipole moments.

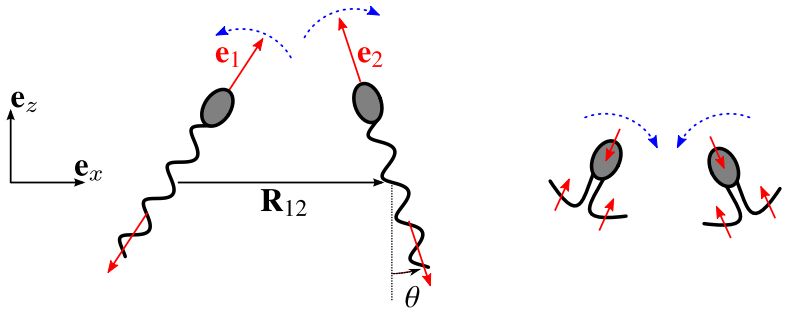

Fig. 29 Left: Two pushers ($p > 0$) on a not too diverging course attract each other hydrodynamically, and reorient each other into a parallel side-by-side motion. Right: Two pullers ($p < 0$) on a diverging course reorient each other towards an antiparallel configuration, swimming subsequently away from each other in anti-parallel direction (see also [108]).

This is not the whole story for arbitrary orientations and positions of the two swimmers. The flow field $\mathbf{u}_\mathrm{D}(\mathbf{r};\mathbf{e}_2)$ created by swimmer 2 at the centre position $\mathbf{R}_1$ of swimmer 1 has rotating and straining parts, $(\nabla\times\mathbf{u}_\mathrm{D})$ and $\mathbf{E}_\mathrm{D} = \frac{1}{2}\left(\nabla\mathbf{u}_\mathrm{D} + (\nabla\mathbf{u}_\mathrm{D})^T\right)$, respectively. Swimmer 1 exposed to the flow field of swimmer 2 has thus the tendency to align itself with the principal axis (dilation axis) of the strain field part $\mathbf{E}_\mathrm{D}(\mathbf{R}_{12};\mathbf{e}_2)$ of swimmer 2. For a quantitative analysis, let us model swimmer 1 geometrically overall as a force-free and torque-free prolate spheroid of aspect ratio $\Gamma > 1$, with the long-axis orientation unit vector $\mathbf{e}_1$. A general rotational Faxén theorem for a no-slip spheroid states [14] that if the spheroid with its centre at position $\mathbf{R}_1$ is subjected to an arbitrary incident Stokes flow field $\mathbf{u}(\mathbf{r})_\mathrm{inc}$, it will rotate with an angular velocity $\boldsymbol{\Omega}_1$ given by

$$\boldsymbol{\Omega}_1 = \frac{1}{2}\left(\nabla \times \mathbf{u}_{\rm inc}\right)(\mathbf{R}_1) + \left(\frac{\Gamma^2-1}{\Gamma^2+1}\right)\mathbf{e}_1 \times \left(\mathbf{E}_{\rm inc}(\mathbf{R}_1)\cdot\mathbf{e}_1\right) + \cdots . \tag{124}$$

The dots annotate that higher order derivative contributions of the incident flow field are neglected. A freely advecting sphere for which $\Gamma = 1$ rotates thus with half the vorticity of the incident flow $\mathbf{u}_{\rm inc}$, taken at the sphere center. An elongated body has an additional angular velocity part due to the shear strain part of the incident flow. This additional angular velocity part is oriented perpendicular to the long body axis unit vector $\mathbf{e}_1$ of swimmer 1.

Substitution of $\mathbf{u}_{\rm D}(\mathbf{R}_{12};\mathbf{e}_2)$ for the incident flow into Eq. (124) reveals that two nearby pushers on a converging course reorient each other hydrodynamically into a parallel side-by-side configuration. As depicted in the left part of Fig. 29, if two pushers located in the $x-z$ plane are separated by the distance $h = R_{12}$, and symmetrically oriented with inclination angles $\pm\theta$ relative to the z axis, their reorientation into a parallel configuration takes place with the angular velocities $\Omega_{y,12} \sim \mp p\theta/(\eta h^3)$ [108]. In contrast, and owing to the opposite flow fields, two pullers on a diverging course align each other in an antiparallel configuration, swimming subsequently away from each other. This is illustrated in the right part of Fig. 29.

It should be recalled that the analysis presented here is based on the leading-order singularity flow solutions. It applies in principle to inter-swimmer distances h large compared to the elongational swimmer size L only, although it is often found to be quite accurate even for distances comparable to L [109]. For two closely moving swimmers, the details of their shapes and propulsion mechanisms play a role. This requires then a refined hydrodynamic modeling and more elaborate methods to determine the swimmer dynamics. These methods include multiparticle collision dynamics (MPCD) simulations of bacteria and sperm cells [109], bead-modeling of complex-shaped swimmers combined with Stokesian dynamics simulations [112], and numerical boundary integral equation methods invoking particle surface triangularization [89].

6.4 Swimming near a surface

For a dipolar swimmer above a planar wall or surface ($x-y$ plane at $z = 0$), the flow field is a superposition of its dipolar flow field $\mathbf{u}_{\rm D}$ and an image flow field, $\mathbf{u}_{\rm Im}$, generated by a system of singularities located below the surface. The image flow contribution is required to satisfy the surface BC (recall Sec.5). In Fig. 30, this situation is illustrated for the simplest case of a pusher swimming above a free surface. The only BC here is the fluid-impermeability of the surface which can be fulfilled by considering the swimmer in the half-space $z > 0$ to move along with its mirror image in the fluid extended to the lower half-space $z < 0$. This is akin to the symmetric side-by-side motion of two swimmers in bulk fluid discussed earlier in relation to Fig. 29.

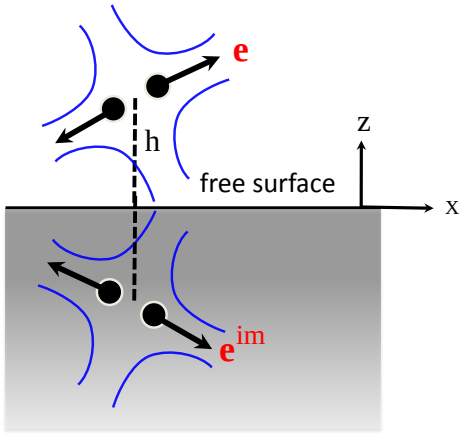

Fig. 30 Swimming with an image: A free surface attracts a puller and reorients its axis parallel to the surface ($\theta = 0$ with $\mathbf{e}\cdot\mathbf{e}_x = \cos\theta$). A puller on the other hand is reoriented perpendicular to the surface, swimming subsequently either away or head-on into the surface. This qualitative behaviour remains valid for a Navier partial-slip wall, a no-slip wall, and a liquid interface [26].

Using again the translational Faxén theorem for a point-like freely advected particle, the vertical velocity component induced on the swimmer at $\mathbf{R}_0 = (0,0,z_0)$ with $z_0 = h > 0$ is

$$V_z(\theta,h) = u_{\mathrm{D},z}(\mathbf{R}_0 - \mathbf{R}_0^*;\mathbf{e}^{im}) = -\frac{p}{32\pi\eta h^2}\left[1 - 3\sin^2\theta\right], \tag{125}$$

where θ is the tilt angle of the swimmer with respect to the surface, so that $\sin\theta = \mathbf{e}\cdot\mathbf{e}_z = -\mathbf{e}^{im}\cdot\mathbf{e}_z$. Here, $\mathbf{R}_0^*$ and $\mathbf{e}^{im}$ are the position and orientation vectors of the mirror dipole, respectively. Provided the tilt angle is not too large so that $\theta < \arcsin(1/\sqrt{3})$, the dipole is attracted by the surface. To reveal the influence of the free surface (i.e. of the image dipole flow part) on the swimmer's orientation, we employ the rotational Faxén law where the swimmer is described as an elongated spheroid. The result is [26]

$$\Omega_y(\theta,h) = \frac{3p\sin(2\theta)}{128\pi\eta h^3}\left[1 + \left(\frac{\Gamma^2-1}{\Gamma^2+1}\right)\sin^2(\theta)\right], \tag{126}$$

according to which for all values of θ, the pusher always aligns parallel to the free surface, with the induced velocity in this aligned configuration being equal to $V_z(0,h) = -p/(32\pi\eta h^2)$. Note that $\Gamma \gg 1$ for a typical bacterium such as *E. coli*, owing to its extended flagella bundle.

Using the respective image flows, the calculations outlined above for a free surface are rather straightforwardly extended to a clean liquid interface and a Navier partial-slip wall, respectively, with the no-slip wall included as a limiting case [26, 113]. For a clean liquid-liquid interface, e.g., the corresponding result is

$$\Omega_y(\theta,h) = \frac{3p\sin(2\theta)}{128\pi\eta_1 h^3}\left[1+\frac{1}{2}\left(\frac{\Gamma^2-1}{\Gamma^2+1}\right)\left(\frac{\lambda+(2+\lambda)\sin^2(\theta)}{1+\lambda}\right)\right] \quad (127)$$

$$V_z(0,h) = -\frac{p\,(2+3\lambda)}{32\pi\eta_1\,(1+\lambda)\,h^2}\,, \quad (128)$$

with the free and no-slip surface results recovered as the limiting cases for $\lambda = \eta_2/\eta_1 = 0$ and $\lambda \to \infty$, respectively. A pusher is always attracted by and aligned to a nearby liquid interface, for any value of the viscosity ratio. The pusher is likewise attracted and aligned parallel by a partial-slip wall, for any value of the Navier slip length [26].

The attraction by and the accumulation of biological microswimmers near surfaces is indeed observed in many biological experiments. According to the above analysis, pullers are oriented hydrodynamically in the direction perpendicular to the surface ($\theta = \pm\pi/2$), swimming either head-on away or right into the surface.

The simple modeling of pushers as linear force dipoles gives the prediction that they should move in straight trajectories along a surface, owing to the rotational symmetry of the aligned dipole with respect to the surface normal. However, it is known experimentally that bacteria such as *E. coli* do swim in clockwise (CW) traversed circles along a glass surface [114], as viewed from inside the fluid, whereas near a clean free surface the spherical trajectories are traversed counter-clockwise (CCW). The CW circular motion near the glass plate can be changed to a CCW motion if a sufficient amount of free polymers is added to the fluid. Likewise, the CW circular motion at a clean free surface can change to a CCW motion upon the addition of detergents accumulating at the surface. The circular motion of a bacterium is interrupted when a tumbling event occurs.

This surface-specificity of the trajectories can be attributed to the chiral bacterial propulsion mechanism not resolved in the simple force dipole model. It becomes essential when the swimmer gets close to a surface. To understand qualitatively the CCW circular motion of a pusher near a free surface, recall that this is equivalent to a pusher swimming in the flow field of its image. The image moves with the same speed as the actual pusher, but the helical flagellar bundle (cell body) of the image rotates opposite to that of the pusher. Recall that the bundle of a bacterium rotates counterclockwise if viewed from behind, and suppose that the bacterium is oriented momentarily along the y-axis. The counter-rotating flagellar helices (cell bodies) of the swimmer and its image create then a disturbance flow directed in the positive (negative) x-direction. Since the swimmer is freely advecting in this flow, it will perform a CCW circular motion [115]. Qualitative arguments similar to the present ones can be given to explain the CW circular motion of a bacterium at a no-slip surface where an advection flow oppositely directed to that near a free surface is created [108].

As Lopez and Lauga have recently shown [26], the surface-specific circular motion of a bacterium is quantitatively explainable on the singularity method level by adding a so-called rotlet dipole singularity solution, $\mathbf{u}_{\mathrm{RD}}(\mathbf{r}) \sim \mathscr{O}(r^{-3})$, to the linear force dipole solution of $\mathscr{O}(r^{-2})$. The rotlet dipole part accounts on the long-distance level for the counter-rotating flagellum and cell body parts of the torque-free pusher.

Using this flow singularity model in conjunction with surface-specific image systems, interesting quantitative predictions regarding critical parameter values for the CW to CCW motion transition for partial-slip walls and surfactant-covered interfaces have been made [26].

7 Concluding Remarks

The present notes give an introduction into the world of low-Reynolds-number flows and associated passive and active (i.e. self-propelling) microparticle motions, with the focus on surface and interfacial effects. As the topics treated in the notes should have amply illustrated, studying low-Reynolds-number phenomena is important, and often leads to surprising findings. Our aim has been to provide the reader with basic background knowledge which facilitates further reading of more advanced research texts on processes involving microparticles and animalcules suspended in viscous fluids. We have presented the governing equations of Stokes flows and their essential properties in a rather descriptive way, avoiding detailed calculations which can be found in more specialized textbooks and overview papers. While the material is presented in a rather systematic way, many important phenomena such as Marangoni surface flows [23], hydrodynamic screening near boundaries [116], wall-induced apparent like-charge attraction of colloidal macroions [117, 118], and hydrodynamically induced surface accumulation of microparticles [119, 55, 120] have been only shortly addressed, with an occasional reference to related literature, or even not mentioned at all. The present notes can serve as a good preparation for an improved understanding of research papers on these additional phenomena.

Acknowledgments: These notes include and complement material which was presented in August 2014 at the SOMATAI summer school in Berlin, and in March 2014 at the SOMATAI workshop in Jülich. It is our pleasure to thank the organizer of these events, Peter Lang, for having invited us to present a lecture on the colloidal hydrodynamics of microparticles and associated interfacial effects. We thank Maria Ekiel-Jeżewska (Polish Academy of Sciences, Warsaw) for having provided us with the streamlines figures of a point force near a planar interface, and Jonas Riest and Rafael Roa (ICS-3, FZ Jülich) and Roland Winkler (IAS-2, FZ Jülich) for helpful discussions. Moreover, we are grateful to Ulrike Nägele (FZ Jülich, ICS-3) for her help with travel and accommodation.

References

1. J. K. G. Dhont, *An Introduction to Dynamics of Colloids*, Elsevier, 1996.
2. P. Szymczak and M. Cieplak, J. Physics. Condens. Matter. **23**, 033102 (2011).
3. R. G. Larson and J. J. Magda, Macromolecules **22**, 3004 (1989).
4. H. Tanaka, J. Phys. Condens. Matter **13**, 4637 (2001).
5. P. Wojtaszczyk and J. B. Avalos, Phys. Rev. Lett. **80**, 754 (1998).

6. C. Korn and U. S. Schwarz, Phys. Rev. Lett. **97**, 138103 (2006).
7. O. B. Usta, J. E. Butler, and A. J. C. Ladd, Phys. Fluids **18**, 031703 (2006).
8. E. Guazzelli and J. F. Morris, *A Physical Introduction to Suspension Dynamics*, Cambridge Univ. Press, 2012.
9. G. Nägele, Colloidal Hydrodynamics, in *Physics of Complex Colloids*, edited by C. Bechinger, F. Sciortino, and P. Ziherl, volume 184, Proceedings of the International School of Physics "Enrico Fermi", page 451, IOS Press, Amsterdam; SIF, Bologna, 2012.
10. G. Nägele, Dynamics of Charged-Particles Dispersions, in *Proceedings of the 5th Warsaw School of Statistical Physics*, page 83, Warsaw Univ. Press, 2014.
11. E. J. Hinch, Hydrodynamics at Low Reynolds Numbers: A Brief and Elementary Introduction, in *Disorder and Mixing*, edited by E. Guyon, J.-P. Nadal, and Y. Pomeau, volume 2, pages 43–55, Springer Netherlands, 1988.
12. P. N. Pusey, Colloidal Suspensions, in *Liquids, Freezing and Glass Transition*, edited by J. P. Hansen, D. Levesque, and J. Zinn-Justin, page 763, Elsevier, Amsterdam, 1991.
13. R. B. Jones and P. N. Pusey, Annu. Rev. Phys. Chem. **42**, 137 (1991).
14. S. Kim and S. J. Karrila, *Microhydrodynamics: Principles and Selected Applications*, Butterworth- Heinemann, Boston, 1991.
15. J. Happel and H. Brenner, *Low Reynolds Numbers Hydrodynamics*, Kluwer, Dordrecht, 1991.
16. Z. Zapryanov and S. Tabakova, *Dynamics of Bubbles, Drops and Rigid Particles*, Fluid Mechanics and Its Applications, Springer Netherlands, 2011.
17. G. K. Batchelor, *An Introduction to Fluid Dynamics*, Cambridge Mathematical Library, Cambridge Univ. Press, 2000.
18. L. D. Landau and E. M. Lifshitz, *Fluid Mechanics*, Course of Theoretical Physics, Pergamon Press, 1987.
19. E. Guyon, J. P. Hulin, and L. Petit, *Physical Hydrodynamics*, Oxford Univ. Press, 2001.
20. G. I. Taylor, *Low Reynolds Number Flows*, National Committe For Fluid Mechanics Films, website: http://web.mit.edu/hml/ncfmf.html, 1966.
21. W. B. Russel, D. A. Saville, and W. R. Schowalter, *Colloidal Dispersions*, Cambridge Monographs on Mechanics, Cambridge University Press, 1989.
22. E. Lauga, M. P. Brenner, and H. A. Stone, The No-Slip Boundary Condition, in *Springer Handbook of Experimental Fluid Mechanics*, edited by C. Tropea, A. Yarin, and J. F. Foss, Springer, 2007.
23. L. G. Leal, *Laminar Flow and Convective Transport Processes*, Butterworth-Heinemann, 1992.
24. N. Lecoq, R. Anthore, B. Cichocki, P. Szymczak, and F. Feuillebois, J. Fluid Mech. **513**, 247 (2004).
25. R. Tuinier and T. Taniguchi, J. Phys. Condens. Matter **17**, L9 (2005).
26. D. Lopez and E. Lauga, Phys. Fluids **26**, 071902 (2014).
27. K. H. Lan, N. Ostrowsky, and D. Sornette, Phys. Rev. Lett. **57**, 17 (1986).
28. B. Cichocki, M. L. Ekiel-Jezewska, and E. Wajnryb, J. Chem. Phys. **136**, 071102 (2012).
29. J. F. Brady and G. Bossis, Annu. Rev. Fluid Mech. **20**, 111 (1988).
30. I. M. Jánosi, T. Tél, D. E. Wolf, and J. A. C. Gallas, Phys. Rev. E **56**, 2858 (1997).
31. M. L. Ekiel-Jeżewska and E. Wajnryb, Phys. Rev. E **83**, 067301 (2011).
32. D. L. Ermak and J. A. McCammon, J. Chem. Phys. **69**, 1352 (1978).
33. G. Nägele, Brownian Dynamics simulations, in *Computational Condensed Matter Physics*, volume 32, Forschungszentrum Jülich Publishing, 37th IFF Spring School edition, 2006.
34. A. T. Chwang and T. Wu, J. Fluid Mech. **67**, 787 (1975).
35. C. Pozrikidis, *Boundary Integral and Singularity Methods for Linearized Viscous Flow*, Cambridge Univ. Press, 1992.
36. J. D. Jackson, *Classical Electrodynamics*, John Wiley & Sons, 3rd edition, 1998.
37. B. Cichocki, B. U. Felderhof, and K. Hinsen, J. Chem. Phys. **100**, 3780 (1994).
38. M. L. Ekiel-Jeżewska and E. Wajnryb, Precise Multipole Method for Calculating Hydrodynamic Interactions Between Spherical Particles in the Stokes Flow, in *Theoretical Methods for Micro Scale Viscous Flows*, edited by F. Feuillebois and A. Sellier, pages 127–172, 2009.

39. M. Lisicki, arXiv:1312.6231 [physics.flu-dyn] (2013).
40. L. G. Leal, Annu. Rev. Fluid Mech. **12**, 435 (1980).
41. S. E. Spagnolie and E. Lauga, J. Fluid Mech. **700**, 105 (2012).
42. H. Luo and C. Pozrikidis, J. Eng. Math. **62**, 1 (2007).
43. G. K. Batchelor, Journal of Fluid Mechanics **44**, 419 (1970).
44. M. M. Tirado, C. L. Martinez, and J. G. de la Torre, J. Chem. Phys. **81**, 2047 (1984).
45. R. G. Cox, J. Fluid Mech. **44**, 791 (1970).
46. J. B. Keller and S. I. Rubinow, J. Fluid Mech. **75**, 705 (1976).
47. G. G. Stokes, Trans. Cambridge Philos. Soc. **9**, 8 (1851).
48. J. L. Anderson, Annu. Rev. Fluid Mech. **21**, 61 (1989).
49. J. H. Masliyah and S. Bhattacharjee, *Electrokinetic and Colloid Transport Phenomena*, John Wiley & Sons, 2006.
50. H. J. Keh and J. L. Anderson, J. Fluid Mech. **153**, 417 (1985).
51. A. S. Khair and T. M. Squires, Phys. Fluids **21**, 042001 (2009).
52. R. Golestanian, T. B. Liverpool, and A. Ajdari, New J. Phys. **9**, 126 (2007).
53. H. A. Stone and A. D. Samuel, Phys. Rev. Lett. **77**, 4102 (1996).
54. C. Contreras-Aburto and G. Nägele, J. Chem. Phys. **139**, 134110 (2013).
55. F. Weinert and D. Braun, Phys. Rev. Lett. **101**, 168301 (2008).
56. J. Rotne and S. Prager, J. Chem. Phys. **50**, 4831 (1969).
57. H. Yamakawa, J. Chem. Phys. **53**, 436 (1970).
58. E. Wajnryb, K. A. Mizerski, P. J. Zuk, and P. Szymczak, J. Fluid Mech. **731**, R3 (2013).
59. R. Courant and D. Hilbert, *Methods of Mathematical Physics II*, Interscience, New York, 1962.
60. F. M. Weinert and D. Braun, Phys. Rev. Lett. **101**, 168301 (2008).
61. P. J. Zuk, E. Wajnryb, K. A. Mizerski, and P. Szymczak, J. Fluid Mech. **741**, R5 (2014).
62. B. Carrasco and J. Garcia de la Torre, Biophys J. **76**, 3044 (1999).
63. B. Cichocki, R. B. Jones, R. Kutteh, and E. Wajnryb, J. Chem. Phys. **112**, 2548 (2000).
64. S. Bhattacharya, J. Bawzdziewicz, and E. Wajnryb, Physica A **356**, 294 (2005).
65. M. Kedzierski and E. Wajnryb, J. Chem. Phys. **133**, 154105 (2010).
66. D. J. Acheson, *Elementary Fluid Dynamics*, Oxford Univ. Press, 1990.
67. D. J. Jeffrey and Y. Onishi, J. Fluid Mech. **139**, 261 (1984).
68. R. Tadmor, J. Phys. Condens. Matter **13**, L195 (2001).
69. M. L. Ekiel-Jeżewska and R. Boniecki, Stokes Flow Generated by a Point Force in Various Geometries II. Velocity Field, Technical report, IFTR, Polish Acad. Sci., 2010.
70. B. Cichocki, M. L. Ekiel-Jeżewska, G. Nägele, and E. Wajnryb, J. Chem. Phys. **121**, 2305 (2004).
71. J. Blake, Proc. Camb. Phil. Soc. **70**, 303 (1971).
72. K. Aderogba and J. R. Blake, Bull. Aust. Math. Soc. **18**, 345 (1978).
73. J. Blake and A. Chwang, J. Eng. Math. **8**, 23 (1974).
74. E. Lauga and T. M. Squires, Phys. Fluids **17**, 103102 (2005).
75. M. Lisicki, B. Cichocki, S. A. Rogers, J. K. G. Dhont, and P. R. Lang, Soft Matter **10**, 4312 (2014).
76. B. Cichocki and R. B. Jones, Physica A **258**, 273 (1998).
77. H. A. Lorentz, *Abhandlung über Theoretische Physik*, B. G. Teubner, Leipzig und Berlin, 1907.
78. H. Faxén, Ark. Mat. Astron. Fys. **17**, 1 (1923).
79. H. Brenner, Chem. Eng. Sci. **16**, 242 (1961).
80. A. J. Goldman, R. G. Cox, and H. Brenner, Chem. Eng. Sci. **22**, 637 (1967).
81. A. J. Goldman, R. G. Cox, and H. Brenner, Chem. Eng. Sci. **22**, 653 (1967).
82. W. Dean and M. O'Neill, Mathematika **10**, 13 (1963).
83. W. Dean and M. O'Neill, Mathematika **11**, 67 (1964).
84. R. B. Jones, J. Chem. Phys. **123**, 164705 (2005).
85. B. Lin, J. Yu, and S. Rice, Phys. Rev. E **62**, 3909 (2000).
86. R. Sadr, C. Hohenegger, H. Li, P. J. Mucha, and M. Yoda, J. Fluid Mech. **577**, 443 (2007).
87. P. Huang and K. Breuer, Phys. Rev. E **76**, 046307 (2007).

88. L. Lobry and N. Ostrowsky, Phys. Rev. B **53**, 12050 (1996).
89. K. Ishii, T. Iwai, and H. Xia, Opt. Express **18**, 7390 (2010).
90. M. A. Plum, W. Steffen, G. Fytas, W. Knoll, and B. Menges, Opt. Express **17**, 10364 (2009).
91. M. A. Plum, J. Rička, H.-J. Butt, and W. Steffen, New J. Phys. **12**, 103022 (2010).
92. P. Holmqvist, J. K. G. Dhont, and P. R. Lang, Phys. Rev. E **74**, 021402 (2006).
93. P. Holmqvist, J. K. G. Dhont, and P. R. Lang, J. Chem. Phys. **126**, 044707 (2007).
94. M. Hosoda, K. Sakai, and K. Takagi, Phys. Rev. E **58**, 6275 (1998).
95. M. Lisicki, B. Cichocki, J. K. G. Dhont, and P. R. Lang, J. Chem. Phys. **136**, 204704 (2012).
96. S. A. Rogers, M. Lisicki, B. Cichocki, J. K. G. Dhont, and P. R. Lang, Phys. Rev. Lett. **109**, 098305 (2012).
97. B. J. Berne and R. Pecora, *Dynamic Light Scattering: With Applications to Chemistry, Biology, and Physics*, Dover Books on Physics Series, Dover Publications, 2000.
98. R. Sigel, Curr. Opin. Colloid Interface Sci. **14**, 426 (2009).
99. G. Nägele, Phys. Rep. **272**, 215 (1996).
100. B. Cichocki, M. L. Ekiel-Jeżewska, and E. Wajnryb, J. Chem. Phys. **140**, 164902 (2014).
101. W. B. Russel, E. J. Hinch, L. G. Leal, and G. Tieffenbruck, J. Fluid Mech **83**, 273 (1977).
102. S.-M. Yang and L. G. Leal, J. Fluid Mech. **136**, 393 (1983).
103. E. P. Ascoli, D. S. Dandy, and L. G. Leal, J. Fluid Mech. **213**, 287 (1990).
104. I. Cantat and C. Misbah, Phys. Rev. Lett. **83**, 880 (1999).
105. U. S. Agarwal, A. Dutta, and R. A. Mashelkar, Chem. Eng. Sci. **49**, 1693 (1994).
106. C. Berdan and L. G. Leal, J. Colloid Interface Sci. **87**, 62 (1982).
107. R. Trouilloud, T. Yu, A. Hosoi, and E. Lauga, Phys. Rev. Lett. **101**, 048102 (2008).
108. E. Lauga and T. R. Powers, Rep. Prog. Phys. **72**, 096601 (2009).
109. J. Elgeti, R. G. Winkler, and G. Gompper, Rep. Prog. Phys. , accepted (2014).
110. J. Lighthill, *Mathematical Biofluiddynamics*, SIAM, Philadelphia, 1975.
111. E. M. Purcell, Am. J. Phys. **45**, 3 (1977).
112. J. W. Swan, J. F. Brady, and R. S. Moore, Phys. Fluids **23**, 071901 (2011).
113. A. P. Berke, L. Turner, H. C. Berg, and E. Lauga, Phys. Rev. Lett. **101**, 038102 (2008).
114. E. Lauga, W. R. DiLuzio, G. M. Whitesides, and H. A. Stone, Biophys. J. **90**, 400 (2006).
115. R. Di Leonardo, D. Dell'Arciprete, L. Angelani, and V. Iebba, Phys. Rev. Lett. , 038101 (2011).
116. P. P. Lele, J. W. Swan, J. F. Brady, N. J. Wagner, and E. M. Furst, Soft Matter **7**, 6844 (2011).
117. T. Squires and M. Brenner, Phys. Rev. Lett. **85**, 4976 (2000).
118. T. M. Squires, J. Fluid Mech. **443**, 403 (2001).
119. R. Di Leonardo, F. Ianni, and G. Ruocco, Langmuir **25**, 4247 (2009).
120. J. Morthomas and A. Würger, Phys. Rev. E **81**, 051405 (2010).